Estimating cloud liquid water content from radar reflectivity for stratocumulus clouds during the Cloud Lidar and Radar Experiment

J.J.M. de Wit
November 1999

Thesis report, IRCTR-S-005-00

International Research Centre on Telecommunications-transmission and Radar
Department of Information Technology and systems
Delft University of Technology

Summary

Clouds have a significant influence upon the earth-atmosphere radiation budget. In order to quantify their role, parameterisation of cloud properties is required. Therefore a good understanding of cloud macro- and micro-physical properties is needed. Cloud characteristics are described in terms of, among others, ice/liquid water content, reflectivity and particle size spectra.

An extensive study of clouds was made during the Cloud Lidar and Radar Experiment (Clare). This campaign took place between October 5th and October 23rd 1998 near Chilbolton in the United Kingdom. During Clare simultaneous in-situ and co-located ground based measurements were performed. Among the airborne equipment were a Johnson-Williams liquid water content meter, particle size measuring probes and the 94 GHz 'Kestrel' radar. The ground based equipment consisted among others of the 94 GHz 'Miracle' radar and several lidars and radiometers.

Throughout Clare the cloud liquid water content (LWC) was measured by the Johnson-Williams sensor mounted on an aircraft. The sample volume of this sensor is however very small. Thus to measure the LWC profile throughout a whole cloud a lot of aircraft runs at different heights have to be made. During the time needed to cover the whole cloud the properties will alter.
It would be less time consuming if the LWC could be obtained using radar measurements. The sample volume of ordinary radars is about 10^5 times as large as the sample volume of the Johnson-Williams. In order to obtain the LWC with radar observations a relationship between the radar reflectivity (z) and the LWC must exist. Throughout the years several empirical Z-LWC have been proposed. However these relationships ignore drizzle sized droplets. Since the clouds were drizzling during Clare these relationships will not be valid for the Clare data set.

In this report Z-LWC relations valid for the Clare campaign are computed using the in-situ data. The particle size spectra are measured by the Forward Scattering Spectrometer probe (FSSP) and the Two-dimensional Cloud probe (2DC). The FSSP measures particles up to 22.75 μm radius and the 2DC measures particles up to 400 μm radius. The raw FSSP data are corrected so that the LWC from the particle size spectra matches the LWC measured by the Johnson-Williams liquid water content sensor. Two different correction schemes are used; a constant correction and a particle size dependent correction. Then the FSSP and the 2DC spectra are merged to obtain full size spectra. If the full size spectra are known the LWC and the radar reflectivity can be computed. Due to the r^6 dependency the reflectivity is dominated by the 2DC sized droplets, the LWC on the other hand is dominated by the FSSP sized particles.

Using the LWC and the reflectivity calculated from the spectra a Z-LWC relationship can be computed. If only the FSSP sized particles are taken into account, a well-defined Z-LWC relationship exists. If the 2DC sized particles are considered also, the Z-LWC scatter plot shows a lot of scatter and the least-squares fit is very bad.
In order to use the Z-LWC relationship found considering only FSSP data, the reflectivity due to FSSP sized droplets and the reflectivity due to 2DC sized droplets must be separated. Doppler information maybe used to discriminate Z_{FSSP} and Z_{2DC}.

Generally the Doppler spectra show a small peak in the FSSP range. At the transition between the FSSP and the 2DC range there is a minimum in the reflectivity. Then Z_{FSSP} can be found by integrating the Doppler spectrum up to this minimum. Since

the peak is very small it is doubtful if this peak will show up in actually measured Doppler spectra. Turbulence and wind shear broaden the Doppler spectrum especially for smaller drop sizes.

Since the Doppler spectrum cannot be used to discriminate Z_{FSSP} and Z_{2DC}, the 2DC sized droplets have to be taken into account also. Then the scatter in the Z-LWC plot must be limited. The deviating data points in the scatter plot are mostly data with high reflectivities and modest LWC. Thus the corresponding spectra are heavily weighted towards large droplets. These spectra can be recognised using the effective radius.

If spectra are filtered out using the effective radius the fit is improved. However the least-squares fit is still not good enough. Therefore a maximum-likelihood fit is implemented. Using this maximum-likelihood fit and the effective radius as extra parameter the results obtained are rather good. The root-mean-square residue is only 0.25 g/m^3 using either correction scheme.

The relationships are validated using an independent data set. These data are measured in stratocumulus 350 km off the Namibian coast on October 3rd 1995. The Namibian data clearly show a two sloped behaviour. The slope depends on the number of 2DC sized droplets present. The Clare data also exhibit this two sloped behaviour, although it is not as clear. This may lead to the conclusion that several cases have to be taken into account determining which Z-LWC relationship is valid:

- There are few 2DC sized droplets present, thus the reflectivity is dominated by the FSSP sized particles. The reflectivity from the cloud is generally below –20 dBZ. In this case the relationship found considering only FSSP data is valid
- The reflectivity is dominated by 2DC sized droplets. The average reflectivity from the cloud is above –20 dBZ. In this case the exponent *b* in the Z-LWC relationship is constant for different stratocumulus, while the multiplicative factor *a* depends on the average reflectivity of the cloud.
- There are many large (ice) particles present; the effective radii from the spectra are very large. In this case there is no relation between the reflectivity and the LWC.

Further research is needed to validate this theory and to find ways to discriminate the different cases.

The Z-LWC relations found in this report are not easily verified. The Kestrel radar and the Johnson-Williams were mounted on different aircraft. These aircraft have different speeds, so they were not at the same place simultaneously.
Generally the LWC from the Johnson-Williams does not match the LWC calculated from the Kestrel measurements. The differences are probably caused by the fact that the Kestrel and Johnson-Williams observations are not from the same spot.
If the reflectivity computed from the spectra and the reflectivity measured by the Kestrel are comparable, the estimated and the measured LWC match very well also. There is only a slight difference using either correction method. Since the 2DC sized droplets dominate the reflectivity, the total reflectivity from the spectra will barely increase if the size dependent correction is used.

Furthermore the LWP is computed from the ground based Miracle radar data using the Z-LWC relationships. This LWP is validated using the LWP calculated from the 93 GHz radiometer data. Only for low values of the LWP there is a difference of about 60 g/m^2. At this point cannot be said if this difference is due to the retrieval method.

Table of Contents

1. Introduction

Clouds play an important role in climate modelling; they have a significant influence on the earth-atmosphere radiation budget. Parameterisation of clouds and cloud related processes is required to quantify the effect of clouds on climate. Therefore a good understanding of cloud macro- and micro-physical properties is needed. The microstructure of clouds is described in terms of, among others, ice/liquid water content, reflectivity and particle size spectra. Remote sensing techniques to measure these cloud properties are available. However in-situ measurements are still needed to validate the remote sensing techniques.

A comprehensive study of clouds was made during the Cloud Lidar and Radar Experiment (Clare). This campaign took place between October 5th and October 23rd 1998 near Chilbolton in the United Kingdom. During Clare simultaneous in-situ measurements and co-located ground based observations were performed.

The airborne measurements were performed by three aircraft; the C-130 'Hercules', the Fokker 27 'Arat' and the 'Falcon' 20-E jet aircraft. The Hercules carried, among others, particle size probes and a Johnson-Williams liquid water content sensor. The Arat carried the 94 GHz 'Kestrel' radar and the 'Leandre' lidar. And finally the Falcon carried, among others, the 'Alex' lidar. The ground based equipment included the 3 GHz scanning radar 'CAMRa', the 94 GHz radar 'Miracle' and several radiometers.

The aircraft flew runs to the west of Chilbolton to and from the radar site. The Hercules and the Arat have comparable airspeeds of roughly 100 ms $^{-1}$. Being a jet the Falcon has a much higher airspeed. Although their speeds are different the aircraft arrived overhead Chilbolton simultaneously. Each run is about ten minutes long; that is $\pm$60 km. The Hercules flew around 2 km through the clouds to obtain in-situ micro-physical measurements, the Arat flew above the clouds between 3 and 5 km to monitor the cloud top and the Falcon flew between 6 and 12 km to be able to observe cirrus clouds also.

A more detailed description of the Clare campaign can be found in [Baedi, De Wit and Baptista, 1999] and [De Wit and Baedi, 1999].

During Clare the cloud liquid water content (LWC) was measured in-situ with a Johnson-Williams sensor mounted on the Hercules aircraft. The sample volume of this sensor is however very small; in the order of $1.4 \cdot 10^{-3}$ m^3/s if the aircraft is flying at 100 m/s [Ouldbridge ,1982]. Hence to measure the LWC profile throughout a whole cloud a lot of runs at different heights have to be made. During the time needed to cover the cloud the cloud properties will alter.

It would be less time consuming if the LWC could be obtained with radar measurements. The sample volume of ordinary radars is about 10^5 times as large as the sample volume of the Johnson-Williams sensor. In order to obtain the LWC with radar measurements some relationship between the radar reflectivity (z) and the LWC must exist. Several empirical Z-LWC relationships have been proposed. For stratocumulus [Sauvageot and Omar, 1987] found a relationship of the form:

$$z = a \cdot LWC^{b} = 0.03 \cdot LWC^{1.31} \qquad 1.1$$

where z is the radar reflectivity in [mm^6/m^3] and LWC is the liquid water content in [g/m^3]. In [Fox and Illingworth, 1997] a similar relation is proposed for stratocumulus:

$$z = 0.031 \cdot LWC^{1.56} \qquad 1.2$$

However these relationships ignore drizzle sized droplets. They will therefore not be valid for the Clare data since during Clare the clouds were drizzling.

In the frame of this work stratocumulus clouds containing only liquid particles are studied. This restricts the data set to runs 32, 51, 52, 61, 62, 71 and 72 flown on October 7th, run 52 flown on October 13th and run 11 flown on October 22nd. Radar images of these runs are included in appendix E. In these images the track of the Hercules aircraft is also shown. A detailed description of the runs studied in this report can be found in [Baedi, De Wit and Baptista, 1999] and [De Wit and Baedi, 1999].

In this report Z-LWC relationships valid for the Clare data set are computed using the in-situ particle size data. In order to be valid for the Clare data the relations have to take drizzle sized droplets into account. In chapter 2 the theory is outlined and it is explained how the Z-LWC relations are computed from the size spectra. The relations found for the different runs are presented. In the next chapter it is attempted to obtain the reflectivity due to small droplets only, using the Doppler spectrum. In chapter 4 efforts are made to limit the scatter due to the drizzle sized droplets and a maximum-likelihood fit is introduced. Then in chapter 5 data from an independent data set are investigated to see if the Z-LWC relations found are also valid for other types of stratocumulus clouds. The final results obtained with the Z-LWC relations are presented in chapter 6. And finally in chapter 7 the conclusions are summarised.

The work described in this report is performed in the frame of the graduation work at the International Research Centre on Telecommunications-transmission and Radar, Delft University of Technology.

The particle size probes and the Johnson-Williams liquid water sensor were operated by the UK Meteorological Office-Meteorological Research Flight. I especially wish to thank Peter Francis from UKMO-MRF for providing the in-situ data and for answering lots of questions. The 94 GHz Kestrel radar is property of the University of Winconsin, but during Clare it was operated by the Institute Pierre Simon Laplace-CETP from France. The 94 GHz Miracle radar was operated by the GKSS-Institut für Atmosphärenphysik from Germany. The 93 GHz radiometer was operated by the Rutherford Appleton Laboratory. Finally I would like to thank Charles Wrench from RAL for providing the 93 GHz radiometer data.

2. Z-LWC Relationships

The particle size spectra are measured by the Forward Scattering Spectrometer Probe (FSSP) and the Two-dimensional Cloud probe (2DC). The FSSP measures particles in the size range of 1.75 μm to 22.75 μm. The particles are sized in 15 radius bins of 1.5 μm each. The 2DC measures larger particles in the range of 12.5 μm to 400 μm. The 2DC sizes the particles in 32 radius bins of 12.5 μm each. The probes both produce a spectrum every 5 seconds. The particle probes are well described in [Moss et al., 1993].

The raw FSSP data are corrected so that the LWC from the particle spectra matches the LWC measured by the Johnson-Williams (JW). This correction is performed because the FSSP is known to under-estimate in cases where the size spectrum is heavily weighted towards small droplets [P.N. Francis, personal communication]. During Clare the FSSP measurements were multiplied by a constant factor *CF*:

$$CF = \frac{LWC_{JW} - LWC_{2DC}}{LWC_{FSSP}} \qquad 2.1$$

Figure 2.1a visualises the operation of the constant correction.
However in [De Wit and Baedi, 1999; chapter 3] a size dependent correction algorithm is proposed. Using this size dependent algorithm the larger particles are corrected more than the small particles, as is shown in figure 2.1b. In this report the results obtained for both corrections are presented.

In order to get a complete particle size spectrum the spectra from the FSSP and the 2DC are merged. The merged spectrum consists of bin 2 to 12 of the FSSP and bin 2 to 32 of the 2DC. The first bins of both probes are not used because they produce unreliable data. In the interval where the probes overlap the measurements of the 2DC are used because they are statically more reliable. The merging technique is described in detail in [Baedi, De Wit and Baptista, 1999]. Figure 2.2 shows a typical example of a merged spectrum.

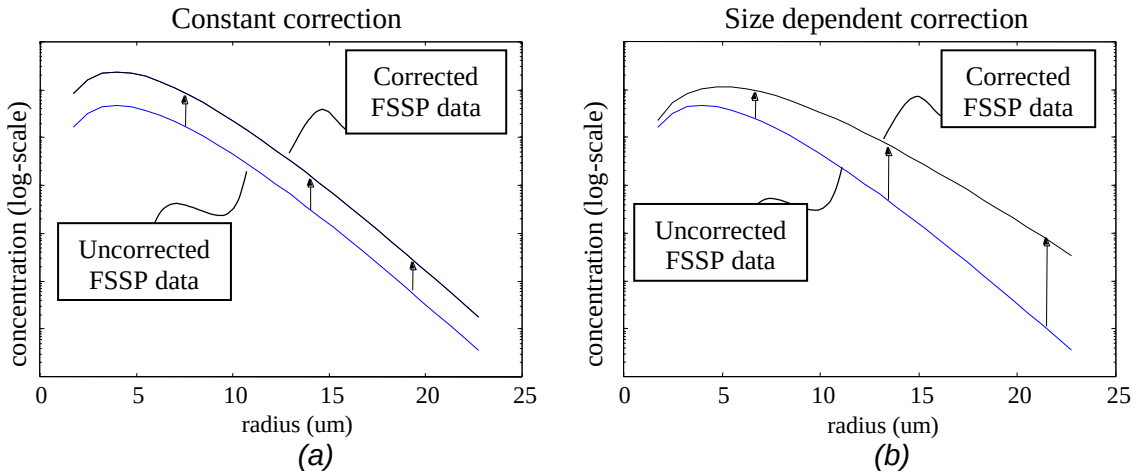

Figure 2.1: Visualisation of the different correction schemes. Panel a shows the constant correction; the data are multiplied with a constant factor (corresponding to a shift in log-scale). Panel b shows the size dependent correction; the larger the particles, the larger the correction factor.

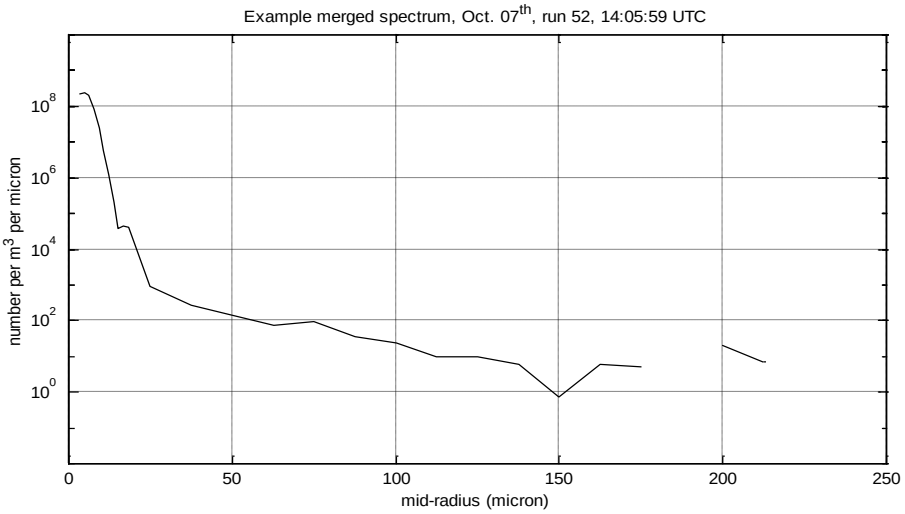

Figure 2.2: A typical example of a merged spectrum measured during Clare, Run 52, Oct. 7th.

If the cloud particle size spectra are known the radar reflectivity *z* can be computed using the Rayleigh approximation. This approximation is valid if the particles are small compared to the wavelength. At radar wavelengths the Rayleigh approximation is accurate for liquid cloud particles. In that case the reflectivity can be calculated using:

$$z = 64 \int_0^\infty N(r)\, r^6\, dr \qquad [\mathrm{mm^6/m^3}] \qquad 2.2$$

where *r* is the particle radius in [mm] and *N(r)dr* is the number of particles per m^3 in the range (*r*, *r+dr*). However the particle probes count droplets in a finite number of bins, formula (2.2) then reduces to a summation over the bins of the probes:

$$z = 64 \sum_i N_i\, r_i^6 \qquad [\mathrm{mm^6/m^3}] \qquad 2.3$$

where *i* is the bin number, N_i is the concentration of particles in bin *i* in [m^{-3}] and r_i is the mid-radius of bin *i* in [mm].

The cloud liquid water content can also be computed from the size spectra. Assuming that the cloud only contains water and that the droplets are spherical, the LWC can be computed using:

$$LWC = \tfrac{4}{3}\pi \cdot \rho_w \cdot 10^{-6} \int_0^\infty N(r)\, r^3\, dr \qquad [\mathrm{g/m^3}] \qquad 2.4$$

where ρ_w is the density of water in [kg/m^3] and *r* is the droplet radius in [mm]. Using the data from the probes formula (2.4) also reduces to a summation:

$$LWC = \tfrac{4}{3}\pi \cdot \rho_w \cdot 10^{-6} \cdot \sum_i N_i\, r_i^3 \qquad [\mathrm{g/m^3}] \qquad 2.5$$

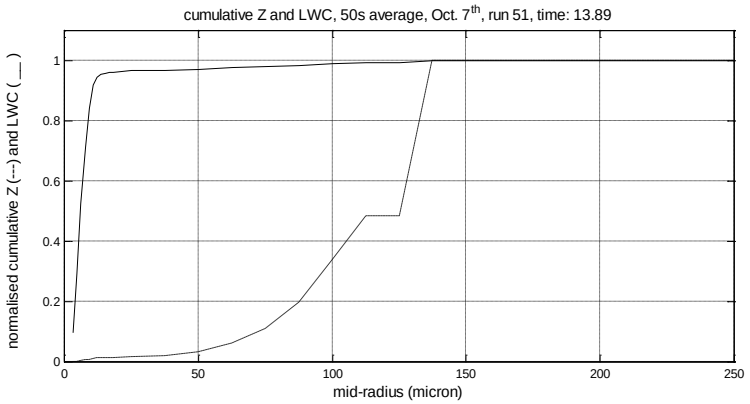

Figure 2.3: Typical examples of cumulative diagrams of the reflectivity (solid line) and the LWC (dashed line) versus particle radius. Ten size spectra are averaged. Run 51, Oct. 7th.

Ice particles are not spherical and their density is particle size dependent [Illingworth et al., 1997]. Therefore it is more cumbersome to compute the ice/liquid water content and the reflectivity for clouds containing ice particles. Therefore only liquid water clouds are considered in this study.

Due to the r^6 dependency the reflectivity is dominated by large droplets; that is droplets in the 2DC range (r > 20 μm). The LWC on the other hand is dominated by the particles in the FSSP range; generally the 2DC sized particles contribute 5% or less to the LWC. Figure 2.3 shows the cumulative diagrams of the reflectivity and the LWC versus particle size.

The number of larger particles is relatively small; they seem to just pop up once in a while according to the 2DC measurements. This causes the reflectivity to be uncorrelated from spectrum to spectrum. Figure 2.4a shows the autocorrelation of the reflectivity. From this figure it is seen that the autocorrelation drops below 1/e within 10 seconds. Note that the probes produce a spectrum every 5 seconds. The LWC on the other hand is not uncorrelated from spectrum to spectrum. Figure 2.4b shows that the autocorrelation of the LWC drops below 1/e after about 30 seconds.

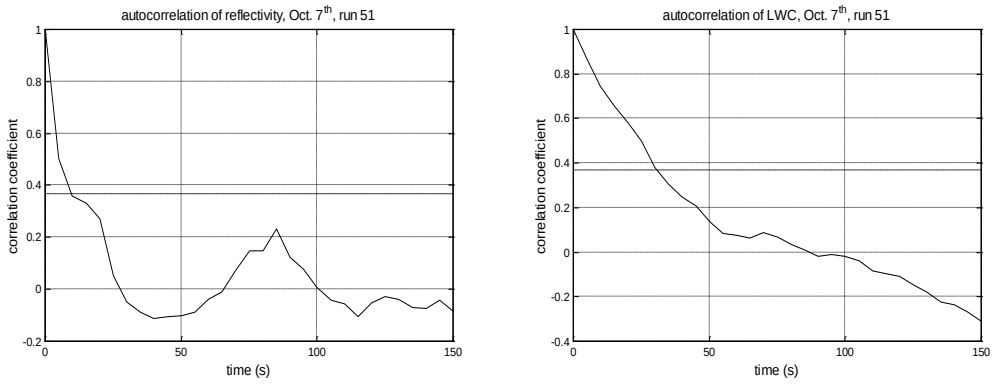

(a) *(b)*

Figure 2.4: Plots of the autocorrelation coefficient of the reflectivity (a) and the LWC (b). The dashed line shows the 1/e level. Run 51, Oct. 7th.

The fact that the reflectivity decorrelates so quickly will lead to a lot of scatter in a Z versus LWC plot. The Z-LWC scatter plots for the runs analysed in this report are presented in appendix A. These plots show indeed a lot of scatter if the 2DC data are taken into account. Note that the fit on the data from run 62 of October 7th is even decreasing.
Figure 2.5a shows the least-squares fits in a single plot. It is seen that these fits are very different from run to run.
In appendix B the Z-LWC scatter plots using the size dependent correction algorithm are shown. From figure 2.5b can be seen that these fits also deviate a lot from run to run if 2DC data are taken into account.
However the differences between the fits using both correction algorithms are small. Using the root-mean-square (rms) error as a measure for the quality of the fits, it cannot be said that one of the correction schemes leads to a better fit.

The rms-error is defined as:

$$rms-error = \sqrt{\frac{\sum_{1}^{n}\left(LWC_{spectrum} - LWC_{fit}\right)^2}{n}} \qquad [g/m^3] \qquad 2.6$$

where $LWC_{spectrum}$ is the LWC actually contained in the size spectrum, LWC_{fit} is the LWC estimated from the reflectivity using the least-squares fit and n is the number of spectra.
Note that the data are fitted twice. After the first fit, data deviating more than three standard deviations (3σ) from the fit are discarded. Afterwards the data are fitted again and the rms-error is computed. For run 61 and 62 of October 7th this 3σ limit is not used, since these data do not exhibit a linear fit at all.
The overall accuracy of the Johnson-Williams is 10% [Illingworth and Hignett, 1998] and the average value of the LWC for maritime stratocumulus is about 0.3 g/m^3 [Cavazzini et al., 1997]. Nevertheless a value of 0.20 g/m^3 for the rms-error is considered reasonable.

The scatter plots using only FSSP data are also shown in appendix A. These plots show that if only FSSP data are taken into account there is considerably less scatter. From figure 2.6a it is seen that in this case the fits are more consistent.
The Z_{FSSP}–LWC_{FSSP} scatter plots using the size dependent correction are shown in Appendix B. These fits are also more consistent from run to run. Again the differences between the fits using the different correction schemes are small.
Using the size dependent correction the reflectivity from the spectra increases, since the large particles are corrected more than the small particles. This increase in reflectivity leads to a shift in the scatter plots. Comparing appendices A and B it is indeed seen that the fits are shifted towards higher reflectivities if the size dependent correction is used. The exponent b does not change very much using either the constant or size dependent correction.
If the 2DC data are taken into account this shift is not seen in the scatter plots, since in that case the FSSP sized particles contribute 5% or less to the total reflectivity from the spectra (figure 2.3).

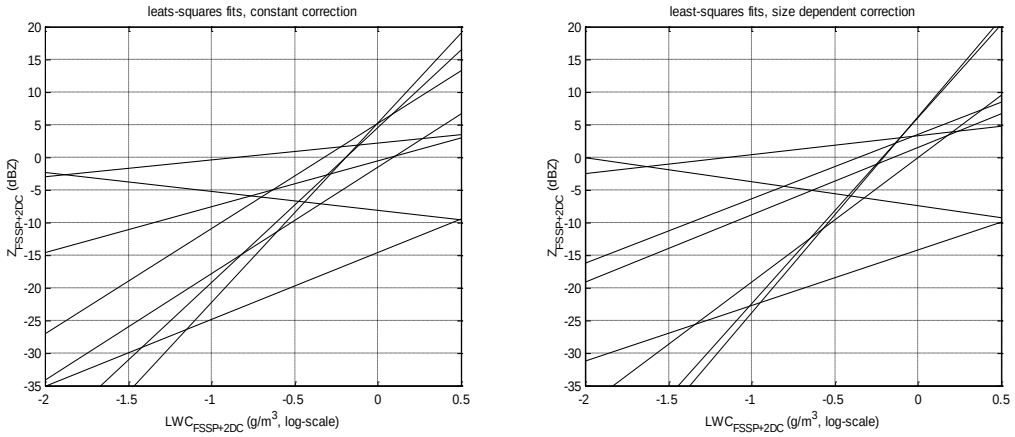

(a) *(b)*

Figure 2.5: The least-squares fits of the different runs in a single plot taking both the FSSP data and the 2DC data into account. Panel a shows the fits using the constant correction and panel b shows the fits using the size dependent correction.

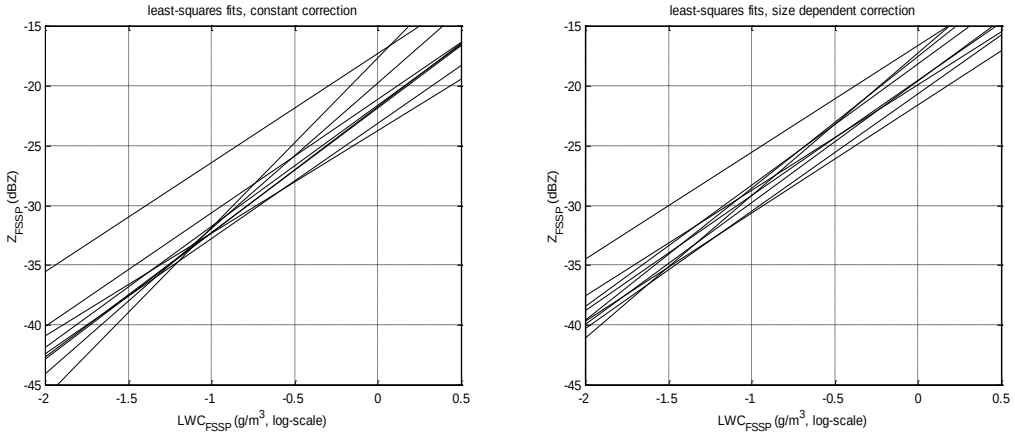

(a) *(b)*

Figure 2.6: The least-squares fits of the different runs in a single plot taking only the FSSP data into account. Panel a shows the fits using the constant correction and panel b shows the fits using the size dependent correction.

The least-squares fit on all the runs is shown in figure 2.7a. The fit found in this case is very bad; the rms-error is 75 g/m^3. If the size dependent correction is used the fit is even worse, see figure 2.7b. Thus these least-squares fits cannot be used to estimate the LWC from the radar reflectivity. Figure 2.7 shows however that the data are roughly around a line, see the hand-made fit in figure 4.1.

The fit on all runs taking only the FSSP data into account is shown in figure 2.8a. In this case there is less scatter present. The rms-error is only 0.38 g/m^3. Using the size dependent correction the fit is even a little better; the rms-error is 0.27 g/m^3.
Using these fits the LWC can be estimated reasonably well. However radars do not discriminate between reflectivity due to FSSP sized droplets and reflectivity due to 2DC sized droplets.

To be able to use the fits on the FSSP data the reflectivity measured by the radar must be separated in Z_{FSSP} and Z_{2DC}. This separation may be possible using different frequencies or using Doppler information.
Signals at high frequencies are more sensitive to small particles. If multiple signals with different frequencies are combined Z_{FSSP} and Z_{2DC} may be separated. Some work, using dual wavelength radar measurements has already been done [Hogan et al., 1999].
The terminal fall speed of cloud particles is size dependent. So maybe the Doppler spectrum can be used to discriminate reflectivity due to small droplets and reflectivity due to large droplets. If this is really the case is explored in chapter 3.
Polarisation information cannot be used in this context, since the flattening of cloud particles is significant only for particles with $r > 500$ μm [Pruppacher and Klett, 1997]. Furthermore the radar has to view the particles sideways.

Finally some notes on the least-squares fits presented in this report. Data points with LWC < 0.01 g/m^3 are not taken into account in the fits since 0.01 g/m^3 is about the noise level of the Johnson-Williams [P.N. Francis, personal communication]. Data points with Z < -35 dBZ are also not taken into account because that is around the sensitivity threshold of ordinary radars. For the fits using only FSSP data the threshold for the reflectivity is set at –45 dBZ.

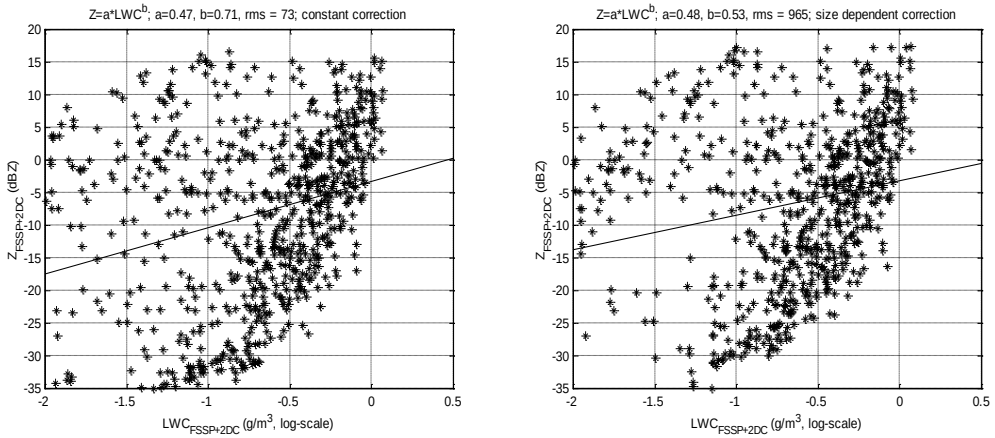

Figure: 2.7: The least-squares fit on all the data analysed in this report. If the constant correction is used (a) the rms-error is 73 g/m^3. Using the size dependent correction (b) the rms-error is 965 g/m^3.

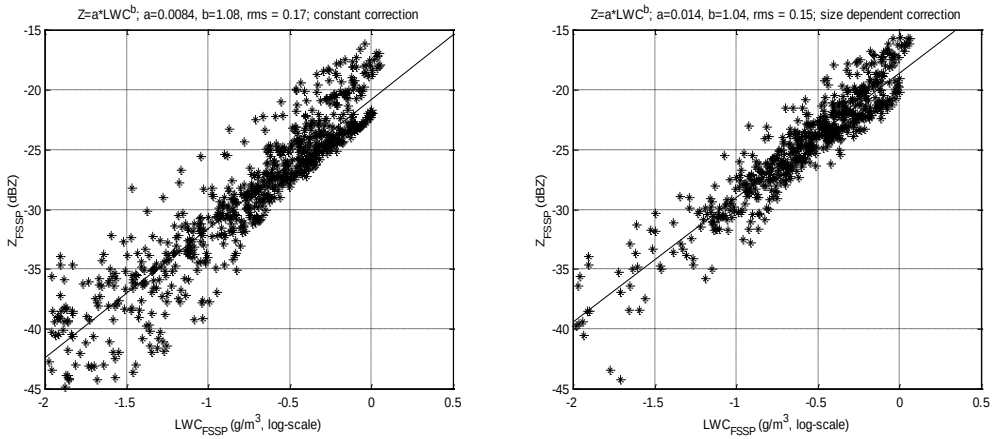

(a) *(b)*

Figure 2.8: The least-squares fit on all the data analysed in this report considering only the FSSP data. Using the constant correction (a) the rms-error is 0.17 g/m^3. The rms-error is only 0.15 g/m^3 if the size dependent correction is used (b).

3. Doppler spectrum

As explained in the last chapter Doppler information may be used to discriminate reflectivity due to small droplets and reflectivity due to large droplets. Since the terminal velocity of cloud droplets is particle size dependent. In [Rogers, 1976] the following relationships between the velocity and the particle size are presented:

$$v = 1.19 \cdot 10^{6}\, r^{2} \qquad [\mathrm{cms}^{-1}] \qquad 0 \le r \le 67\ \mu\mathrm{m} \qquad 3.1$$

and:

$$v = 8 \cdot 10^{3}\, r \qquad [\mathrm{cms}^{-1}] \qquad 67 \le r \le 600\ \mu\mathrm{m} \qquad 3.2$$

where v is the terminal velocity and r is the particle radius in [cm]. The terminal speed of the largest particle measured by the FSSP (r = 19 μm) is only 4.29 cms^{-1}.

The reflectivity can now be written as a function of velocity:

$$z(v) = z(r) \cdot \left| \frac{dr}{dv} \right| \qquad 3.3$$

Substituting relationship (3.1) and (3.2) results in:

$$z(v) = 64 \cdot N(r) \cdot r^{6} \cdot \left| \frac{1}{2 \cdot 1.19 \cdot 10^{6}} \cdot \sqrt{\frac{1.19 \cdot 10^{6}}{v}} \right| \qquad 0 \le v \le 53\ \mathrm{cms}^{-1} \qquad 3.4$$

and:

$$z(v) = 64 \cdot N(r) \cdot r^{6} \cdot \left| \frac{1}{8 \cdot 10^{3}} \right| \qquad 53 \le v \le 480\ \mathrm{cms}^{-1} \qquad 3.5$$

Figure 3.1 shows some examples of calculated Doppler spectra for different runs. Generally the Doppler spectra show a small peak in the FSSP interval. At the transition between the FSSP data and the 2DC data there is a minimum in the reflectivity. Thus Z_{FSSP} can be found by integrating the Doppler spectrum up to this minimum.
However it is very doubtful if this peak will show up in actually measured Doppler spectra. Turbulence and shear broaden the spectrum [Doviak and Zrnic., 1984], especially for smaller droplets. Furthermore not all calculated spectra show this peak as is seen from figure 3.1c.

In [Babb et al., 1999a] a technique to eliminate the influence of turbulence is presented. The broadening of the Doppler spectrum by turbulence is modelled. Using this model the particle size spectrum can be retrieved from the Doppler spectrum, assuming a gamma distribution.
This method is however not very reliable if the particle size spectra consist of the sum of two gamma distributions, as is the case with the Clare data. If ice particles are present the accuracy of this method is further deteriorated.
A similar technique is described in [Babb et al., 1999b]. This method does not make assumptions about the shape of the particle size spectrum or the phase of the particles. After elimination of the broadening due to turbulence, the Doppler spectrum

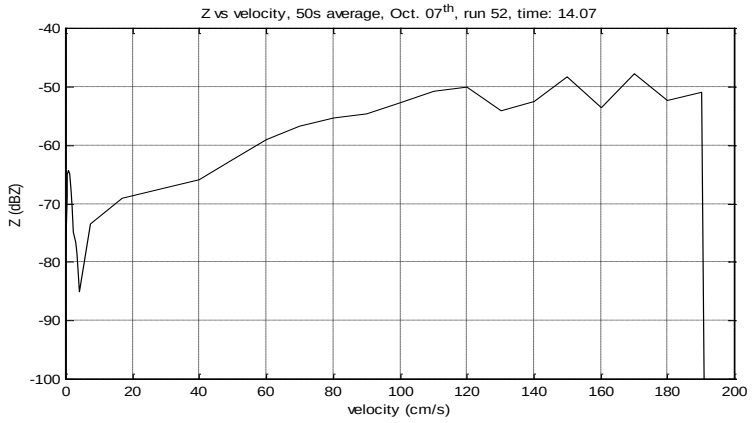

(a)

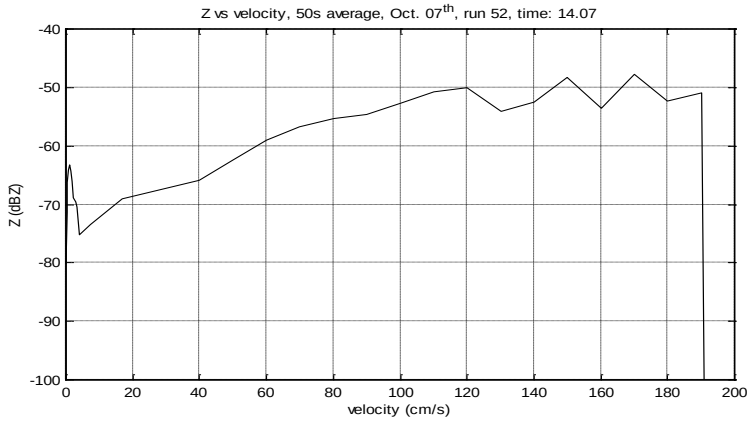

(b)

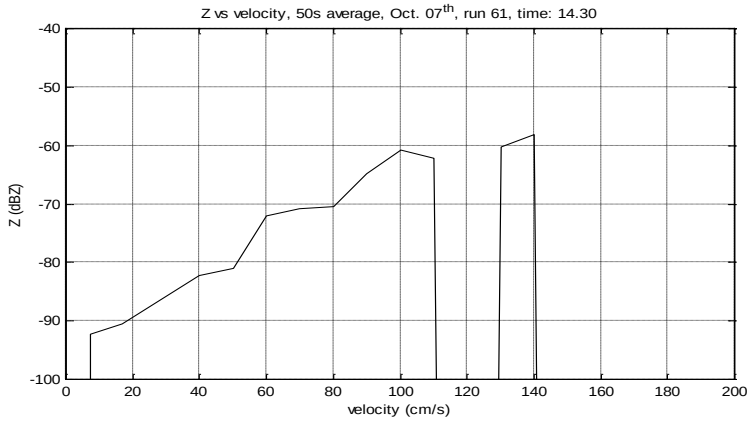

(c)

Figure 3.1: Several examples of Doppler spectra. Panel a shows an example from run 52, Oct 7th, using the constant correction and panel b shows the same spectrum if the size dependent correction is applied. In the first case the minimum at the transition of the FSSP and the 2DC data is lower. Finally panel c shows an example of run 61, Oct. 7th, using the constant correction. In this case there is no difference between both correction schemes since the FSSP did not measure anything.

is used to identify the different types of hydrometeors. However this technique is still in development.

Some examples of normalised cumulative diagrams of the reflectivity and the LWC versus velocity are included in figure 3.2. The cumulative diagram of the LWC can be used to determine the velocity at which 95% of the LWC is reached. The reflectivity reached at that velocity should more or less represent the reflectivity due to FSSP sized droplets.
From A.3 can be seen that run 52 of October 7th is a 'well behaved' run; the plot shows very little scatter. In this case 95% of the LWC is always reached around 1.19 cms^{-1} (bin 5-6). The percentage of the reflectivity reached at that velocity however varies from 0.06% to 89%. So there is no constant percentage of the reflectivity that corresponds to the LWC.

Figure A.5 shows that run 62 of October 7th is less well behaved; this plot exhibits a lot of scatter. In this case the results are even worse. Sometimes 95% of the LWC is only reached at 290 cms^{-1} (bin 39). During this run the percentage of the reflectivity reached at the velocity at which 95% of the LWC is reached, varies between 0.3% and 97%.
The cumulative reflectivity is normalised to the total reflectivity. As seen in chapter 2 the total reflectivity is uncorrelated from spectrum to spectrum. So it was to be expected that there is not a constant percentage of the total reflectivity from the spectrum corresponding to Z_{FSSP}. Thus Z_{FSSP} and Z_{2DC} cannot be separated using the Doppler spectrum.

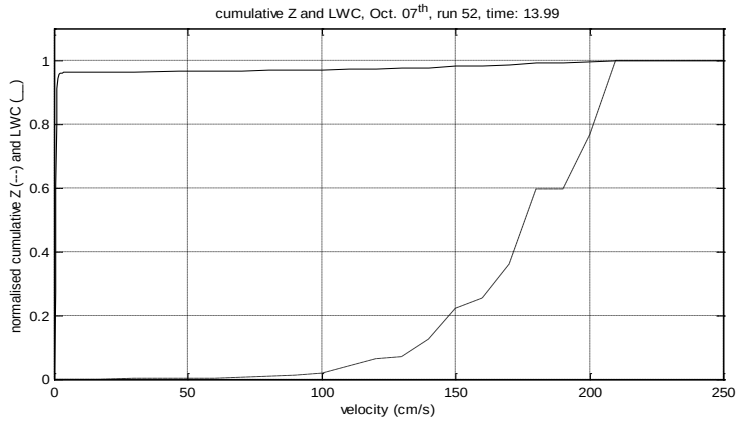

(a)

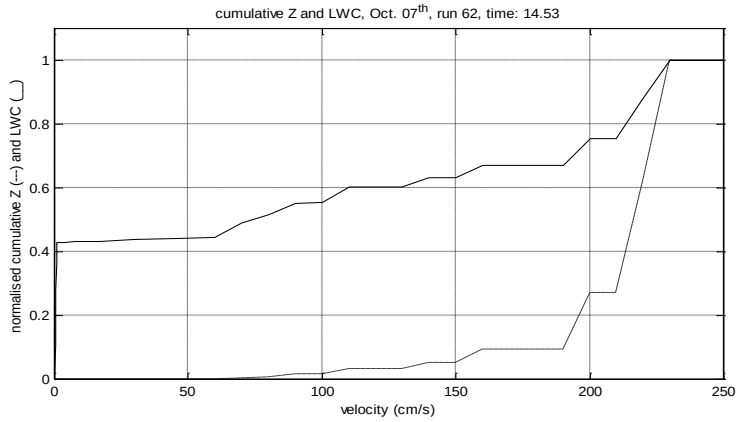

(b)

Figure 3.2: Some examples of cumulative diagrams of the reflectivity and the LWC versus velocity. The dashed lines represent the cumulative reflectivity normalised to the total reflectivity from the spectrum. The dashed lines show the cumulative LWC normalised to the total LWC contained in the spectrum. Panel a shows an example from run 52, Oct. 7th. This example is 'well behaved' most of the LWC (95%) is contained in the FSSP data while the reflectivity is determined by the 2DC data. Panel b is an example from run 62, Oct 7th. In this case only 50% of the LWC is contained in the FSSP data.

4. The effective radius as extra parameter

In the last chapter it is concluded that the Doppler spectrum cannot be used to discriminate Z_{FSSP} and Z_{2DC}. Thus in order to estimate the LWC from the radar reflectivity the 2DC data have to be taken into account also. Then the scatter present in the Z-LWC scatter plots, figure 2.6a and 2.6b, has to be limited.
Although figure 2.7 shows a lot of scatter, most data are roughly around a line, see figure 4.1. The deviating data are mostly above that line; that is they combine a high reflectivity with a rather modest LWC. Thus these spectra are weighted towards large droplets.
Spectra weighted towards larger droplets can be recognised using the effective radius. The effective radius is a parameter that shows how many large, 2DC sized droplets are present relative to the small, FSSP sized droplets. Spectra that are weighted towards larger droplets have large effective radii. The effective radius is defined as:

$$r_e = \frac{< r^3 >}{< r^2 >} = \frac{\sum_i N_i \, r_i^3}{\sum_i N_i \, r_i^2} \qquad [\mu m] \qquad 4.1$$

where r_i is the mid-radius of bin *i* in [μm].
However the goal of this work was to find a way to determine the LWC without in-situ data. Fortunately in [Baedi, 1999] it is stated that the effective radius can be obtained using radar and lidar measurements. In this report a relationship between the radar-lidar ratio z/α and the effective radius is found. Using this method the effective radius can be obtained with an accuracy of about 1 μm. However since the lidar signal attenuates very quickly in the cloud, this method is only applicable in the edges of the cloud.

In appendix C and D plots of the effective radius are presented. From these plots it is seen that the effective radius is generally below 10 μm. Furthermore it is confirmed that the effective radius becomes large if the reflectivity is high and the liquid water content is small.
In appendix E images from the 94 GHz Kestrel radar are included. These images are compared with the plots of the effective radius to determine the cloud conditions in which the effective radius becomes very large. However some precaution has to be taken comparing the plots.
The Kestrel was mounted on the Arat and the particle probes on the Hercules aircraft. These aircraft have slightly different velocities. Hence they were not at the same longitude simultaneously. They did however arrive at Chilbolton (-1.44° longitude) at the same time.
Unfortunately the Arat aircraft was not operational on October 22nd. Thus there are no data from the Kestrel available for run 11. Although the Arat was operational on October 7th, there is also no Kestrel image for run 32.

In the cloud the effective radius is generally between 5 and 10 μm (constant correction). See for example run 52, October 7th (figure C.2c).
During run 51 of October 7th the effective radius becomes very large in thinner parts of the cloud. The peak in the effective radius around –2.2° longitude is due to a measurement issue. At that point the Hercules is flying just below the cloud where the particle concentrations are very low. The 2DC however acquires its data in blocks and partially filled data blocks cannot be processed. Usually this is not a problem, but if the droplet concentration is very low it will take a long time to fill a data block. If this is the case the 2DC data are interpolated onto the 5 second grid assuming that the

2DC spectra are identical during the interpolation period [P.N. Francis, personal communication]. From figure D.2a it is seen that the 2DC data are indeed interpolated. Around –2.2° longitude the reflectivity exhibits a flat horizontal line. The second peak in the effective radius is also due to the Hercules flying just outside the cloud.
During run 61 and 62 of October 7th the Hercules flew near the bottom of the cloud at 1.9 km. Throughout these runs the effective radius becomes very large if the reflectivity is also large, that is 10 dBZ or higher. Most probably the Hercules flew through some light drizzle, so a lot of 2DC sized droplets were measured. Furthermore [Francis, 1999] reported that there was a significant amount of columnar ice crystals present between -1.95° longitude and Chilbolton. Since these crystals cannot be considered spherical formula (2.3) and (2.5) are not valid.
There were also columnar ice crystals present during run 71 and 72 of October 7th, between –1.8° longitude and Chilbolton [Francis, 1999]. Again the effective radius becomes very large in the parts of the cloud where ice crystals were present.

4.1 Using the effective radius to filter the data

Figure 4.2 verifies that the data deviating from the fit shown in figure 4.1, have large effective radii; typically larger than 10 μm. Using the effective radius these data can be filtered out to enhance the least-squares fit.
The rms-error is minimised if data with effective radii larger than 9 μm are filtered out. In that case the error is 1.50 g/m^3, see figure 4.3. Other limits for the effective radius lead to larger errors, although the difference is very small. If 8 μm is taken as limit the error is 1.59 g/m^3 and if 11 μm is taken as limit the error is 2.17 g/m^3. According to figure 2.6, the rms-error is 75 g/m^3 without filtering.

Thus far the data using the constant correction are presented. Applying the size dependent correction the effective radius will increase since the correction factor is larger for large droplets. Plots of the effective radius using the size dependent correction are included in appendix D. These plots show that the effective radius increases about 1 μm.
Using the size dependent correction a filter limit of 10 μm should be applied. The rms-error is smaller if 8 μm or 9 μm is used, but many data are rejected then. Additionally the increase in the rms-error shows a minimum if 10 μm is taken as filter limit. The error is 1.20 g/m^3 if data with effective radii larger than 10 μm are discarded. Referring to figure 2.6 the error is 761 g/m^3 without filtering.

Note that varying the filter limit 1 μm does not affect the rms-error too much. If the constant correction is used the difference is only 0.2 g/m^3 and with the size dependent correction the difference is about 0.4 g/m^3. Thus the method in [Baedi, 1999] to obtain the effective radius with radar and lidar measurements is accurate enough.

One should notice that filtering on the effective radius is not the same as clipping the tail of the size spectrum. If the effective radius is too large the whole spectrum is discarded.

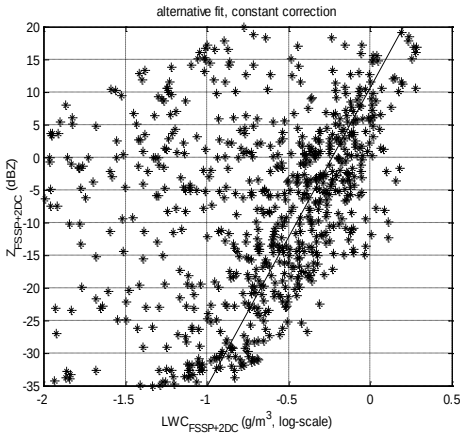

Figure 4.1: Desired fit, made by hand.

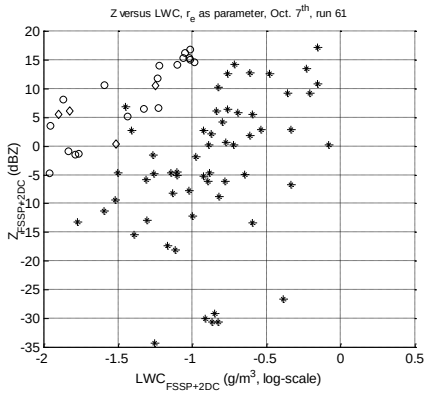

(a)

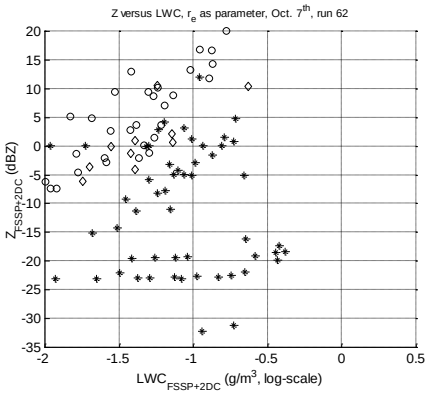

(b)

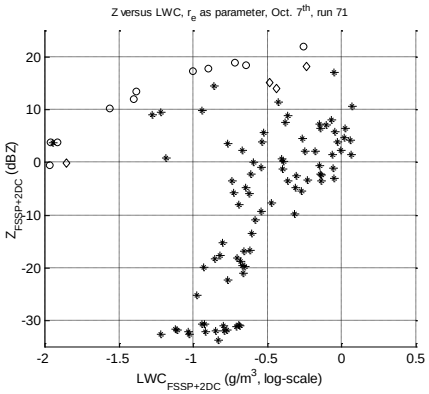

(c)

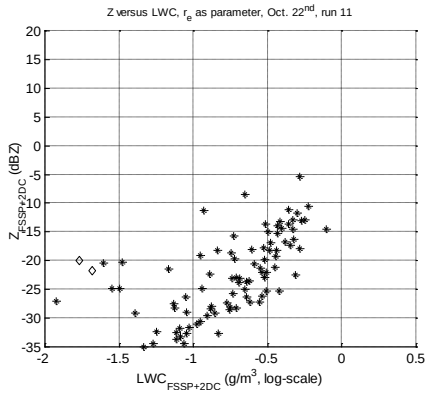

(d)

Figure 4.2: Scatter plots showing the effective radius. Panel a, b and c show run 61, 62 and 71 of Oct. 7th respectively. Panel d shows run 11 of Oct. 22nd. The symbols represent different effective radii; ✱: $r_e \leq 10$ μm, ♢: $r_e \leq 15$ μm and ○: $r_e > 15$ μm. The constant correction is used.

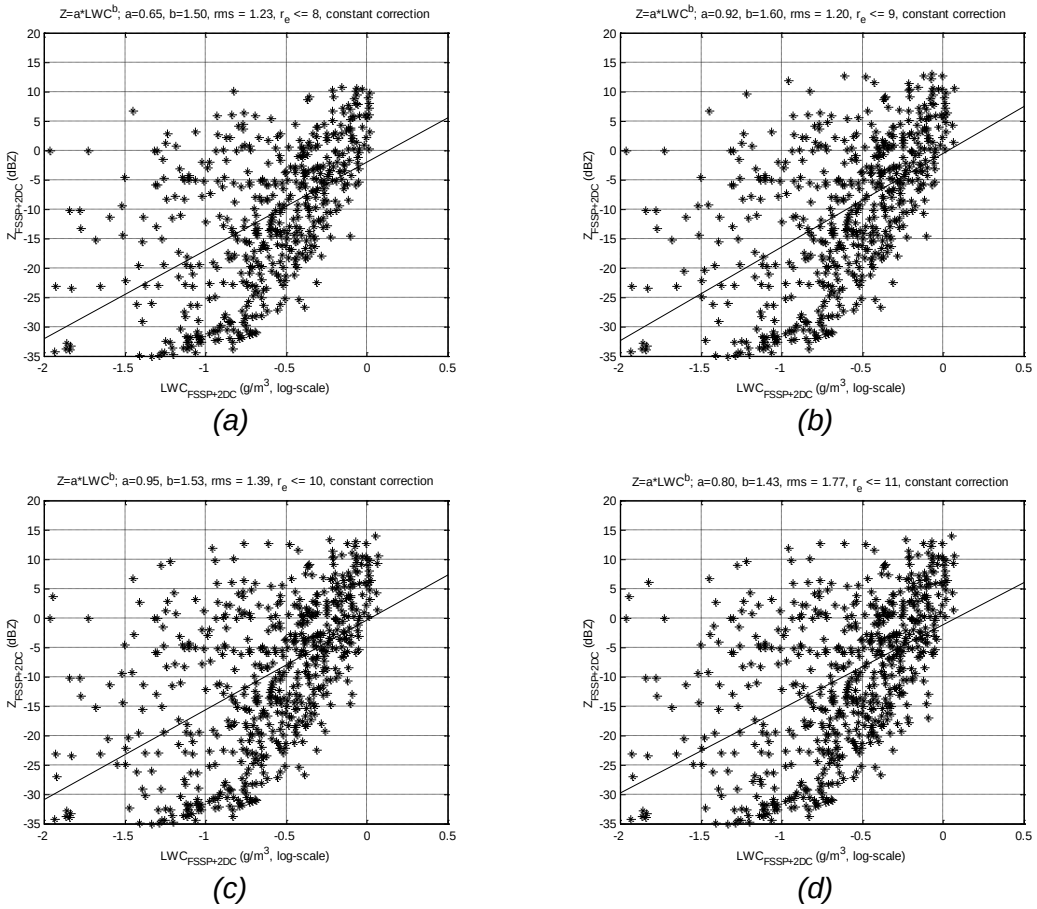

Figure 4.3: The least-squares fit if the effective radius is used to filter out deviating data. Panel a shows the fit if data with $r_e > 8$ μm are filtered out. In this case the error is 1.23 g/m^3. If data with $r_e > 9$ μm are rejected (panel b), the error is 1.20 g/m^3. The error is 1.39 g/m^3 if data with $r_e > 10$ μm are filtered out (panel c). And finally panel d shows the fit if data with $r_e > 11$ μm are discarded, then the error is 1.77 g/m^3. The constant correction is used.

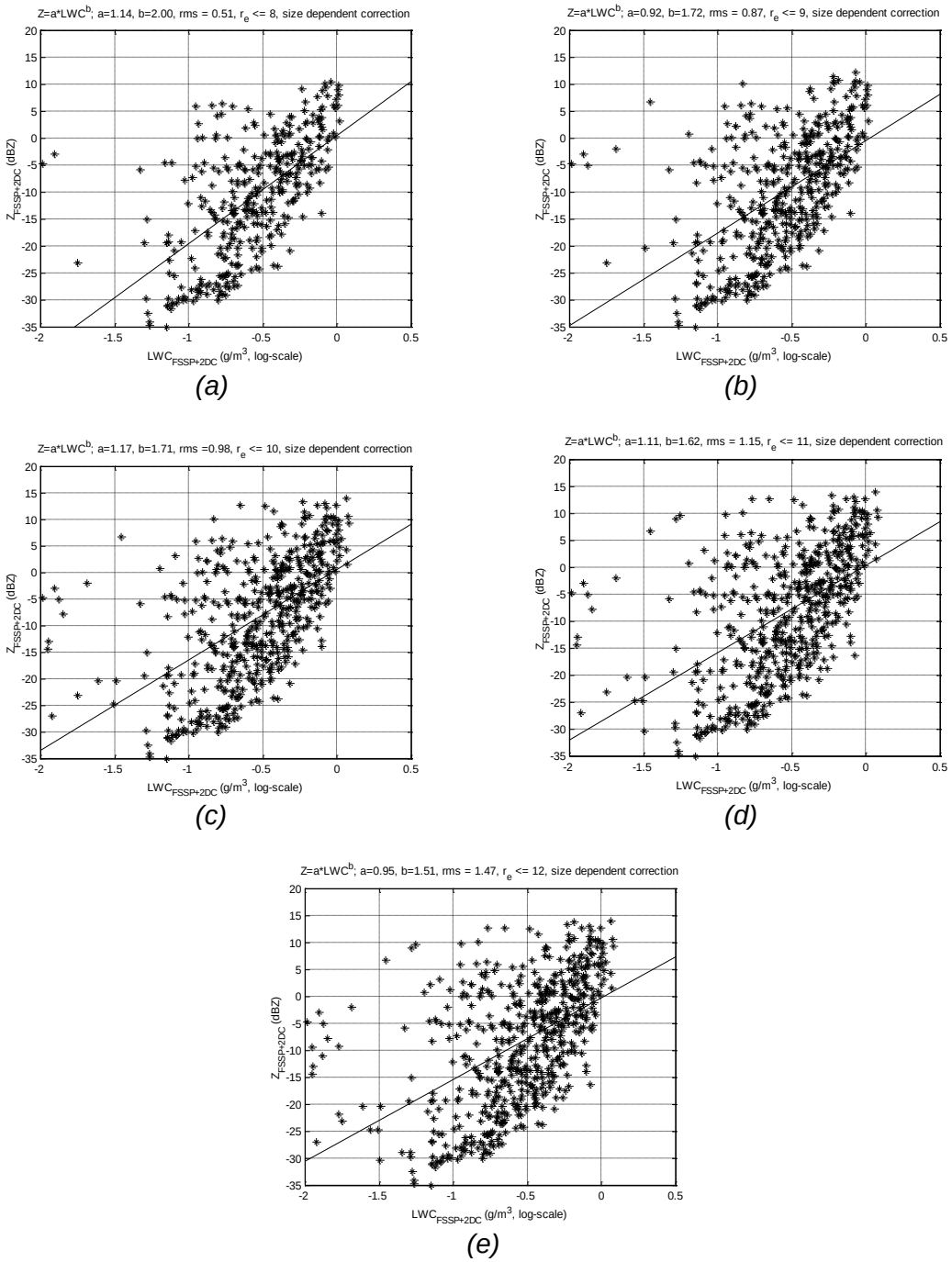

Figure 4.4: The least-squares fit if a filter on the effective radius applied to reject deviating data. Panel a shows the fit if data with $r_e > 8$ μm are discarded, then the error is 0.51 g/m^3. If data with $r_e > 9$ μm are filtered out (panel b), the error is 0.87 g/m^3. The error is 0.98 g/m^3 if data with $r_e > 10$ μm are filtered out (panel c). Rejecting data with $r_e > 11$ μm leads to an error of 1.15 g/m^3 (panel d). And finally panel e shows the fit if data with $r_e > 12$ μm are filtered out, then the error is 1.47 g/m^3. The size dependent correction is used.

4.2 Maximum-likelihood fit

After filtering or normalising the fit is still far from the 'desired' fit shown in figure 4.1. So maybe another type of fitting should be applied to enhance the results. In this paragraph a maximum-likelihood fit is presented.
First the data are divided in reflectivity-intervals of 5 dBZ and LWC-intervals of 0.1 g/m^3. The dashed lines in figure 4.5 represent these intervals. Then the algorithm searches the square containing most data points for each reflectivity-interval. In figure 4.5 these squares are marked with a large point. If two or more intervals contain the same number of data, the number of points in the neighbours is determining. Finally the Z-LWC relationship is found performing a least-squares fit on the marked squares.

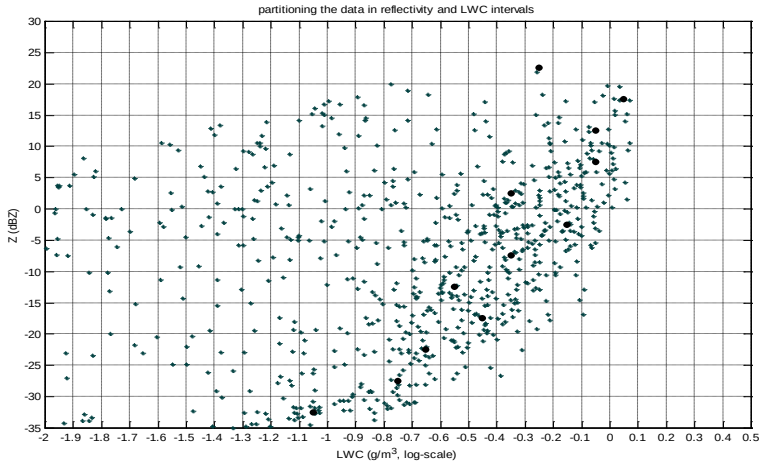

Figure 4.5: The operation of the maximum-likelihood fitter. For each reflectivity-interval the square containing most data is searched. These squares are marked with a large point. Finally the Z-LWC relationship is found applying a least-squares fit on the data in the marked squares.

The maximum-likelihood fits are shown in figure 4.6. The rms-errors are computed neglecting data that are more than three standard deviations off the fit. For both the constant correction and the size dependent correction the error is only 0.3 g/m^3.
If data with large effective radii are also neglected, the results are even a little better (figure 4.7). In this case the error is about 0.25 g/m^3 for both correction schemes. This error is considered acceptable. Thus the final relationships between the reflectivity and the LWC are:

$$z = 28.26 \cdot LWC^{4.88} \qquad 4.2$$

for the constant correction, and:

$$z = 14.82 \cdot LWC^{4.57} \qquad 4.3$$

if the size dependent correction is applied. Solving relation (4.2) and (4.3) for the LWC results in:

$$LWC = 0.503 \cdot z^{0.205} \qquad 4.4$$

if the constant correction is used, and:

$$LWC = 0.554 \cdot z^{0.219} \qquad 4.5$$

for the size dependent correction. The variance of the estimated LWC can then be written as a function of the variance of the measured reflectivity:

$$\mathrm{var}(LWC) = \left(\frac{\partial LWC(z)}{\partial z} \right)^2 \cdot \mathrm{var}(z) \qquad 4.6$$

Substituting equation (4.4) and (4.5) in (4.6) results in:

$$\mathrm{var}(LWC) = \left\{ 0.011 \cdot z^{-1.59} \right\} \cdot \mathrm{var}(z) \qquad 4.7$$

for the constant correction, and:

$$\mathrm{var}(LWC) = \left\{ 0.015 \cdot z^{-1.56} \right\} \cdot \mathrm{var}(z) \qquad 4.8$$

for the size dependent correction.

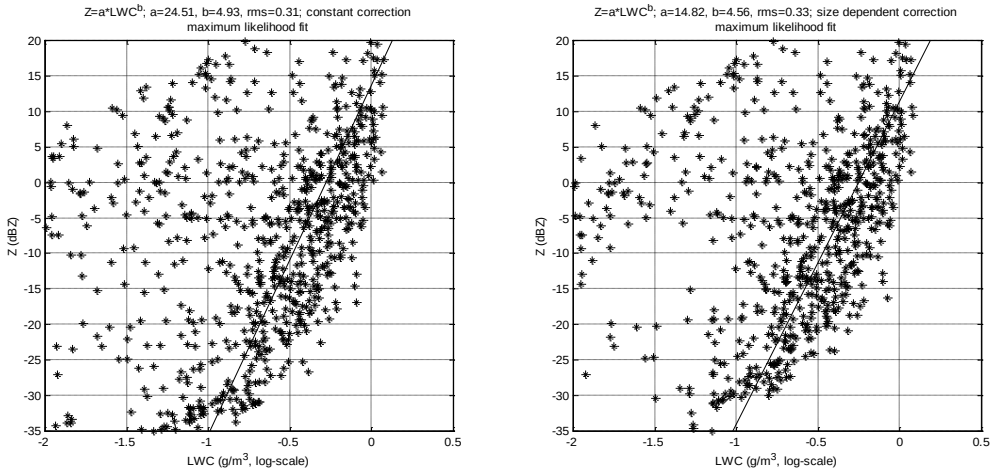

(a) *(b)*

Figure 4.6: The maximum likelihood fit on all data. Using the constant correction the rms-error is 0.31 g/m^3 (panel a). If the size dependent correction is applied the error is about the same: 0.33 g/m^3 (panel b).

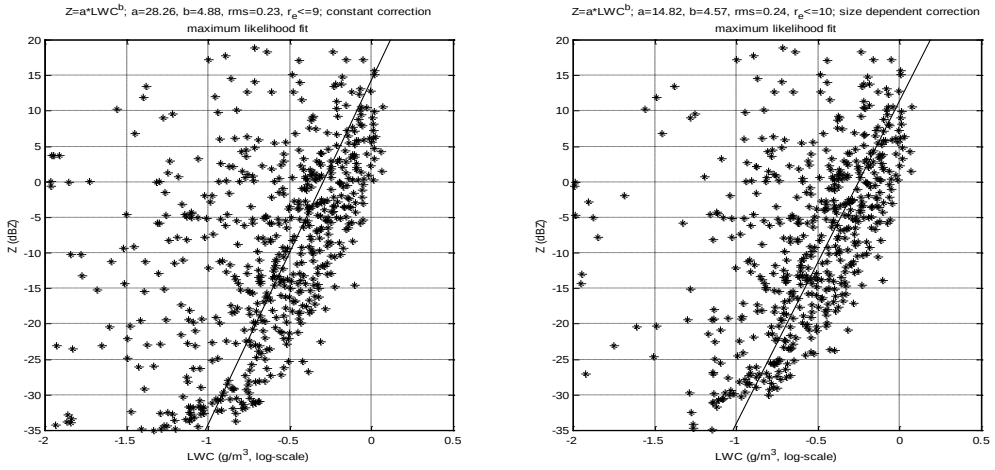

(a) *(b)*

Figure 4.7: The maximum likelihood fit if deviating data are filtered out using the effective radius. Using the constant correction, data with r_e > 9 μm are filtered out. In that case the rms-error is 0.23 g/m^3 (panel a). Data with r_e > 10 μm are discarded if the size dependent correction is used. Then the error is 0.24 g/m^3 (panel b).

5. Another campaign; in-situ data

In order to see if the fits are generally valid, data from an independent data set have been investigated. These data are measured in stratocumulus 350 km off the Namibian coast on October 3rd 1995. The cloud base height was around 950 m and the cloud top height varied between 1050 and 1200 m.
During the morning of October 3rd four runs were made; run 3 and 8 were flown near cloud base, and run 5 and 7 were flown near the top of the cloud. Each run is about thirteen minutes long. For these runs only FSSP, 2DC and Johnson-Williams data are available.
The particle spectra are narrow compared to the spectra measured during the Clare campaign. Generally the 2DC did not measure droplets larger than 90 μm radius. Figure 5.1 shows a typical example of a merged spectrum measured during the Namibian campaign.
The FSSP data are again tuned to the Johnson-Williams measurements. However the Namibian spectra are less weighted to the smaller particle sizes. The correction factor is therefore close to unity [De Wit and Baedi, 1999].

The scatter plots for each run separate are presented in appendix F and G. Since the correction is very small, the fits using either correction algorithm show only a slight difference. The data of run 7 and 8 clearly show different slopes, while the data of run 5 show a mixture of these slopes. The fit on run 7 is very close to the fit on only FSSP data found for the Clare campaign (figure 2.7b).
The data of run 7 are dominated by the FSSP sized particles. The total number of droplets measured by the 2DC ($N_{t,\ 2DC}$) is generally below $2{\cdot}10^4$ during this run. Figure 5.2a shows the scatter plot of all data from Namibia. If the total number of droplets measured by the 2DC is below $2{\cdot}10^4$, then the spectra are represented by a red asterisk. The green asterisks show the spectra if the 2DC measured more droplets. The red line is the least-squares fit on the 'red data' and the green line is the maximum-likelihood fit on the 'green data'.
The red fit is very close to the fit found for the FSSP data measured during Clare, see figure 2.7b. The green fit is closer to the maximum-likelihood fit found for the Clare data, that is relation (4.2).

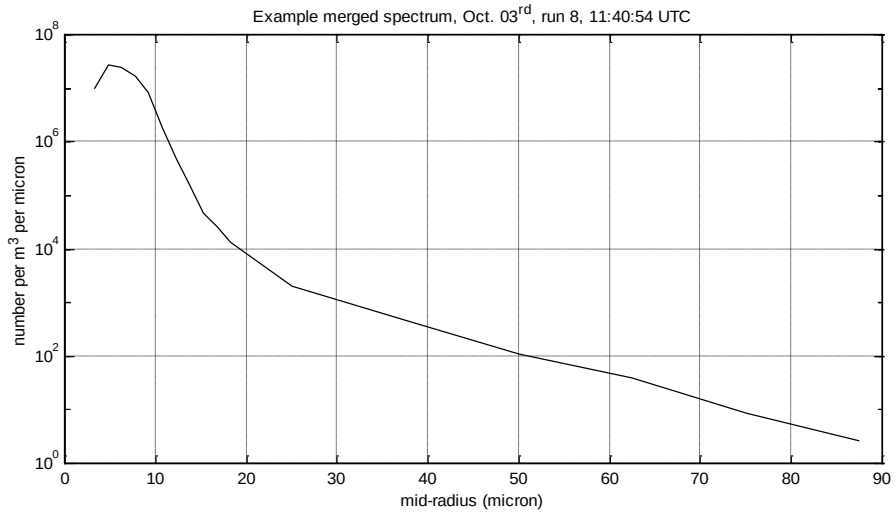

Figure 5.1: A typical example of a merged spectrum measured during the Namibian campaign, run 8, Oct. 3rd.

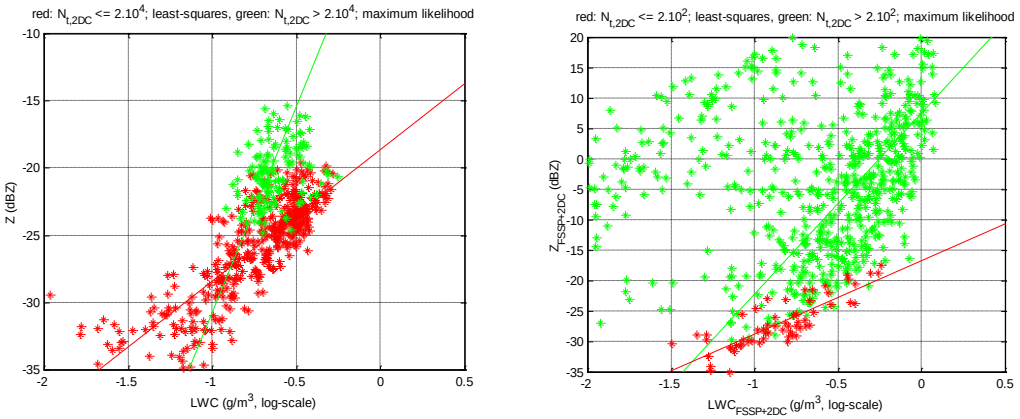

Figure 5.2: The fits if the data are sorted to the total number of droplets measured by the 2DC. Panel a shows the Namibian data. If the 2DC measured $2 \cdot 10^4$ droplets or more, the data are represented by green asterisks. Otherwise the data are shown as red asterisks. Panel b shows the Clare data, in this case the limit for the number of droplets measured by the 2DC is $2 \cdot 10^2$. The green fits represent the maximum-likelihood fits on the green asterisks and the red fits are the least-squares fits on the red asterisks. The size dependent correction is used.

The Clare data also exhibit this two sloped behaviour. However the limit for the total number of droplets measured by the 2DC is lower, in this case a limit of $2 \cdot 10^2$ droplets is taken. Figure 5.2b shows the Clare data, the green asterisks represent the data if the total number measured by the 2DC is larger than $2 \cdot 10^2$. The red asterisks show the data if the 2DC measured fewer particles.
The least-squares fits found for the case that the 2DC measured little particles are (using the size dependent correction):

Namibia:	$z = 0.014 \cdot LWC^{0.98}$	$N_{t,\,2DC} \leq 2 \cdot 10^4$	5.1
Clare:	$z = 0.022 \cdot LWC^{1.24}$	$N_{t,\,2DC} \leq 2 \cdot 10^2$	5.2

For the case that the 2DC measured a lot of particles the maximum-likelihood fits are (using the size dependent correction):

Namibia:	$z = 1.00 \cdot LWC^{3.07}$	$N_{t,\,2DC} > 2 \cdot 10^4$	5.3
Clare:	$z = 5.86 \cdot LWC^{2.98}$	$N_{t,\,2DC} > 2 \cdot 10^2$	5.4

Relationships (5.1) through (5.4) are plotted in figure 5.3. The dashed lines are the fits found for the Clare data set. In case that the 2DC measured little droplets (red) the fits for both campaigns are very similar. The black line is the least-squares fit on the Clare FSSP data (figure 2.8b).
If there are more 2DC sized particles present (green) the fits are more or less parallel, there is however a shift in reflectivity. Thus it could be that the exponent *b* in relation (1.1) is constant for different types of stratocumulus, while variable *a* is dependent on the total number of droplets measured by the 2DC. That is variable *a* depends on the average reflectivity of the cloud since the 2DC sized droplets dominate the reflectivity. The clouds observed during Clare do have a higher average reflectivity than the clouds observed during the Namibian campaign.

During Clare the reflectivity of the clouds is generally between 0 and 10 dBZ and it is always above –10 dBZ. Throughout the Namibian campaign the reflectivity is usually between –15 and –20 dBZ. So there is a rather distinct difference in the average reflectivity. Of course more data from other stratocumulus clouds are needed to really verify this idea.

The results obtained in the last two chapters may lead to the conclusion that three cases have to be taken into account determining which Z-LWC relationship is valid:

- Case 1: there are very few 2DC sized particles present and the FSSP sized particles dominate the reflectivity. In this case the least-squares fit on only the FSSP data found in chapter 2 (figure 2.8b) is valid.
- Case 2: the reflectivity is dominated by 2DC sized particles. In this case the exponent *b* is constant for different stratocumulus clouds and the variable *a* depends on the average reflectivity of the cloud.
- Case 3: there are a lot of very large (ice) particles present and very few FSSP sized droplets; the effective radius is thus very large. In this case there is no relationship between the reflectivity and the LWC.

Using the effective radius as extra parameter case 3 is easily distinguished. Furthermore ice crystals can also be identified using polarimetric techniques.
That there is no relation between the reflectivity and the LWC for case 3 is probably due to the fact that the Rayleigh approximation is not valid. As explained in chapter 2 the reflectivity from the spectra is computed using this approximation. The Rayleigh approximation is only valid if [Skolnik, 1980]:

$$\left|\frac{2\pi r}{\lambda}\right| \ll 1 \qquad 5.5$$

During run 61, 62 and 71 of October 7th, the 2DC regularly measured droplets up to 300 to 400 μm radius in the parts of the cloud where the effective radius is very large. Since the frequency of the Kestrel radar is 94.92 GHz, it is questionable if Rayleigh theory can be used.
Furthermore the reflectivity from the spectra is calculated assuming that only liquid particles were present. The density of ice crystals is however particle size dependent [Illingworth et al., 1997].
If exact Mie calculations are used to compute the reflectivity from the spectra it is still doubtful whether the LWC can be obtained with radar observations (for case 3). The reflectivity, and thus the Z-LWC relation, will be very sensitive to the number and the size of the ice crystals present. However the number and size of the ice crystals cannot be determined from radar measurements alone.

Case 1 and 2 are not so easily separated. In both regions the effective radius is well behaved. Since the effective radius is a relative figure, it does not say anything about the absolute number of 2DC sized droplets.
At first sight the average reflectivity of the cloud might be used to discriminate case 1 and 2. If only FSSP data are present, the reflectivity from the cloud is generally below –20 dBZ (figure 2.8b). The reflectivity from the cloud is higher, typically above –20 dBZ, if 2DC sized particles are present. Of course this is stated a bit too simple; from figure 5.2 can already be seen that data from case 1 and case 2 do overlap in reflectivity.
Since the terminal fall speed of cloud particles is size dependent, Doppler information may be helpful in distinguishing case 1 from case 2. For case 1 the Doppler spectrum will be narrow because there are mainly FSSP sized particles present. The presence of 2DC sized droplets broadens the Doppler spectrum.

One way could be to compute the cumulative reflectivity and plot it versus velocity. This is done for some runs of both the Clare and the Namibia data. For case 1 generally 80% of the reflectivity is reached at 10 cm/s. For case 2 only 20-30% of the reflectivity is reached at 10 cm/s. However these results were obtained after only a quick inspection of the data. A more thorough study is required to verify if the cumulative Doppler spectrum can really be used to discriminate case 1 and 2.

Further research is needed to validate this 3-case-theory and to find ways to distinguish the three cases.

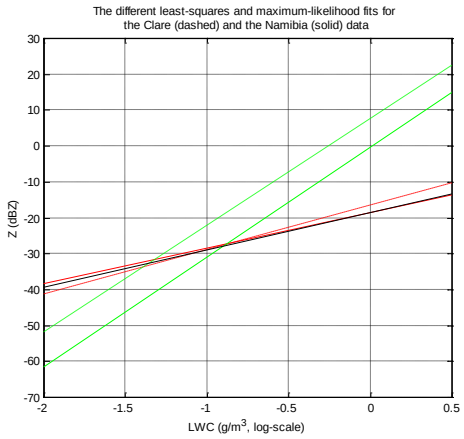

Figure 5.3: Relationships 5.1 through 5.4 in a single plot. The dashed lines are the fits found for the Clare data and the solid lines are the fits on the Namibian data. The red lines are the fits on the data if $N_{t,\ 2DC}$ is small (relation 5.1 and 5.2), the green lines are the fits on the data if $N_{t,\ 2DC}$ is large (relation 5.3 and 5.4). The black line represents the fit on the Clare FSSP data (figure 2.8b). The size dependent correction is used.

6. Results obtained with the Z-LWC relationships

In this chapter the results obtained with the relationships found in chapter 4 are presented. First relations (4.2) and (4.3) are used to calculate the LWC from the reflectivity from the spectra. Then real radar data are used to compute the LWC. The computed LWC is compared to the LWC measured by the Johnson-Williams.
Figure 6.1 shows the results for three runs using the constant correction. The calculated LWC for run 51, October 7th, is very good, see figure 6.1a. For 15% of the time the calculated LWC is within 10% of the value measured by the Johnson-Williams and for 36% of the time it is within 30% of the Johnson-Williams. The large difference between the LWC's around –2.2° longitude was to be expected, since the effective radius has a very large peak at that longitude (figure C.2c).
From figure 6.1b it is seen that the results obtained for run 61, October 7th, are very bad. This can be explained with the aid of figure C.4c. From this figure it is seen that the effective radius is very spiky during this run. So actually there is no relation between the reflectivity and the LWC during this run.
Figure C.6c shows that the effective radius is very peaked between –1.9° and –1.4° longitude, during run 71, October 7th. Thus it is to be expected that the calculated LWC will not match the measured LWC in that region. This is confirmed by figure 6.1c. Overall the computed LWC is within 10% of the measured value for 11% of the time and it is within 30% of the measured value for 17% of the time, despite the large differences between –2.0° and –1.4° longitude.

Figure 6.2 shows the same three runs using the size dependent correction. The difference between both correction schemes is very small. For run 51 the computed LWC is within 10% of the measured value for 17% of the time and it is within 30% of the value measured by the Johnson-Williams for 34% of the time. So the accuracy is comparable to the accuracy obtained using the constant correction.
That is also true for run 71. Throughout this run the calculated LWC is within 10% of the measured value for 12% of the time and for 23% of the time it is within 30% of the LWC measured by the Johnson-Williams.

The variance in the computed reflectivity can be written as [Illingworth et al., 1997]:

$$\mathrm{var}(z) = 64 \sum_i \sqrt{N_i}\, r_i^6 \qquad 6.1$$

The variance of the calculated LWC can then be obtained by substituting (6.1) in relation (4.7) and (4.8). The variance in the calculated LWC is very small, as can be seen from figure 6.3. The peak around –2.2° longitude is due to a measurement issue, as is explained in chapter 4. The variance is of the same order for both correction schemes.
The results shown so far are of course rather good, since the data from the spectra were used to find the Z-LWC relationship in the first place.

6.1 Comparison with airborne radar data

In figure 6.4 and 6.5 the results are shown if the reflectivity from the 94 GHz Kestrel radar is used to compute the LWC. As mentioned before the in-situ measurements cannot readily be compared to the Kestrel measurements.
The Kestrel radar was mounted on the Arat, while the particle probes and the Johnson-Williams were mounted on the Hercules aircraft. The aircraft were not at the

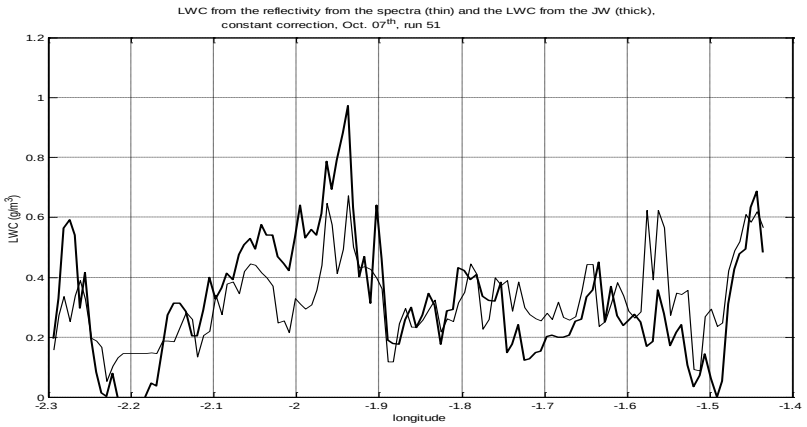

Figure 6.1a: The computed and measured LWC for run 51, Oct. 7th.

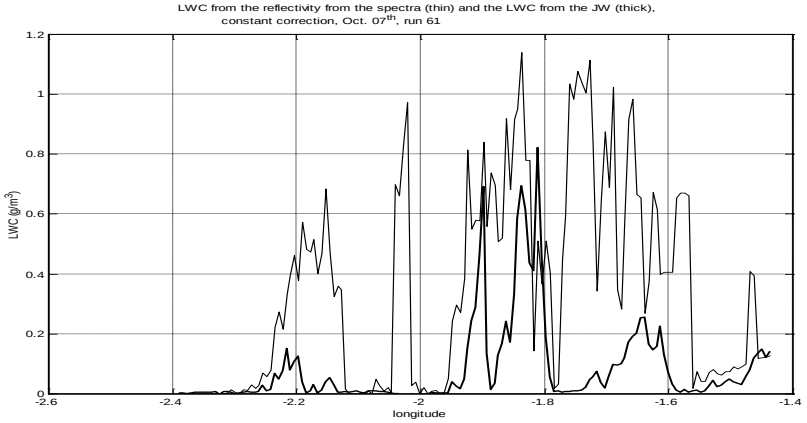

Figure 6.1b: The computed and measured LWC for run 61, Oct. 7th.

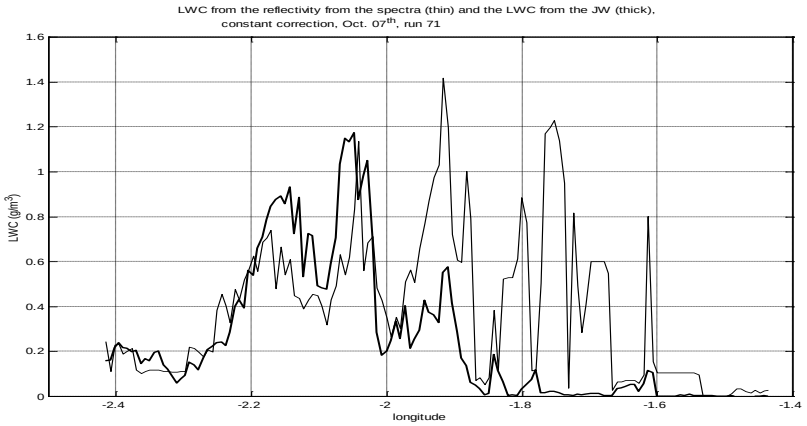

Figure 6.1c: The computed and measured LWC for run 71, Oct. 7th.

Figure 6.1: The LWC measured by the Johnson-Williams (thick) and the LWC estimated from the reflectivity from the size spectra (thin). Since the constant correction is used, the LWC is computed using relation (4.2).

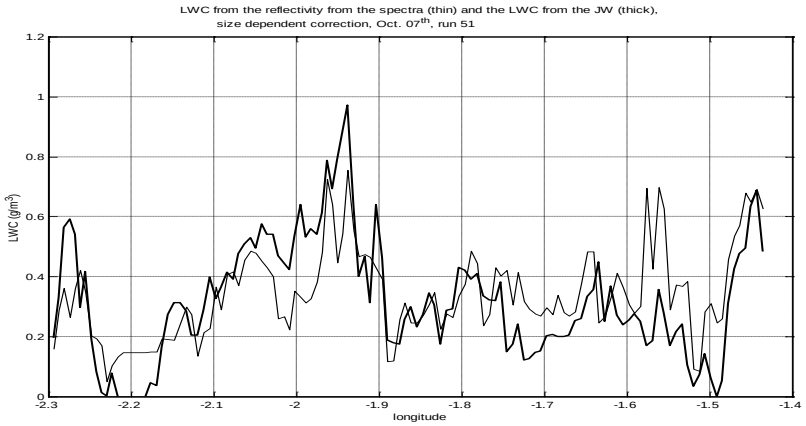

Figure 6.2a: The computed and measured LWC for run 51, Oct. 7th.

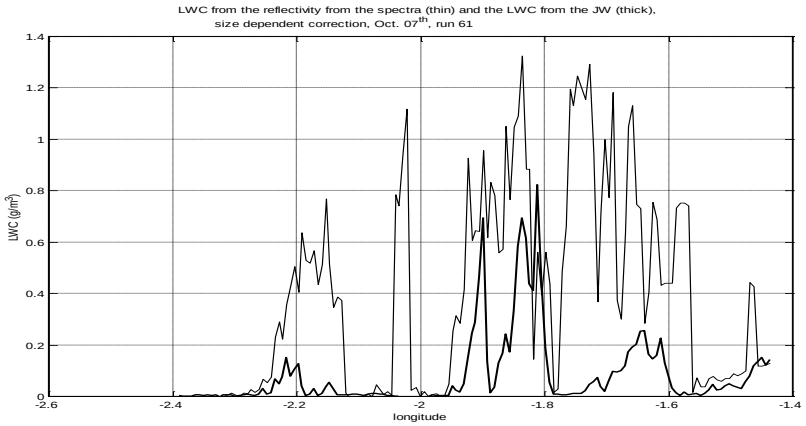

Figure 6.2b: The computed and measured LWC for run 61, Oct. 7th.

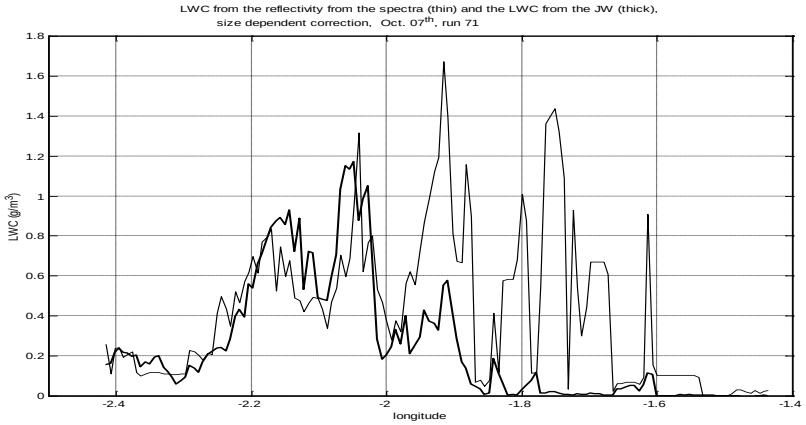

Figure 6.2c: The computed and measured LWC for run 71, Oct. 7th.

Figure 6.2: The LWC measured by the Johnson-Williams (thick) and the LWC estimated from the reflectivity from the particle size spectra (thin). The LWC is computed using relation (4.3), since the size dependent correction is used.

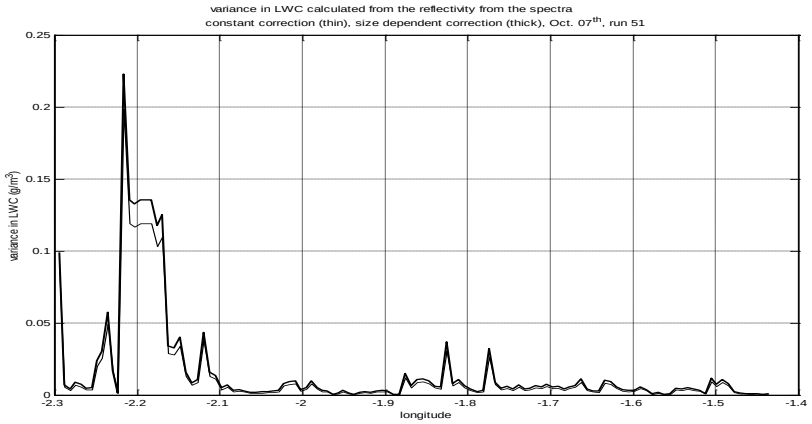

Figure 6.3: The variance of the LWC estimated from the reflectivity from the size spectra. The variance is computed using the constant correction (thin) and the size dependent correction (thick). Run 51, Oct. 7th.

same longitude simultaneously since they have different speeds. However they did arrive overhead Chilbolton (-1.44° longitude) at the same time.

Furthermore a single range resolution cell (50 m) of the Kestrel has been taken. This range cell is chosen to match the height of the Hercules as good as possible. However the height of the Hercules varies within about 100 m during a run.
As already mentioned in the introduction, the sample volumes of the Kestrel and the Johnson-Williams are not comparable. The sample volume of the Kestrel is about 10^5 times as large.
From the Kestrel data a calibration factor of 8.5 dBZ has been subtracted. This is however not yet the definitive calibration factor [A. Guyot, Clare workshop].

Figure 6.4 shows the estimated LWC (thin) and the LWC measured by the Johnson-Williams (thick) if the constant correction is used. The estimated and measured LWC for run 51, October 7th, are shown in figure 6.4a. Between –1.7° and –1.5° longitude the estimated LWC and the LWC from the Johnson-Williams agree very well. The large differences between –2.2° and –1.7° longitude can be explained with the aid of figure 6.6a.
Around –2.2° longitude the LWC is over-estimated using the Z-LWC relationship. From figure 6.6a it is seen that the reflectivity measured by the Kestrel is higher than the reflectivity computed from the spectra. This difference is probably due to the difference in height between the Kestrel resolution cell and the Hercules.
Between –2.0° and –1.7° longitude the reflectivity calculated from the spectra is higher than the reflectivity measured by the Kestrel, thus the LWC will be under-estimated using the Z-LWC relationship. This is confirmed by figure 6.4a.
During run 61, October 7th, the effective radius is very spiky (figure C.4c), so effectively there will be no relationship between the reflectivity and the LWC. Figure 6.4b shows indeed that the estimated LWC differs from the LWC measured by the Johnson-Williams.
During run 71, October 7th, the reflectivity measured by the Kestrel is generally lower than the reflectivity from the spectra. From figure 6.4c it is seen that the LWC is indeed under-estimated during this run. However between –1.9° and –1.4° longitude the LWC is over-estimated using the Z-LWC relationship. This is due to the fact that during this part of the run the Z-LWC relationship is not valid, since the effective radius is not well-behaved (figure C.6c).

The results obtained if the size dependent correction is used are shown in figure 6.5. From figure 6.4 and 6.5 can be seen that the differences between both correction schemes are very small.

The estimated and measured LWCs for run 52, 62 and 72 are included in appendix J. Plots of the reflectivity calculated from the spectra and the reflectivity measured by the Kestrel for these runs can also be found appendix J.
During run 52, October 7th, the reflectivity from the spectra is a bit higher than the reflectivity measured by the Kestrel. Therefore the LWC is under-estimated during this run.
During run 62, October 7th the Z-LWC relationship is not valid, since the effective radius shows a very spiky behaviour (figure C.5c). And indeed there is a large difference between the estimated LWC and the measured LWC.
Throughout run 72, October 7th, the reflectivity measured by the Kestrel and the reflectivity from the spectra do not match very well. Therefore the estimated and measured LWC do not match very well also.
The differences between both correction algorithms are again very small.

Figure 6.7a shows the histogram of the LWC estimated from the Kestrel data for run 51 and 52, October 7th. This histogram exhibits a large peak around 0.25 g/m^3. According to [Cavazzini et al., 1997] the average LWC in stratocumulus clouds is 0.2 to 0.3 g/m^3, while the maximum LWC is 1.0 g/m^3. Thus the results obtained with the Kestrel data agree very well with the literature.
The histogram of the LWC measured by the Johnson-Williams for run 51 and 52, October 7th is shown in figure 6.7b. This histogram is not so well behaved as the histogram of the Kestrel data. This is probably due to under-sampling by the Johnson-Williams.
The Johnson-Williams produces a measurement every 5 seconds, while the Kestrel produces measurements every second. Furthermore the sample volume of the Johnson-Williams is very small, as already explained in the introduction.

Summarising it is very difficult to compare the estimated and measured LWC since the Kestrel and Johnson-Williams measurements are not from exactly the same spot. Hence it could be that the Johnson-Williams and the Kestrel did not measure the same event. Furthermore their sample volumes are not comparable.
The difference between the computed reflectivity and the measured reflectivity could also be due to the calibration factor. Maybe the calibration factor is too large, since the reflectivity measured by the Kestrel is usually lower than the reflectivity calculated from the spectra.
Next to that the Kestrel data are not corrected for attenuation inside the cloud. According to [Illingworth et al., 1997] the specific one-way attenuation for 94 GHz is about 4.82 dB/km/(g/m^3) at a temperature of 0 ºC. So, during the events studied in this report, the maximum two-way specific attenuation of the Kestrel signal is 1 dB. Thus the attenuation of the radar signal cannot cause the large differences between the reflectivity from the size spectra and the reflectivity measured by the Kestrel.
If the computed reflectivity and the measured reflectivity are comparable, then the estimated and the measured LWC match very well also.

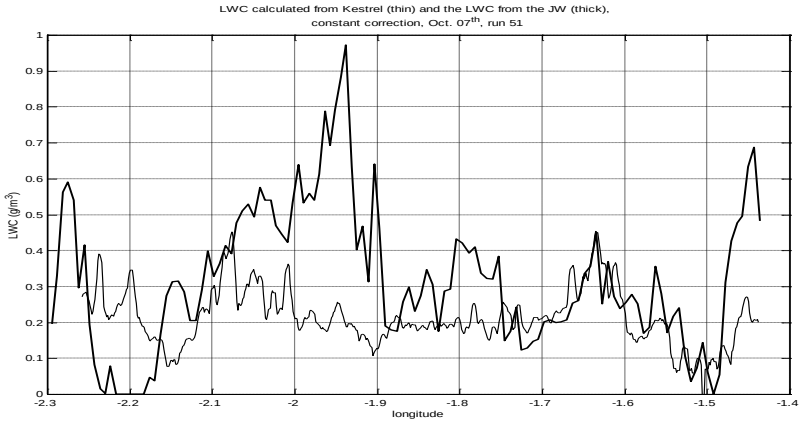

Figure 6.4a: The estimated and measured LWC for run 51, Oct. 7th.

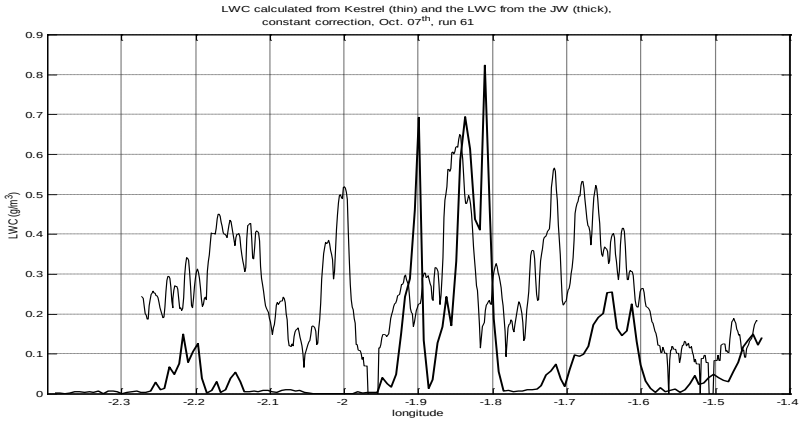

Figure 6.4b: The estimated and measured LWC for run 61, Oct. 7th.

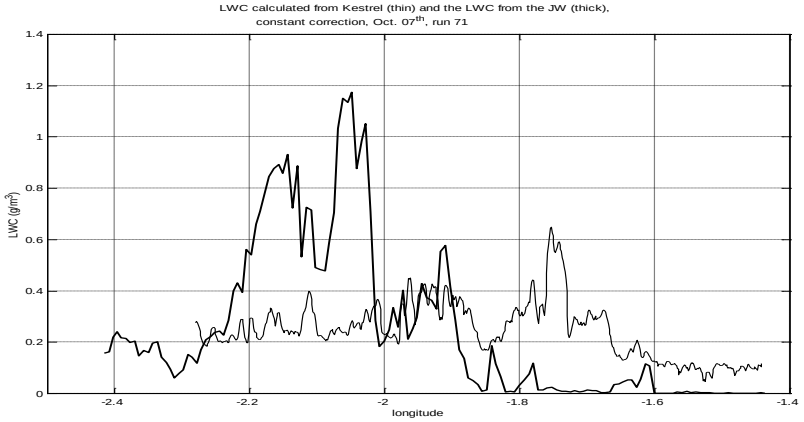

Figure 6.4c: The estimated and measured LWC for run 71, Oct. 7th.

Figure 6.4: The LWC measured by the Johnson-Williams (thick) and the LWC estimated from the 94 GHz Kestrel data (thin). The LWC is estimated using relation (4.2) (constant correction).

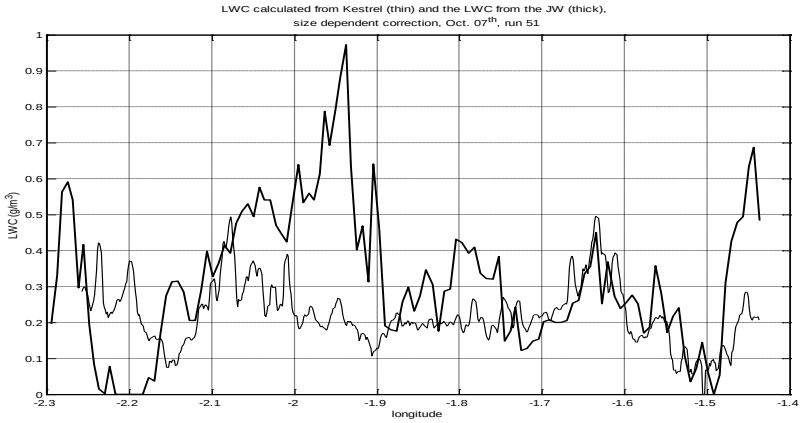

Figure 6.5a: The estimated and measured LWC for run 51, Oct. 7th.

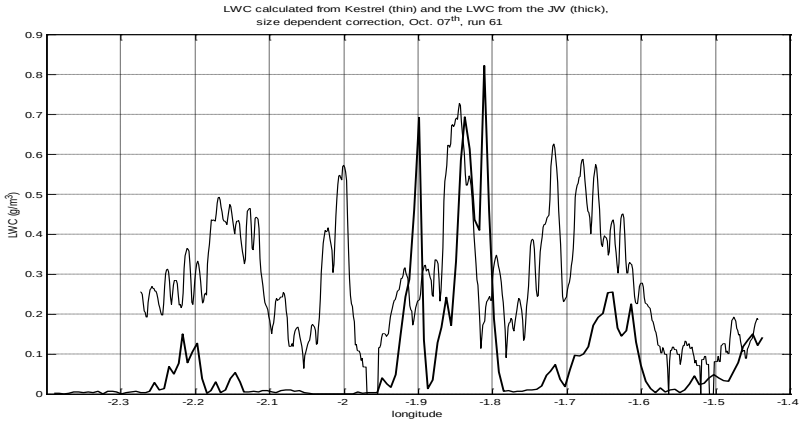

Figure 6.5b: The estimated and measured LWC for run 61, Oct. 7th.

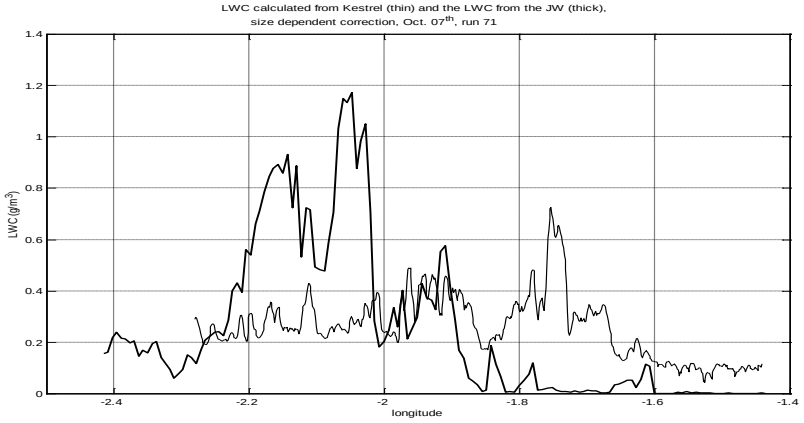

Figure 6.5c: The estimated and measured LWC for run 71, Oct. 7th.

Figure 6.5: The LWC measured by the Johnson-Williams (thick) and the LWC estimated from the 94 GHz Kestrel data (thin). The LWC is estimated using relation (4.3) (size dependent correction).

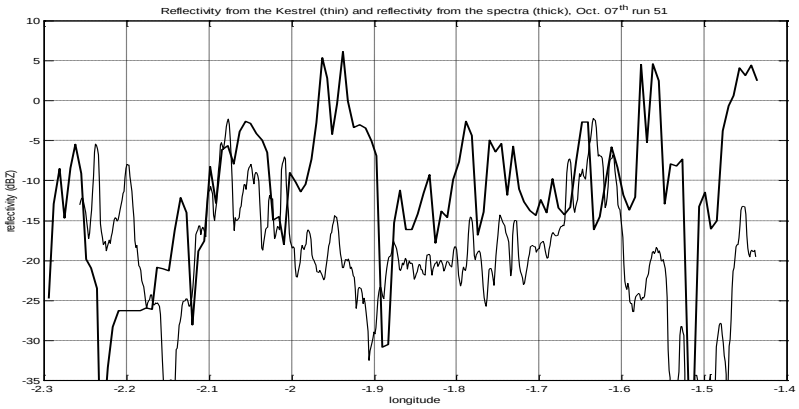

Figure 6.6a: The computed and measured reflectivity for run 51, Oct. 7th.

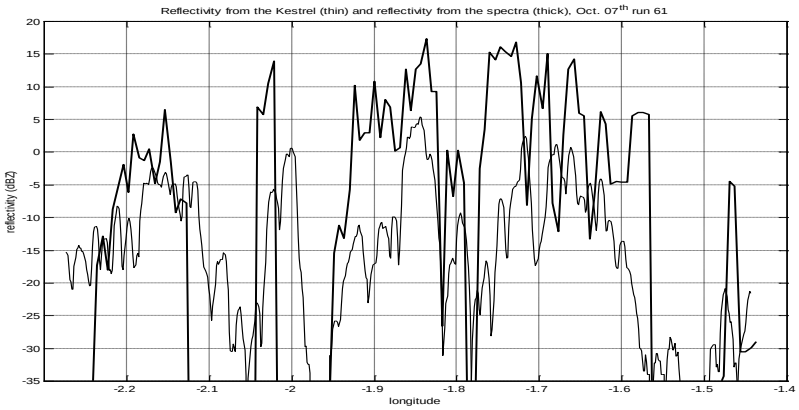

Figure 6.6b: The computed and measured reflectivity for run 61, Oct. 7th.

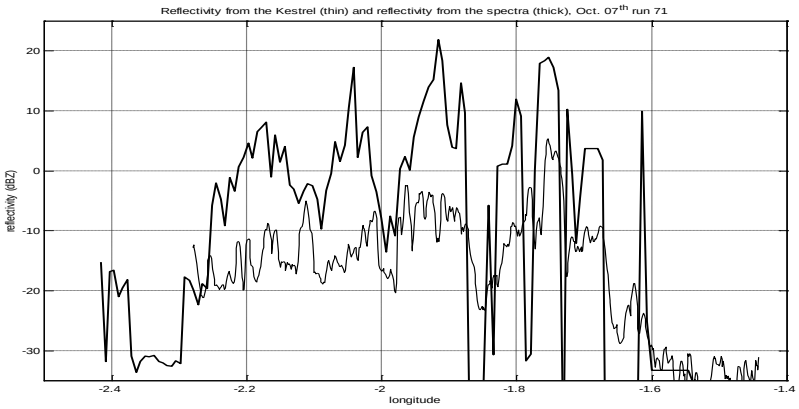

Figure 6.6c: The computed and measured reflectivity for run 71, Oct. 7th.

Figure 6.6: The reflectivity measured by the 94 GHz Kestrel radar (thin) and the reflectivity calculated from the particle size spectra (thick).

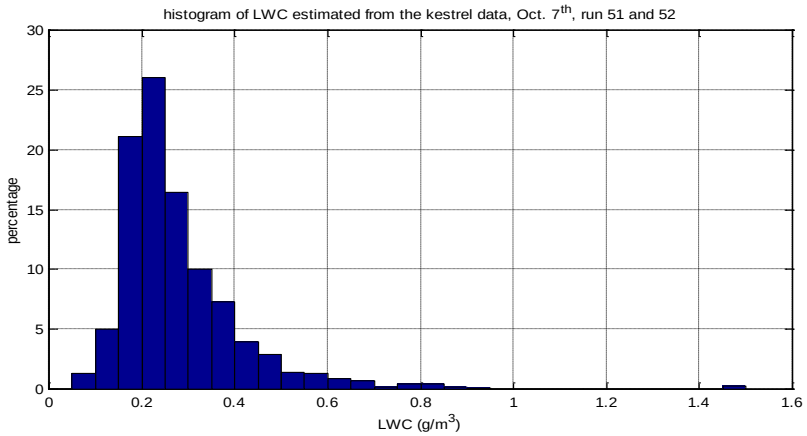

Figure 6.7a: Histogram of the LWC estimated from the Kestrel data, using relation (4.2) (constant correction), Oct. 7th, run 51 and 52.

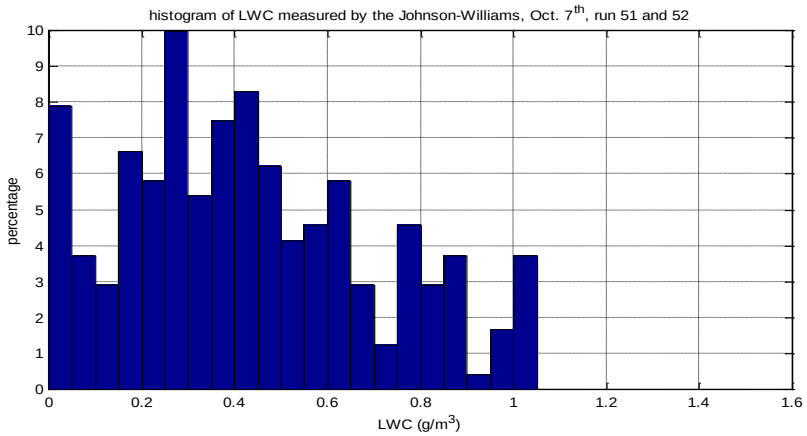

Figure 6.7b: Histogram of the LWC measured by the Johnson-Williams, Oct. 7th, run 51 and 52.

Figure 6.7: Histograms of the estimated and the measured LWC.

6.2 Comparison of ground based radar and radiometer data

In this paragraph the Z-LWC relationships found in chapter 4 are validated using ground based radar and radiometer data. The 94 GHz Miracle radar and the 93 GHz radiometer were both situated at Chilbolton. Since they were close together, they must have been sampling the same events.
In appendix K images of the Miracle radar are included. For the Miracle the far-field approximation is only valid beyond a range of 900 m [Hogan et al., 1999]; note that the measurements start at 984 m.

The cloud liquid water path (LWP) is calculated from the Miracle data using the Z-LWC relationships. Then this LWP is compared to the cloud liquid water path computed from the radiometer data. To obtain the LWP, the LWC is integrated over the cloud:

$$LWP = \int_{h_b}^{h_t} LWC(h)\,dh \qquad [g/m^2] \qquad 6.4$$

where *h* is the height [m]. Since the data from the Miracle is used to calculate the LWC, relation (6.4) reduces to a summation over the height cells of the Miracle:

$$LWP = \sum_i LWC_i \cdot h_{cell} \qquad 6.5$$

where h_{cell} is the height of the radar resolution cells and LWC_i is the LWC in resolution cell *i*.
In this case the attenuation caused by the cloud particles cannot be neglected. Therefore the Miracle data are corrected using the value mentioned in [Illingworth et al., 1997]: 4.82 dB/km/(g/m^3). For this correction it is assumed that the average LWC is 0.3 g/m^3 and that the average cloud base height is 1,700 m.

Figure 6.8 shows the LWP computed from the corrected Miracle data. The thin line represents the LWP if relation (4.2) is used and the thick line shows the LWP if relation (4.3) is applied. As can be seen the difference between using relation (4.2) or (4.3) to compute the LWP is very small. Only for high values of the LWP the differences are not negligible, see the peak around 13.90 UTC.
In figure 6.9 the LWP from the 93 GHz radiometer data and the LWP from the Miracle data are shown. The LWP is calculated from the Miracle data using relationship (4.2). The LWP's agree quite well, however for low values of the LWP there is a difference of about 60 g/m^2.
The scatter plot of the LWP from the Miracle and the LWP from the radiometer data is included as figure 6.10. This plot confirms that there is a difference between the LWP from the radiometer and the LWP from the Miracle for low values of the LWP. At this point it is not certain if this difference is due to the retrieval method or due to some sort of offset in the measurement set up.

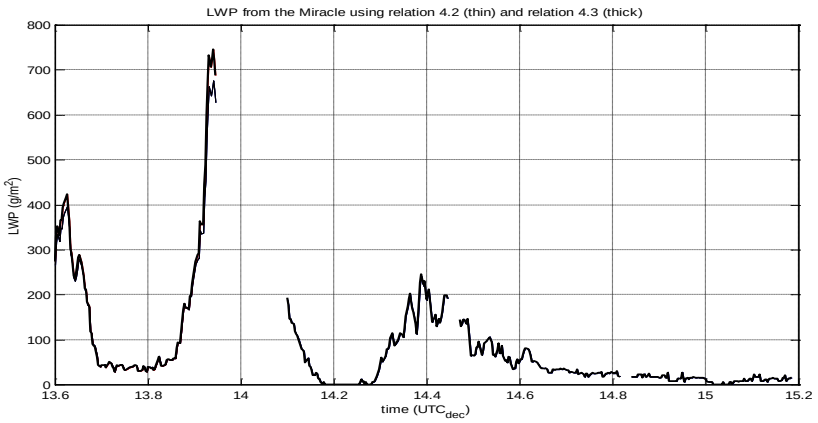

Figure 6.8: The LWP computed from the Miracle data, Oct. 7th. The thin line shows the LWP if the Z-LWC relation for the constant correction is used and the thick line represents the LWP if the relation for the size dependent correction is applied.

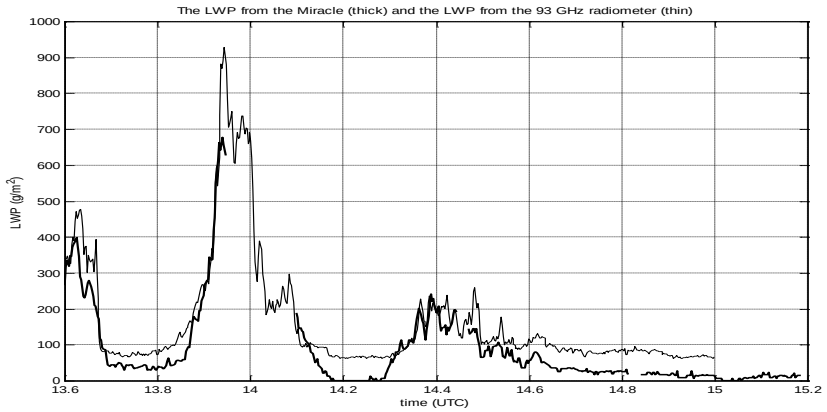

Figure 6.9: The LWP calculated from the Miracle data and the LWP computed from the 93 GHz radiometer data, Oct. 7th. The thin line shows the LWP from the radiometer and the thick line represents the LWP from the Miracle data if the Z-LWC relation for the constant correction is applied.

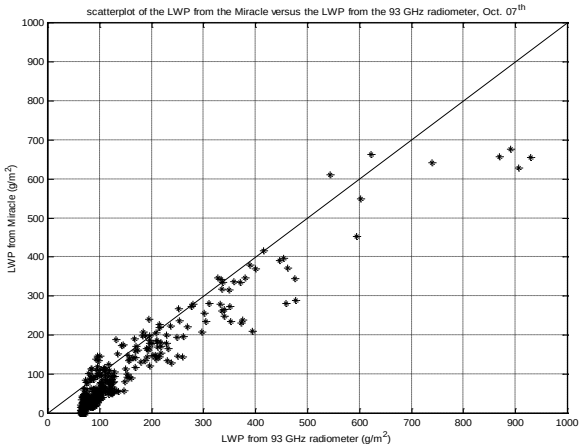

Figure 6.10: The scatter plot of the LWP from the 93 GHz radiometer versus the LWP computed from the Miracle data using the relationship for the constant correction.

7. Conclusions and recommendations

If only FSSP data are taken into account, it seems that there is a relationship between the reflectivity and the LWC that is generally valid. The relationships found for the different runs made during Clare are very similar.
Furthermore the fits on the FSSP data for the Clare campaign and the Namibian campaign are also very alike. The different relationships found for the FSSP data are (figure 2.8 and 5.2):

$$z = 0.0084 \cdot LWC^{1.04}$$; Clare, constant correction 7.1

$$z = 0.014 \cdot LWC^{1.04}$$; Clare, size dependent correction 7.2

$$z = 0.014 \cdot LWC^{0.98}$$; Namibia 7.3

The difference between the correction schemes is mainly a shift in reflectivity. In both cases the LWC is tuned to the Johnson-Williams measurements. However using the size dependent technique the large droplets are corrected more than the small droplets, thus the reflectivity from the spectra will increase due to the r^6 dependency.

On the other hand if the 2DC data are also taken into account there is no generally valid Z-LWC relationship. Although the fits found for Clare and the Namibian campaign are parallel, thus it could be that the exponent *b* in relationship (1.1) is constant for different stratocumulus clouds.
There is a shift in reflectivity between the fits found for Clare and the Namibian campaign. During Clare the reflectivity of the clouds is, on average, higher than the reflectivity of the clouds observed throughout the Namibian campaign. So apparently variable *a* in relation (1.1) is dependent on the average reflectivity of the cloud.
The points in the Z-LWC scatter plot that are far off the fit generally have a large effective radius. So effectively there is no relation between the reflectivity and the LWC, if the effective radius is very large. Thus the effective radius can be used as a parameter to verify if the Z-LWC relation can be used to estimate the LWC. In [Baedi, 1999] a method is described to obtain the effective radius from radar and lidar measurements. However since the lidar signal attenuates very quickly in the cloud, this method can only be used in the edges of the cloud.

Thus it seems that there are three different cases that have to be taken into account determining which Z-LWC relationship is valid:

- Case 1: there are very few 2DC sized particles present, thus the FSSP particles dominate the reflectivity. In this case the Z-LWC relation found for only the FSSP data is valid (figure 2.8).
- Case 2: the 2DC sized droplets dominate the reflectivity. In this the exponent *b* is constant for different stratocumulus, while the variable *a* depends on the average reflectivity of the observed cloud (figure 5.2).
- Case 3: there are only little FSSP sized particles present and a lot of large droplets; the effective radius is very large. In this case there is no relationship between the reflectivity and the LWC.

Case 3 can be easily discriminated using the effective radius. Furthermore the presence of ice crystals can be detected using polarimetric techniques. That there is no relationship between the reflectivity and the LWC in this case is probably due to the fact that the Rayleigh approximation is not valid.
Even if exact Mie calculations are used to compute the reflectivity from the spectra, it is still not to be expected that there will be a Z-LWC relationship for case 3. The computed reflectivity, and thus the Z-LWC relation, will be very sensitive to the

number and size of the ice crystals present in the cloud. However from radar observations the number and size of ice crystals cannot be determined.
However case 1 and 2 ca not be readily discriminated. In both case 1 and 2 the effective radius is well-behaved. Maybe the reflectivity can be used to identify case 1 and 2. If only FSSP data are present (case 1) the average reflectivity of the cloud is below –20 dBZ. If the reflectivity is dominated by 2DC sized particles (case 2) the average reflectivity of the cloud is higher, typically above –20 dBZ. This is however stated too simple since there is not a distinct difference in reflectivity between case 1 and case 2 (figure 5.2).
At first sight Doppler information may be used to discriminate case 1 and 2. For case 1 the cumulative reflectivity reaches 80% at 10 cm/s. For case 2 only 20-30% of the reflectivity is reached at 10 cm/s.

The Z-LWC relationships found for Clare, taking the 2DC data into account, are (figure 4.9):

$$z = 28.26 \cdot LWC^{4.88}\text{; constant correction} \qquad 7.4$$

$$z = 14.82 \cdot LWC^{4.57}\text{; size dependent correction} \qquad 7.5$$

There is only a slight difference using either correction technique. Since the 2DC sized droplets dominate the reflectivity, the reflectivity from the spectra will barely increase if the size dependent correction is used.

Relationships (7.4) and (7.5) are not easily verified. The Kestrel radar and the Johnson-Williams were mounted on different aircraft. Since the aircraft have different speeds they were not at the same longitude simultaneously. Furthermore a single range resolution cell (50 m) of the Kestrel is compared to the Johnson-Williams measurements. The range cell is chosen to match the height of the Hercules, which carried the Johnson-Williams, as good as possible. However the height of the Hercules varies about 100 m throughout a run.
Generally the estimated LWC does not match the measured LWC very well. This is due to the difference between the reflectivity calculated from the spectra and the reflectivity measured by the Kestrel. This difference is probably caused by the fact that the Kestrel and the Johnson-Williams measurements are not from exactly the same spot. However during most runs the reflectivity measured by the Kestrel is lower than the reflectivity calculated from the spectra. Thus it could also be that the calibration factor is too large, since it is not yet the definitive factor [A. Guyot, Clare workshop].
If the reflectivity from the spectra and the reflectivity measured by the Kestrel are comparable, then the estimated and the measured LWC match very well.
The histogram of the LWC computed from the Kestrel data shows a large peak around 0.25 g/m^3 and the maximum value is 0.9 g/m^3. These values agree very well with typical values mentioned in literature.

The Z-LWC relationships are also validated ground based radar and radiometer data. Since Miracle radar and the 93 GHz radiometer were close together, they must have been observing the same events. The LWP computed from the Miracle data and the LWP calculated from the radiometer data are compared. The results are good, the LWP's are in good agreement. Only for low values of the LWP there is a difference of about 60 g/m^2. Further research is needed to see whether this difference is due to the retrieval method. The difference between the LWP computed using relationship (7.4) and the LWP calculated applying relation (7.5) is negligible.

It is not possible to estimate the LWC directly from the Doppler spectrum. There are techniques to remove the spectral broadening due to turbulence and retrieve the particle size spectrum from the Doppler spectrum. Using the retrieved particle size spectrum the LWC and the effective radius can be computed. These techniques are however still in development.

More data of different stratocumulus clouds should be investigated to verify the idea that the exponent *b* in relationship (1.1) is constant for different types of stratocumulus. And if this is true then should be looked into how the variable *a* in relation (1.1) is dependent on the average reflectivity of the cloud.
Furthermore the 3-case-theory can be validated if more data of stratocumulus are available. Then should also be investigated if Doppler information can be used to discriminate between the cases.

The maximum-likelihood fit presented in this report is very simple. A better maximum-likelihood fit should be developed to obtain the Z-LWC relationship more accurate.

The fact that the 2DC sized droplets seem to just pop up once in a while could be due to under-sampling, since in clouds the 2DC sized droplets are rare and the sample volume of the 2DC is very small. In [Baedi, De Wit and Baptista] it is shown that the standard deviation of the measurements increases with particle size. For the last bins of the 2DC the standard deviation is very large.
If the 2DC really under-samples, the raw 2DC data should be averaged over a longer period. Maybe the averaging time should be made size dependent. Finally should be looked into the effect of a longer averaging time on the Z-LWC scatter plot and the Z-LWC relationships.

8. References

Babb, D.M., Verlinde, J., Albrecht, B.A., *Retrieval of cloud microphysical parameters from 94-GHz radar Doppler power spectra*, J. Atmospheric and Oceanic Technology, Volume 16, p489-503, 1999a

Babb, D.M., Miles, N.L., Verlinde, J., *A constrained linear inversion algorithm for removing turbulent broadening in Doppler power spectra*, Proceedings IRCTR-Cloud Remote Sensing Symposium, Delft, 21-22 October 1999b

Baedi, R.J.P., *Estimating the effective radius by combining radar and lidar observations for the stratocumulus clouds during Clare '98*, Internal report IRCTR-Delft University of Technology, 1999

Baedi, R.J.P., Wit, J.J.M. de, Poiares Baptista, J.P.V., *Comparison of micro-physical and macro-physical measurements during the Cloud Lidar and Radar Experiment*, Internal report ESTEC-European Space Agency, 1999

Cavazzini, P., Prodi, F., Schmid, W., Barthazy, E., *Macrophysical and microphysical properties of clouds*, Internal report ESTEC-European Space Agency, 1997

Doviak, R.J., Zrnic, D.S., *Doppler radar and weather observations*, Academic Press INC., 1993

Fox, N.I., Illingworth, A.J., *The retrieval of stratocumulus cloud properties by ground based cloud radar*, J. Applied Meteorology, Vol. 36, p485-492, 1997

Francis, P.N., *A summary of the cloud microphysics data collected during CLARE '98 by the UKMO C-130 aircraft*, Proceedings ESTEC-Clare workshop, Noordwijk, 12-13 September 1999

Hogan, R.J., Illingworth, A.J., Sauvageot, H., *Stratocumulus liquid water content from dual wavelength radar*, Proceedings ESTEC-Clare workshop, Noordwijk, 12-13 September 1999

Illingworth, A.J., Hignett, P., *Clare '98, Experimental plan for October 1998*, Internal report University of Reading, 1998

Illingworth, A.J., Liu, C-L., Astin, I., Richards, B., *Study of the critical requirements for a cloud radar*, Internal report ESTEC-European Space Agency, 1997

Moss, S.J., Brown, P.R.A., Johnson, D.W., Lauchlan, D.R., Martin, G.M., Pickering, M.A., Spice, A., *Cloud microphysics measurements on the MRF C-130: Working Group Report*, Meteorological Research Flight, MRF Technical note no. 12, 1993

Ouldbridge, M., *An introduction and guide to the Johnson-Williams liquid water content meter*, Meteorological Office, Met. O. 15 Internal report no. 41, 1982

Pruppacher, H.R., Klett, J.D., *Microphysics of clouds and precipitation*, Kluwer Academic Publishers, 1997

Rogers, R.R., A *short course in cloud physics*, Oxford Pergamon, 1976

Sauvegeot, H., Omar, J., *Radar reflectivity of cumulus clouds*, J. Atmospheric and Oceanic Technology, Vol. 4, p246-272, 1987

Skolnik, M.I., *Introduction to radarsystems*, McGraw-Hill International Editions, p33-34, 1980

Wit, J.J.M. de, Baedi, R.J.P., *Comparison of micro-physical and macro-physical measurements of clouds during the Cloud Lidar and Radar Experiment, Part II*, Internal report IRCTR-Delft University of Technology, 1999

Appendix A. Z-LWC relation constant correction

In this appendix the Z versus LWC scatter plots for each run are presented. In each figure the least-squares fit is shown. Using this fit the Z-LWC relation can be written as: $z = a^*LWC^b$, where *a* and *b* are given in the title of each figure. The root-mean-square (rms) error is also computed and printed in the title of each plot. If only the FSSP data are taken into account then data with Z < -45 dBZ or LWC < 0.01 g/m^3 are neglected. If the 2DC data are also taken into account, the data with Z < -35 dBZ or LWC < 0.01 g/m^3 are discarded.
For run 52, October 13th only one scatter plot is included, since the 2DC did not measure any droplets during that run.

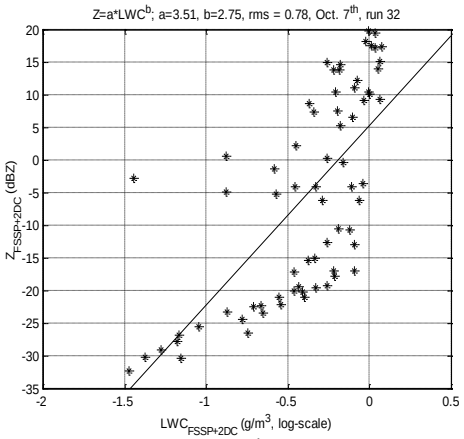

Fig. A.1: Run 32, Oct. 7th, rms- error is 0.78.

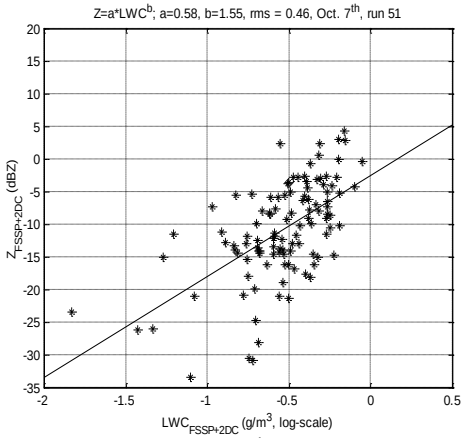

Fig. A.2: Run 51, Oct. 7th, rms- error is 0.46.

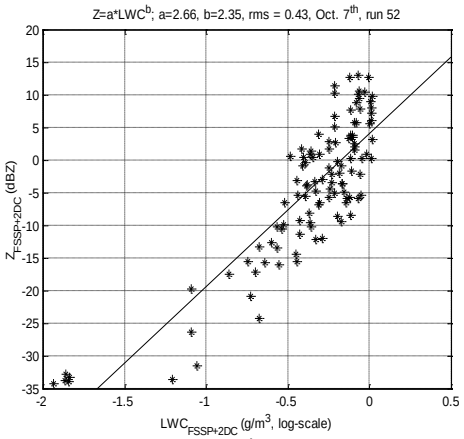

Fig A.3: Run 52, Oct. 7th, rms- error is 0.43.

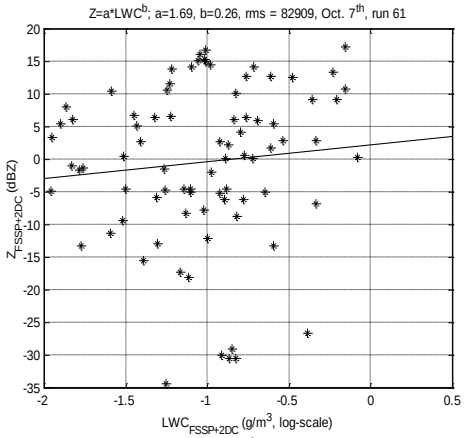

Fig A.4: Run 61, Oct. 7th.

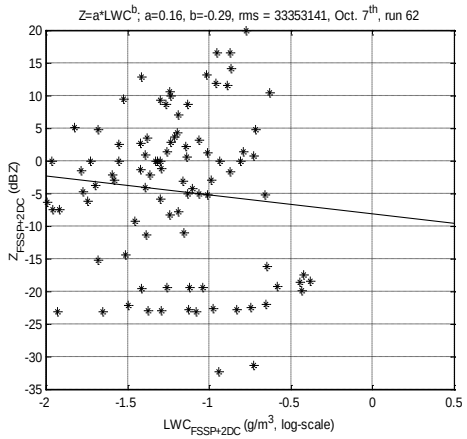

Fig A.5: Run 62, Oct. 7th.

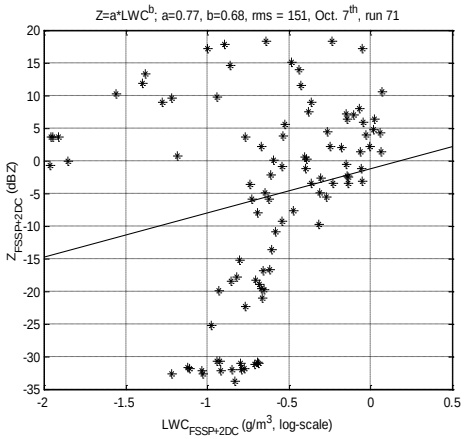

Fig A.6: Run 71, Oct. 7th, rms- error is 151.

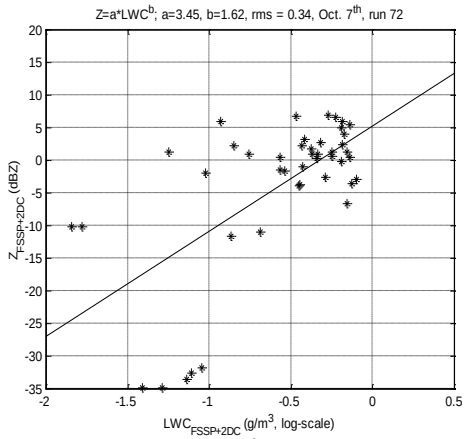

Fig A.7: Run 72, Oct. 7th, rms- error is 0.34.

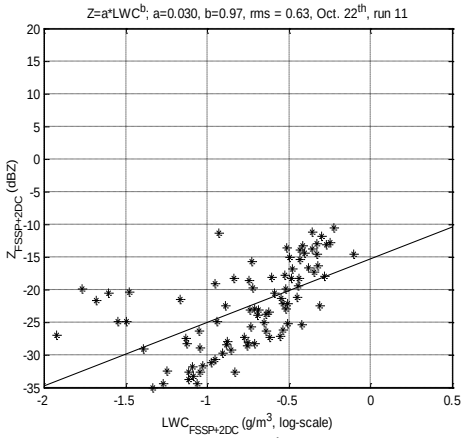

Fig A.8: Run 11, Oct. 22nd, rms- error is 0.63.

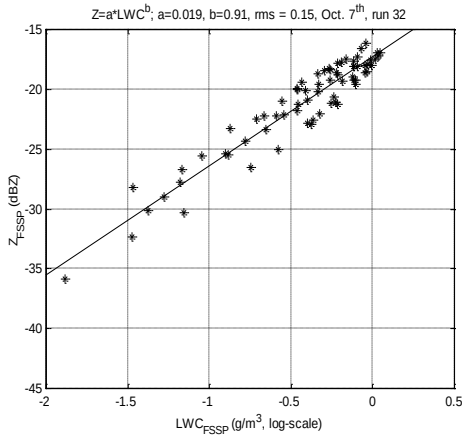

Fig. A.9: Run 32, Oct. 7th, rms- error is 0.15.

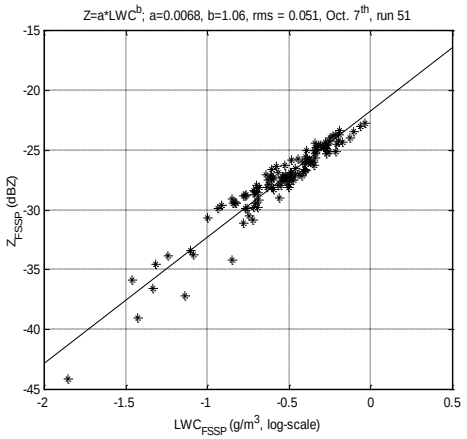

Fig. A.10: Run 51, Oct. 7th, rms- error is 0.05.

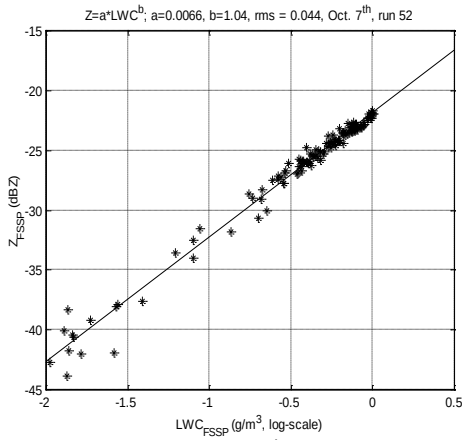

Fig. A.11: Run 52, Oct. 7th, rms- error is 0.04.

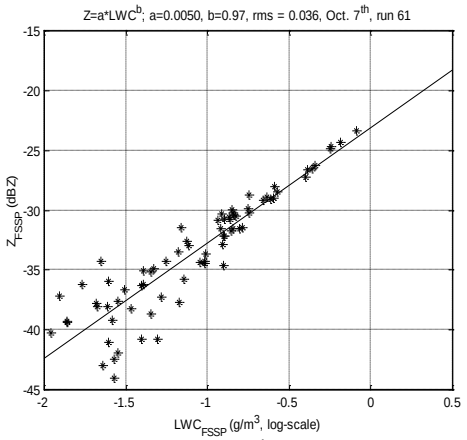

Fig. A.12: Run 61, Oct. 7th, rms- error is 0.04.

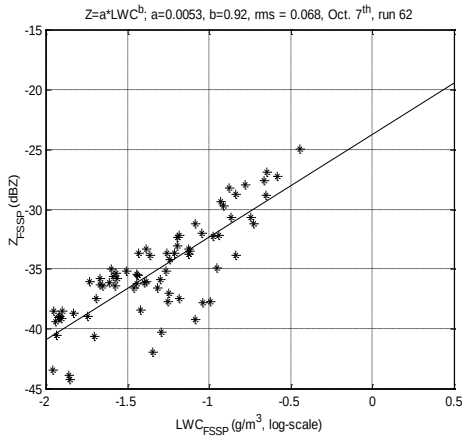

Fig. A.13: Run 62, Oct. 7th, rms- error is 0.07.

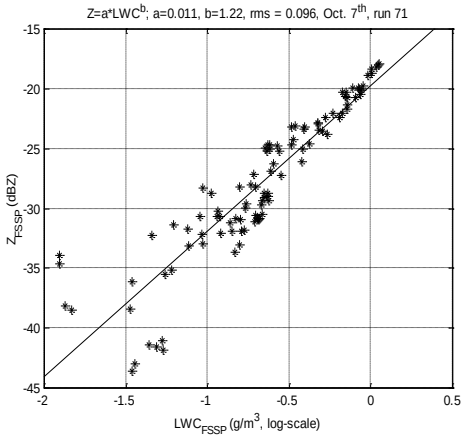

Fig. A.14: Run 71, Oct. 7th, rms- error is 0.10.

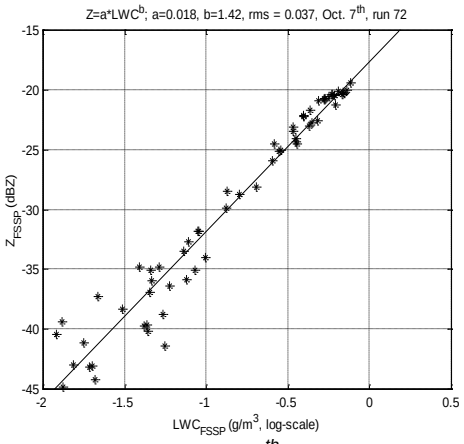

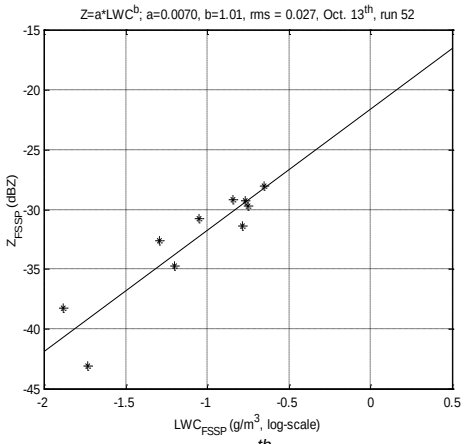

Fig. A.15: Run 72, Oct. 7th, rms- error is 0.04. *Fig. A.16: Run 52, Oct. 13th, rms- error is 0.03.*

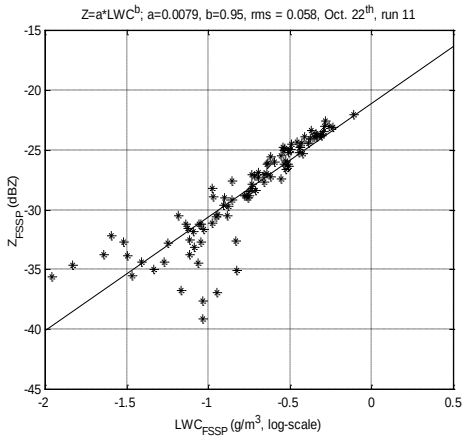

Fig. A.17: Run 11, Oct. 22nd, rms- error is 0.06.

Appendix B. Z-LWC relation size dependent correction

In this appendix the Z versus LWC scatter plots for each run are presented. In each figure the least-squares fit is shown. Using this fit the Z-LWC relation can be written as: $z = a^*LWC^b$, where *a* and *b* are given in the title of each figure. The root-mean-square (rms) error is also computed and printed in the title of each plot. If only FSSP data are taken into account, then data with Z < -45 dBZ or LWC < 0.01 g/m^3 are discarded. If the 2DC data are also taken into account, data with LWC < 0.01 g/m^3 or Z < -35 dBZ are neglected.
During run 52, October 13th the 2DC did not measure anything thus for that run only one scatter plot is included.

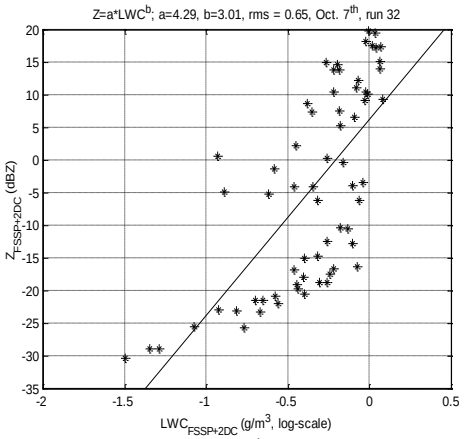

Fig. B.1: Run 32, Oct. 7th, rms- error is 0.65.

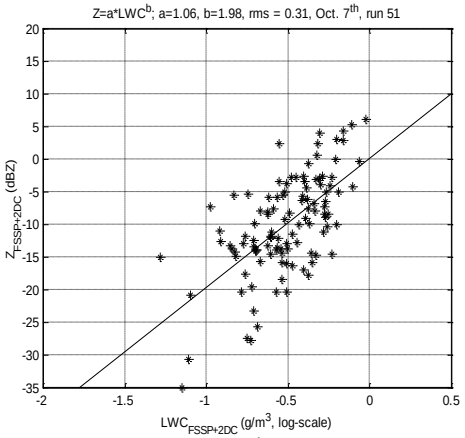

Fig. B.2: Run 51, Oct. 7th, rms- error is 0.31.

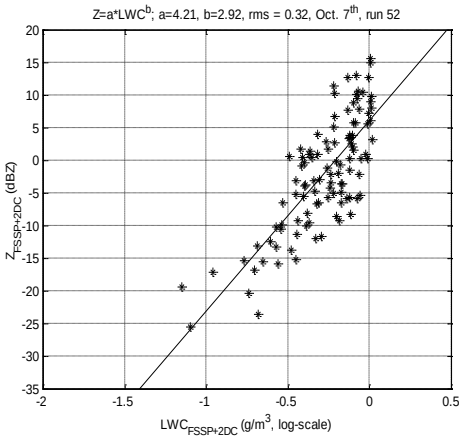

Fig. B.3: Run 52, Oct. 7th, rms- error is 0.32.

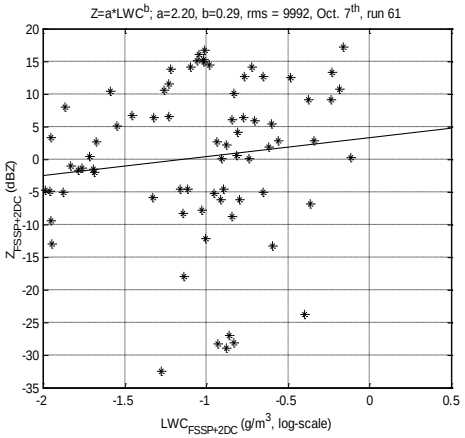

Fig. B.4: Run 61, Oct. 7th.

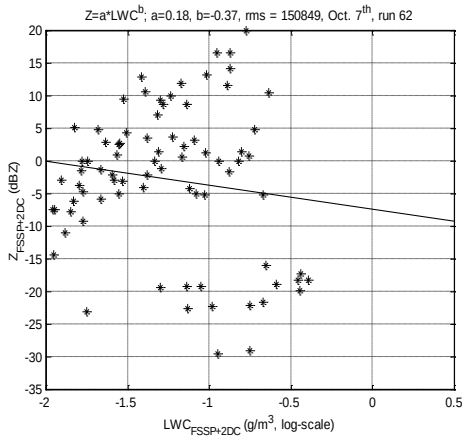

Fig. B.5: Run 62, Oct. 7th.

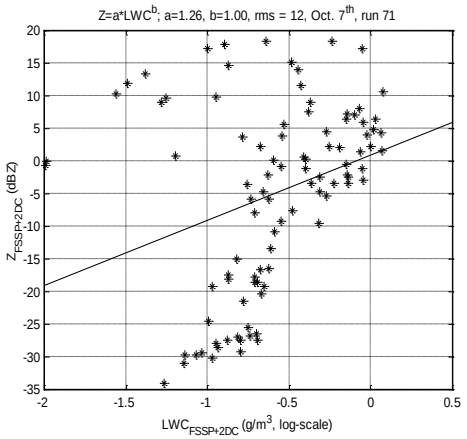

Fig. B.6: Run 71, Oct. 7th, rms- error is 12.

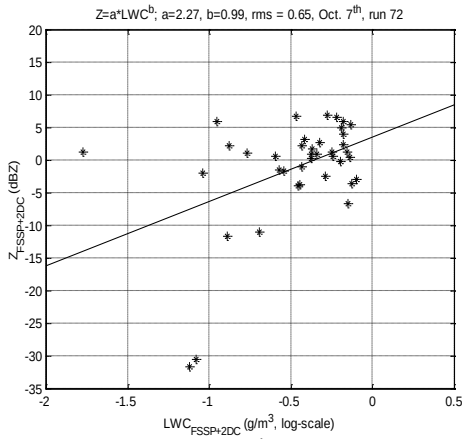

Fig. B.7: Run 72, Oct. 7th, rms- error is 0.65.

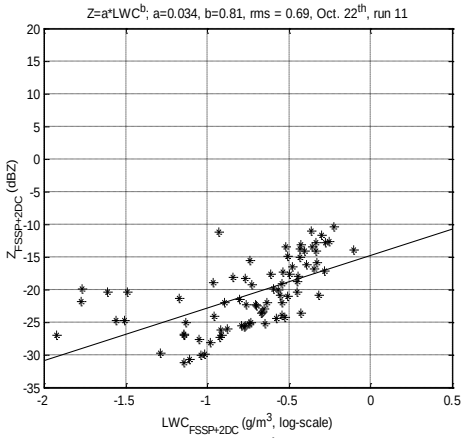

Fig. B.8: Run 11, Oct. 22nd, rms- error is 0.69.

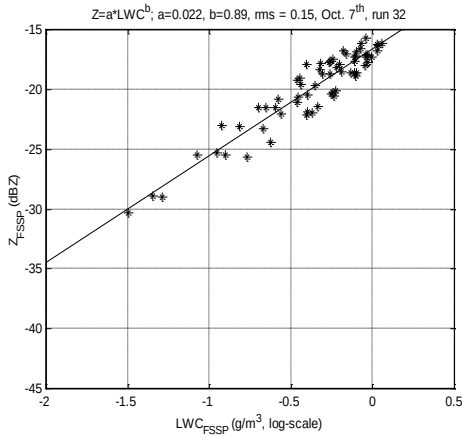

Fig. B.9: Run 32, Oct. 7th, rms- error is 0.15.

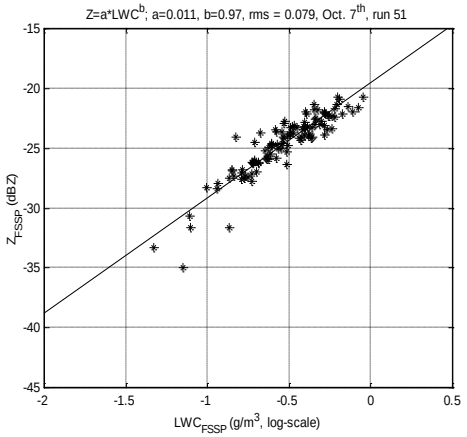

Fig. B.10: Run 51, Oct. 7th, rms- error is 0.08.

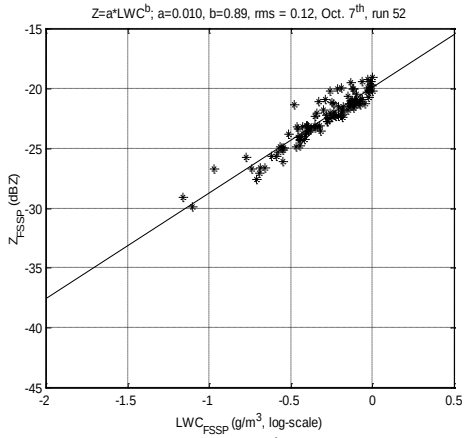

Fig. B.11: Run 52, Oct. 7th, rms- error is 0.12.

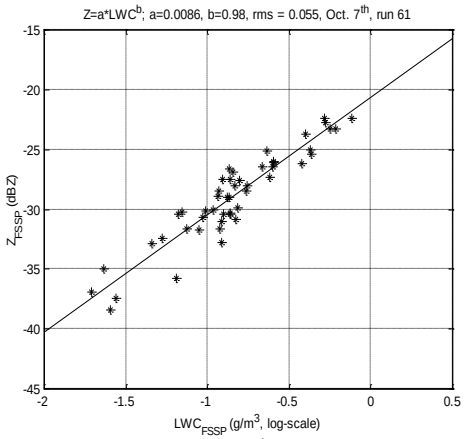

Fig. B.12: Run 61, Oct. 7th, rms- error is 0.05.

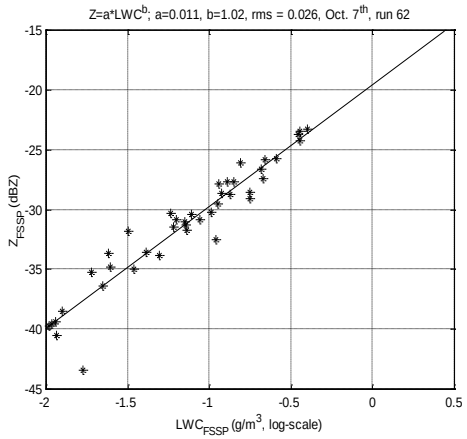

FigB.13: Run 62, Oct. 7th, rms- error is 0.03.

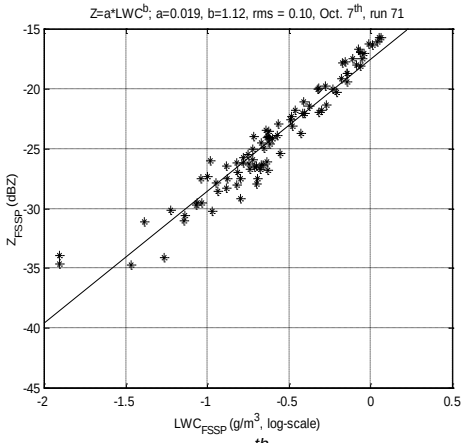

Fig. B.14: Run 71, Oct. 7th, rms- error is 0.10.

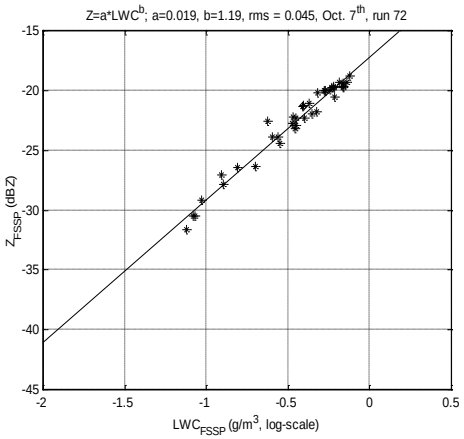

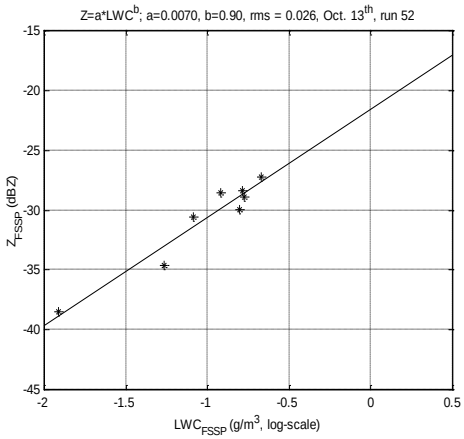

Fig. B.15: Run 72, Oct. 7th, rms- error is 0.05. *Fig. B.16: Run 52, Oct. 13th, rms- error is 0.03.*

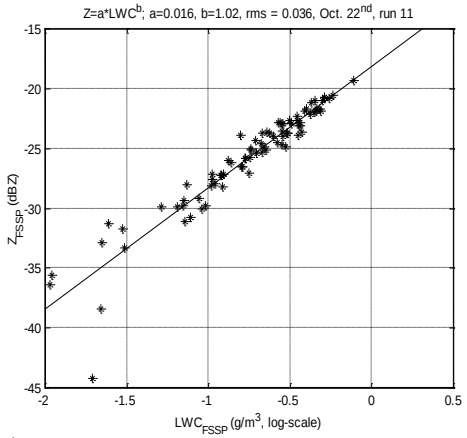

Fig. B.17: Run 11, Oct. 22nd, rms- error is 0.04.

Appendix C. Reflectivity, LWC and effective radius constant correction

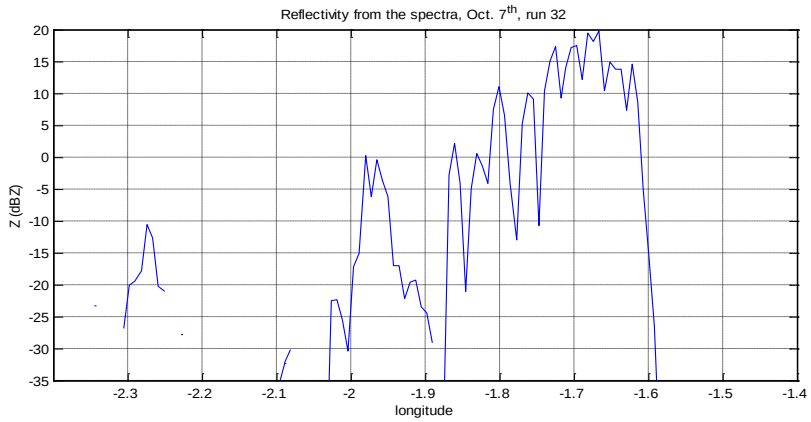

Figure C.1a: The reflectivity versus longitude for run 32, Oct. 7th.

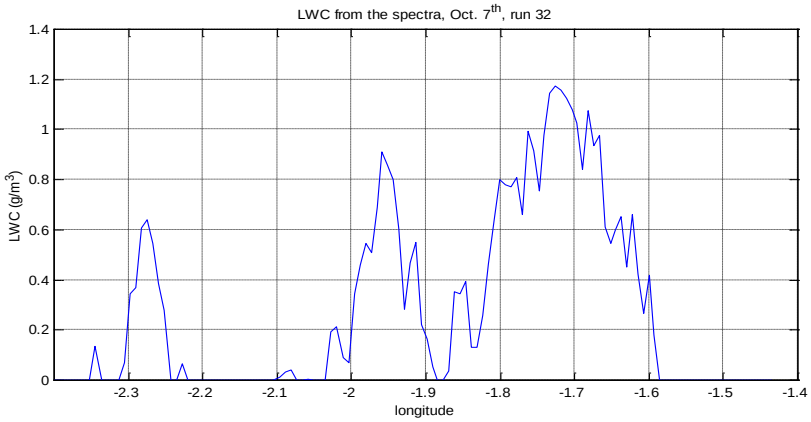

Figure C.1b: The LWC versus longitude for run 32, Oct. 7th.

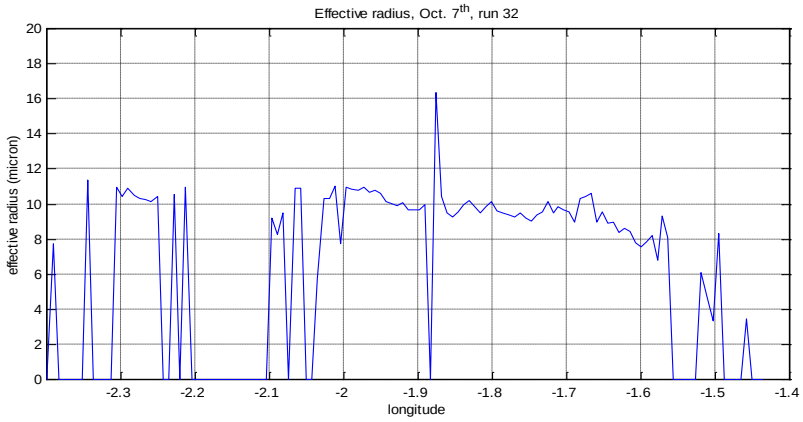

Figure C.1c: The effective radius versus longitude for run 32, Oct. 7th.

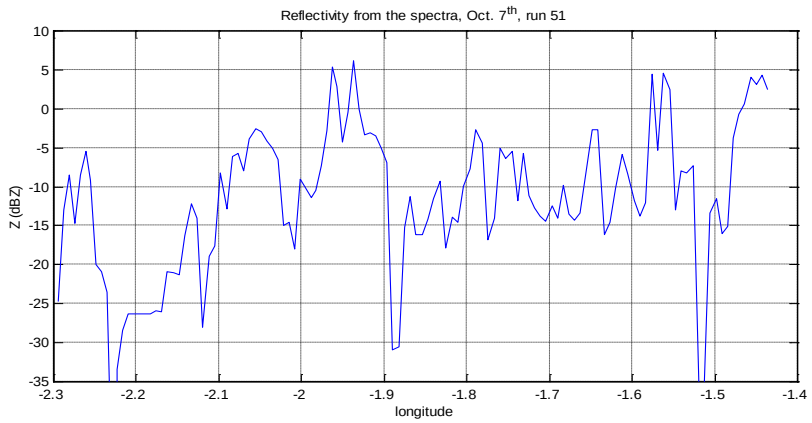

Figure C.2a: The reflectivity versus longitude for run 51, Oct. 7th.

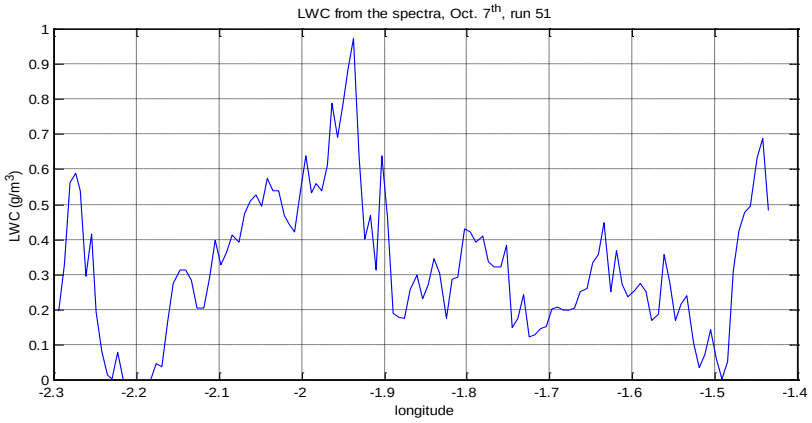

Figure C.2b: The LWC versus longitude for run 51, Oct. 7th.

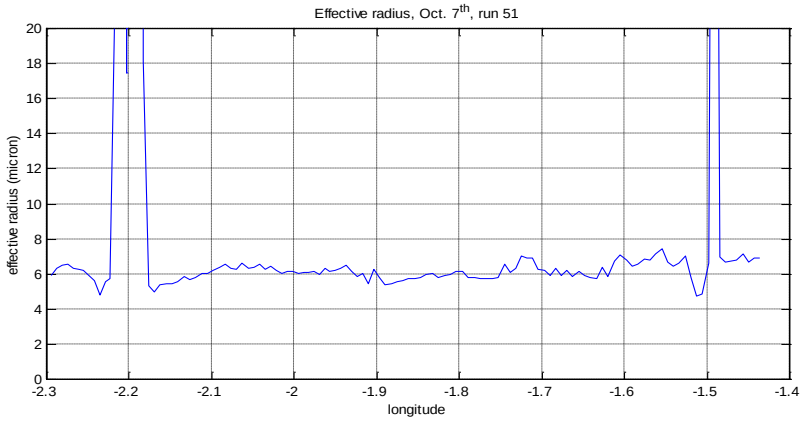

Figure C.2c: The effective radius versus longitude for run 51, Oct. 7th.

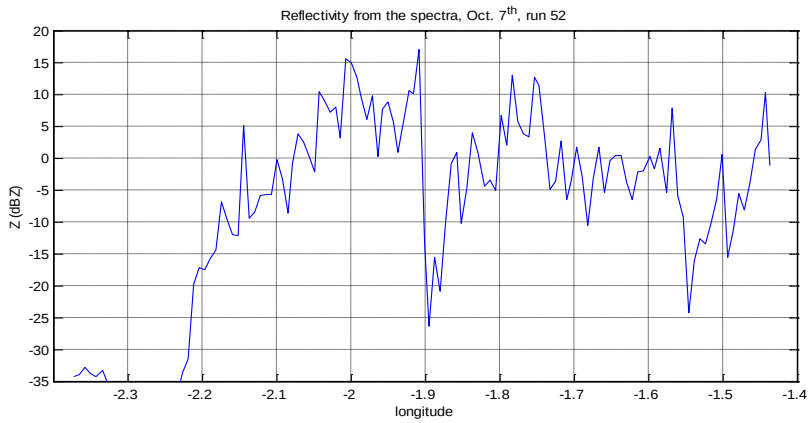

Figure C.3a: The reflectivity versus longitude for run 52, Oct. 7th.

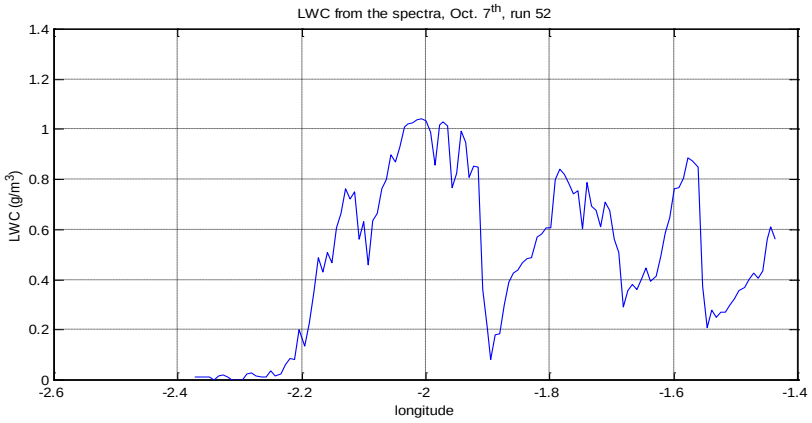

Figure C.3b: The LWC versus longitude for run 52, Oct. 7th.

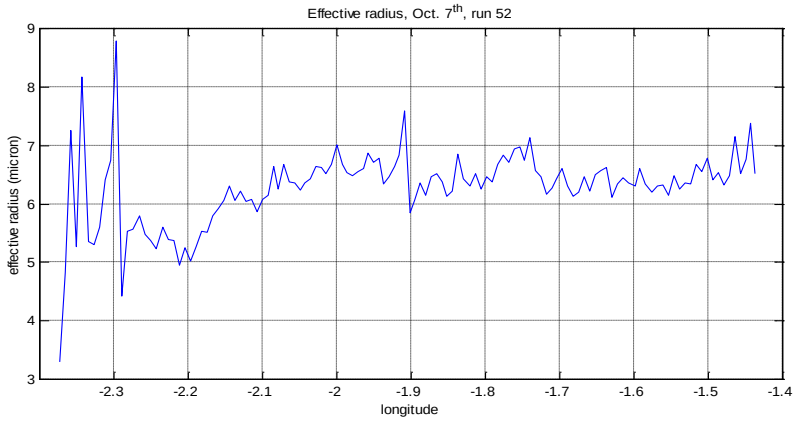

Figure C.3c: The effective radius versus longitude for run 52, Oct. 7th.

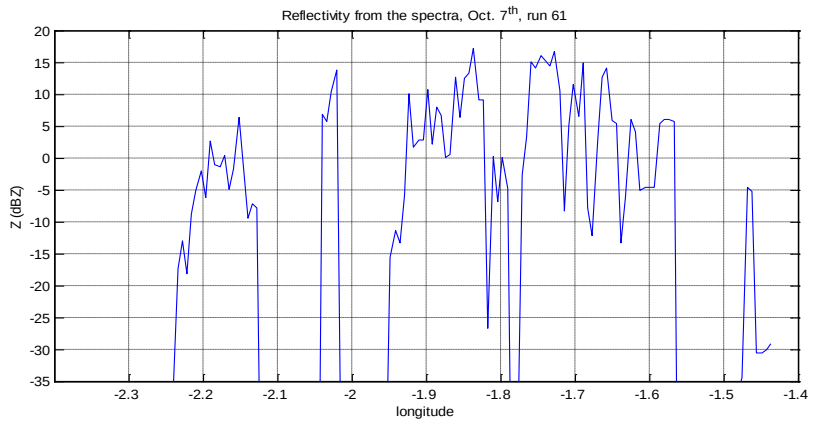

Figure C.4a: The reflectivity versus longitude for run 61, Oct. 7th.

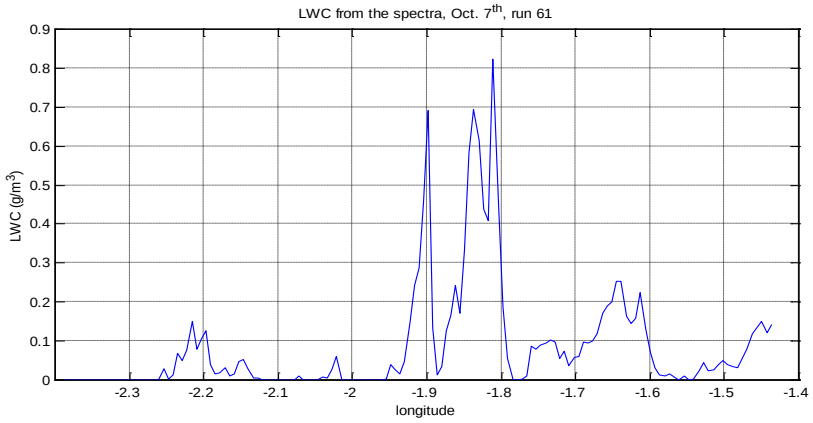

Figure C.4b: The LWC versus longitude for run 61, Oct. 7th.

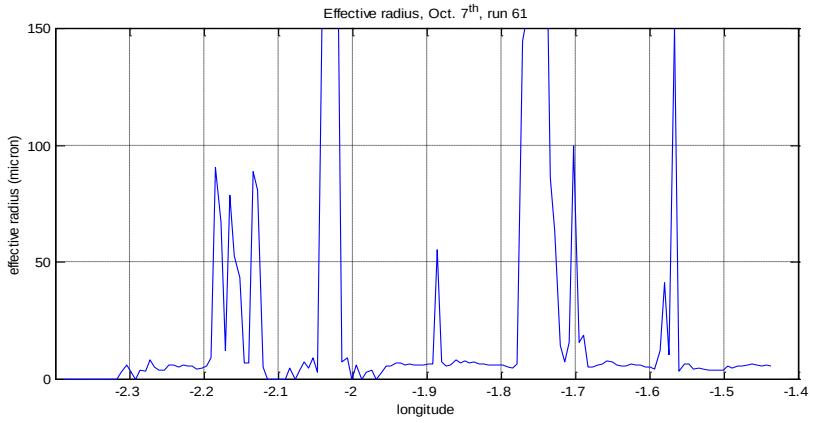

Figure C.4c: The effective radius versus longitude for run 61, Oct. 7th.

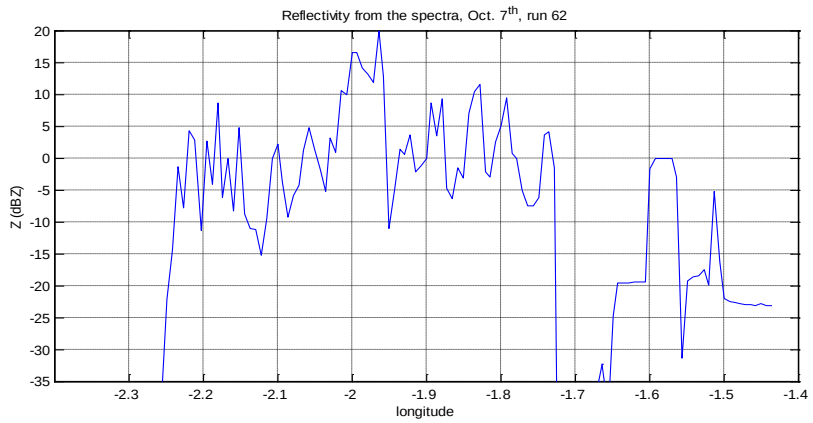

Figure C.5a: The reflectivity versus longitude for run 62, Oct. 7th.

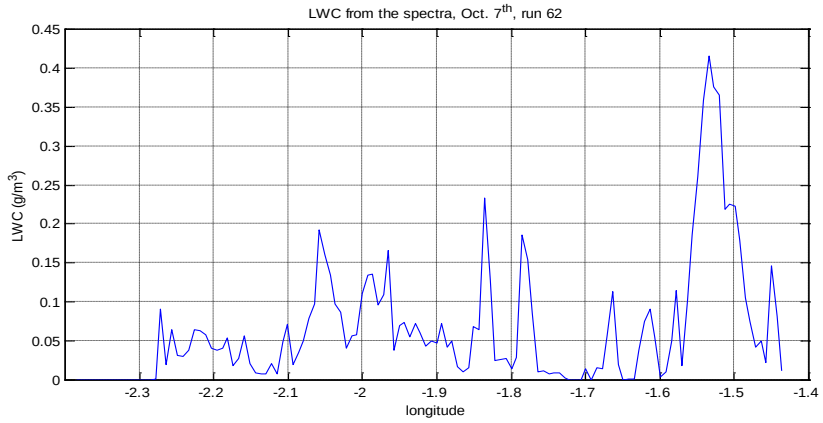

Figure C.5b: The LWC versus longitude for run 62, Oct. 7th.

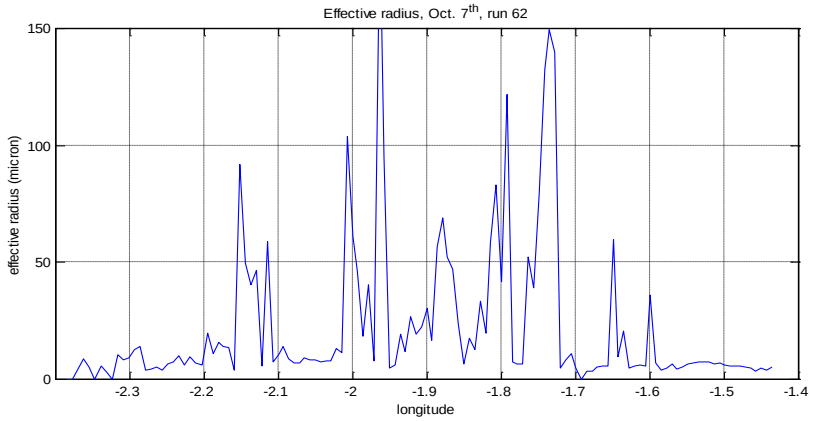

Figure C.5c: The effective radius versus longitude for run 62, Oct. 7th.

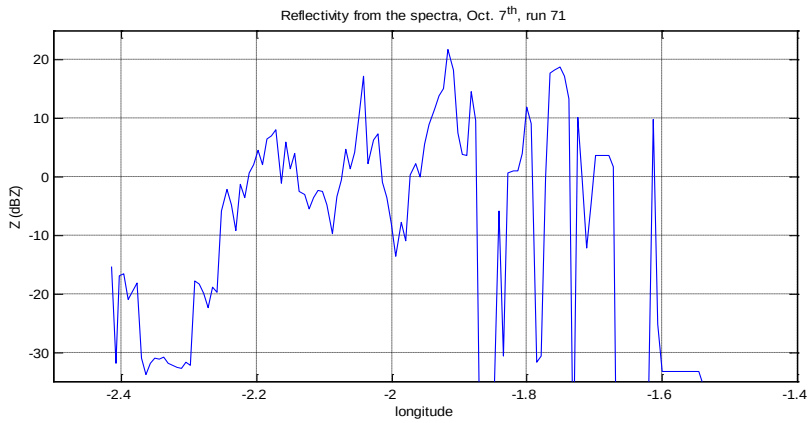

Figure C.6a: The reflectivity versus longitude for run 71, Oct. 7th.

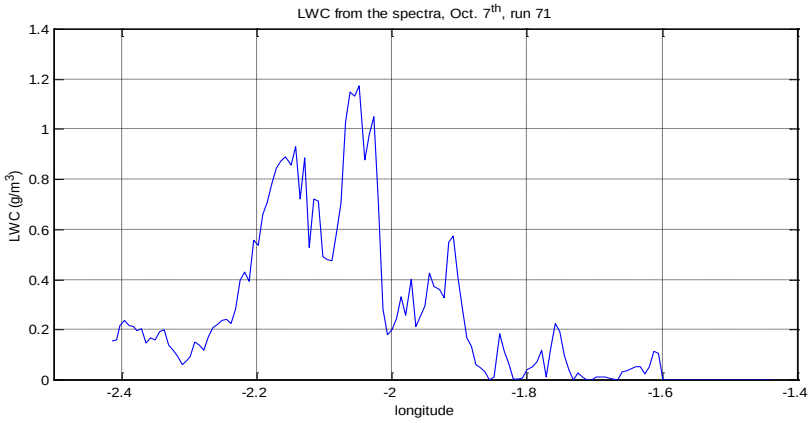

Figure C.6b: The LWC versus longitude for run 71, Oct. 7th.

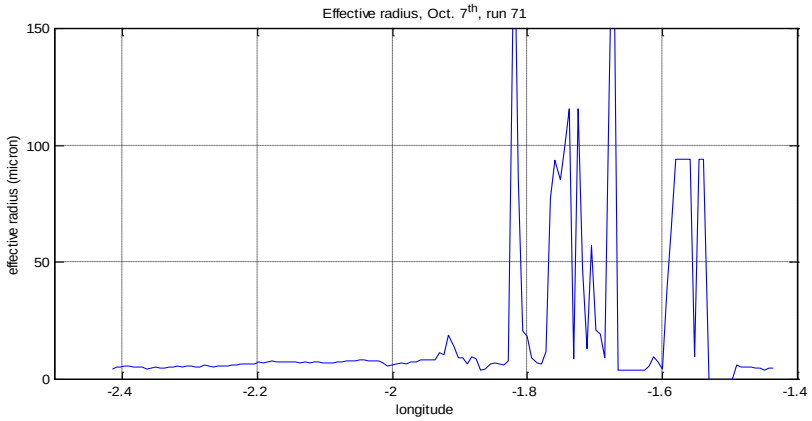

Figure C.6c: The effective radius versus longitude for run 71, Oct. 7th.

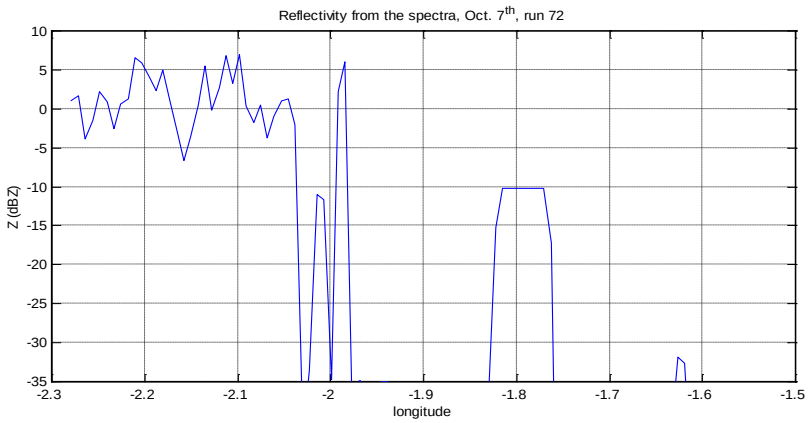

Figure C.7a: The reflectivity versus longitude for run 72, Oct. 7th.

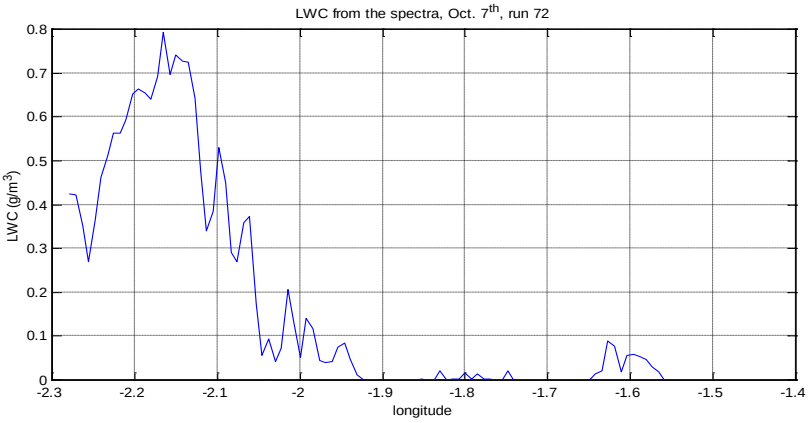

Figure C.7b: The LWC versus longitude for run 72, Oct. 7th.

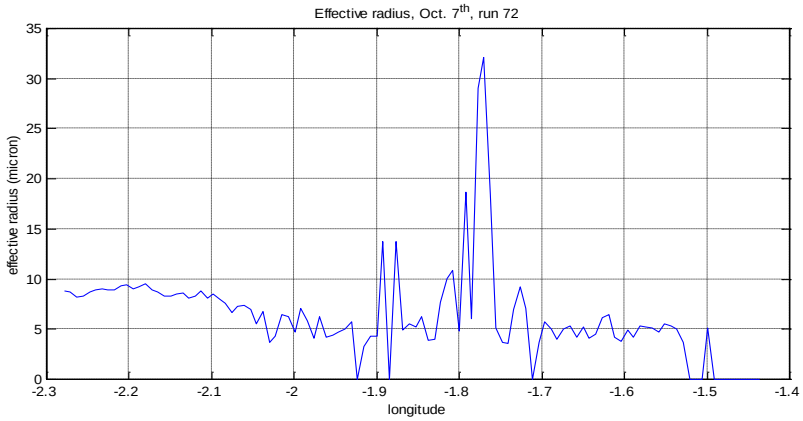

Figure C.7c: The effective radius versus longitude for run 72, Oct. 7th.

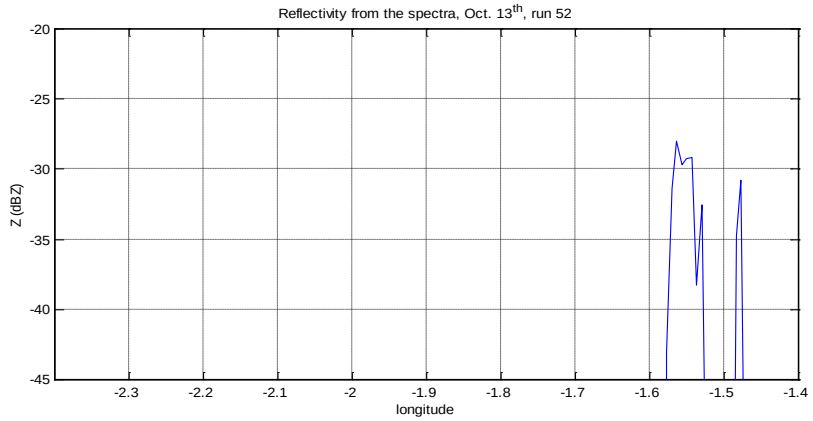

Figure C.8a: The reflectivity versus longitude for run 52, Oct. 13th.

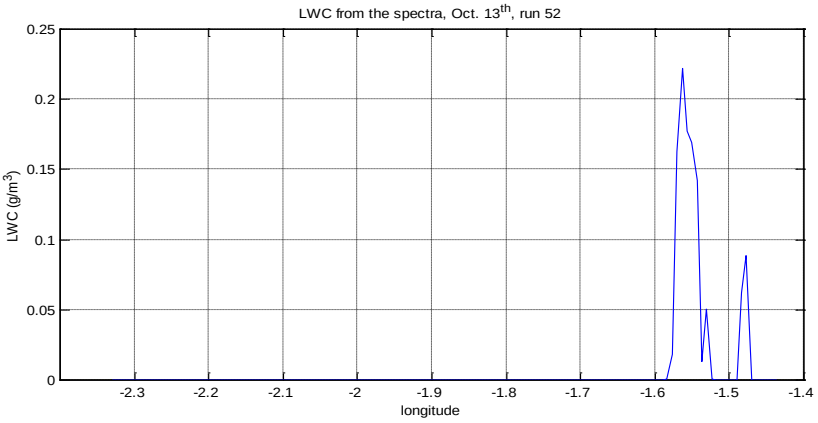

Figure C.8b: The LWC versus longitude for run 52, Oct. 13th.

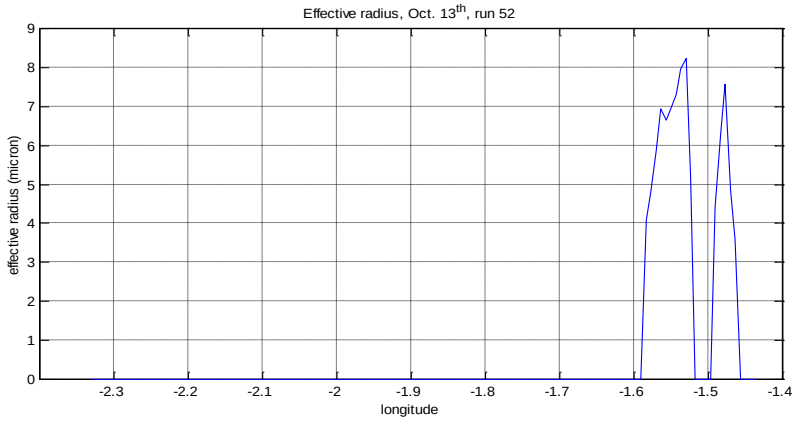

Figure C.8c: The effective radius versus longitude for run 52, Oct. 13th.

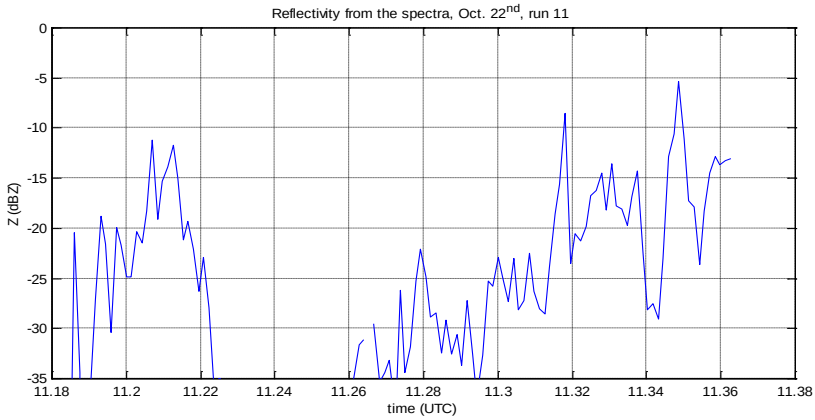

Figure C.9a: The reflectivity versus longitude for run 11, Oct. 22nd.

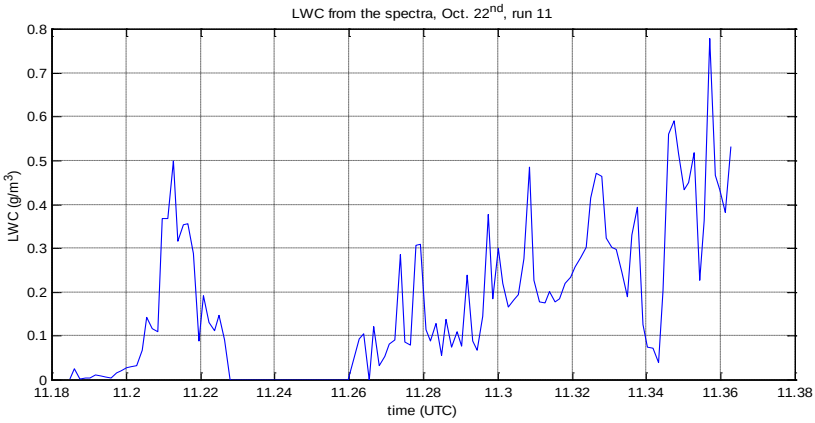

Figure C.9b: The LWC versus longitude for run 11, Oct. 22nd.

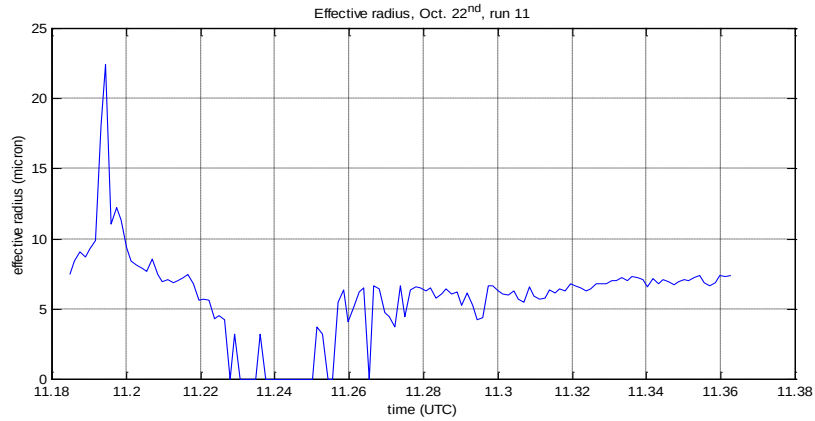

Figure C.9c: The effective radius versus longitude for run 11, Oct. 22nd.

Appendix D. Reflectivity, LWC and effective radius size dependent correction

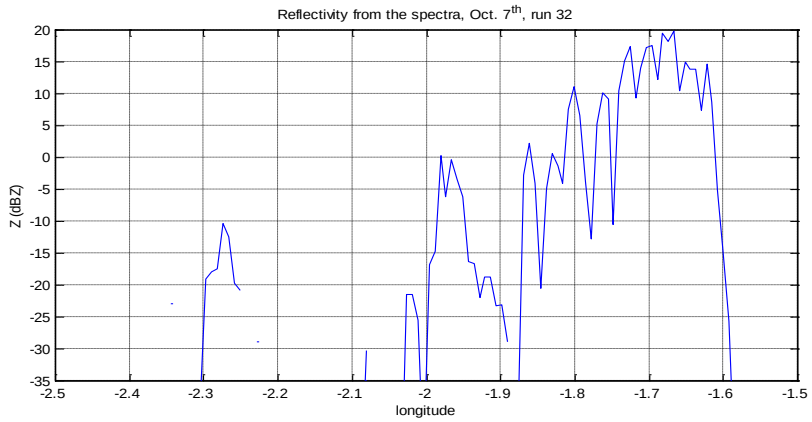

Figure D.1a: The reflectivity versus longitude for run 32, Oct. 7th.

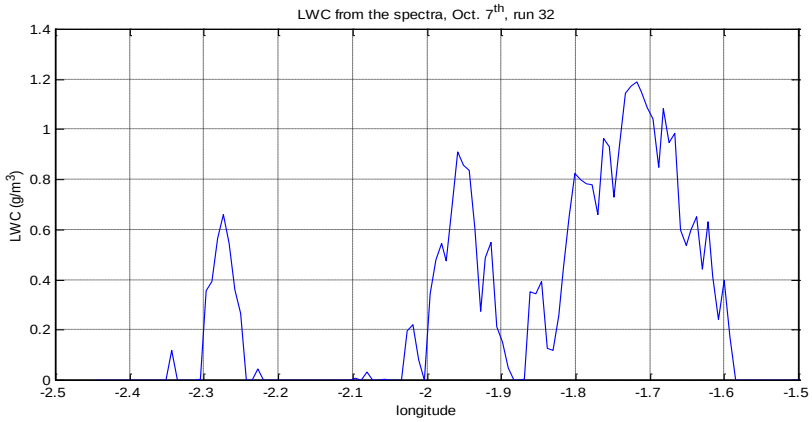

Figure D.1b: The LWC versus longitude for run 32, Oct. 7th.

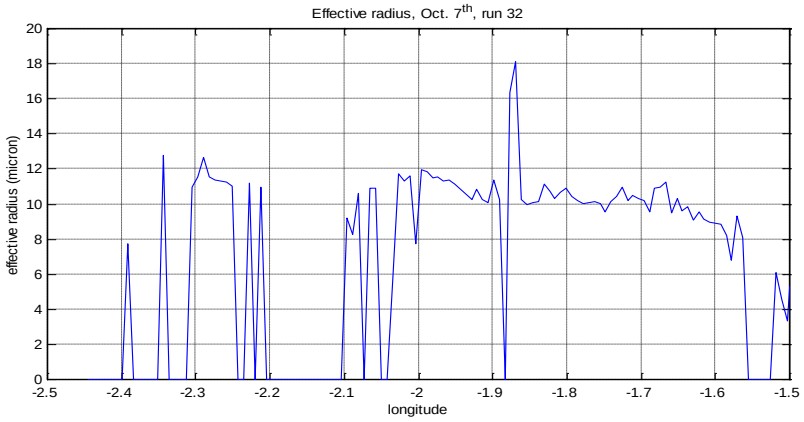

Figure D.1c: The effective radius versus longitude for run 32, Oct. 7th.

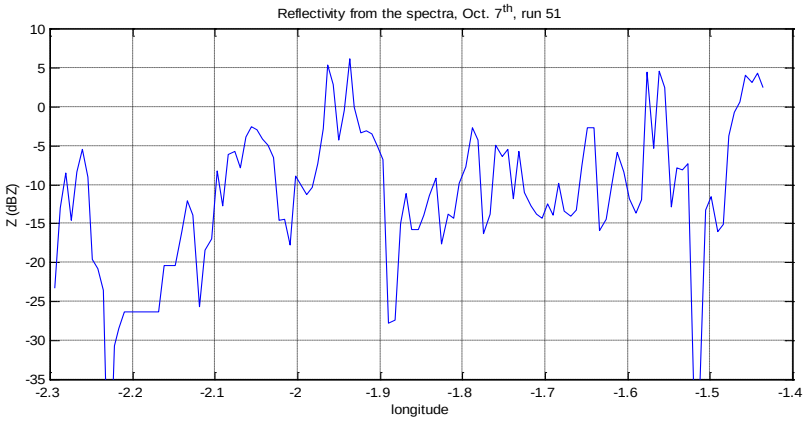

Figure D.2a: The reflectivity versus longitude for run 51, Oct. 7th.

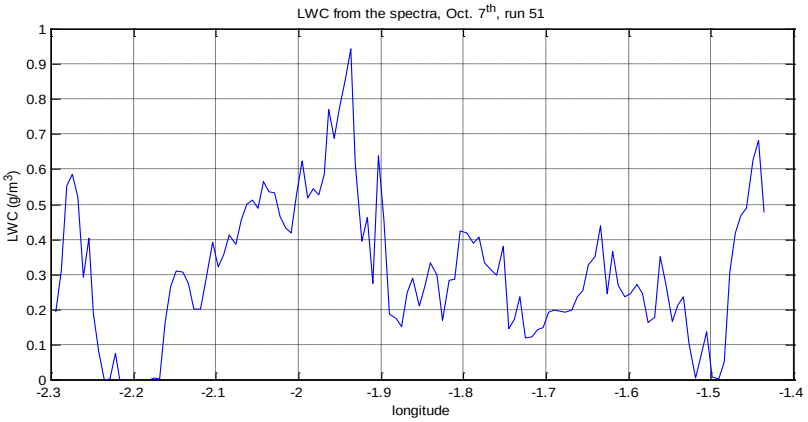

Figure D.2b: The LWC versus longitude for run 51, Oct. 7th.

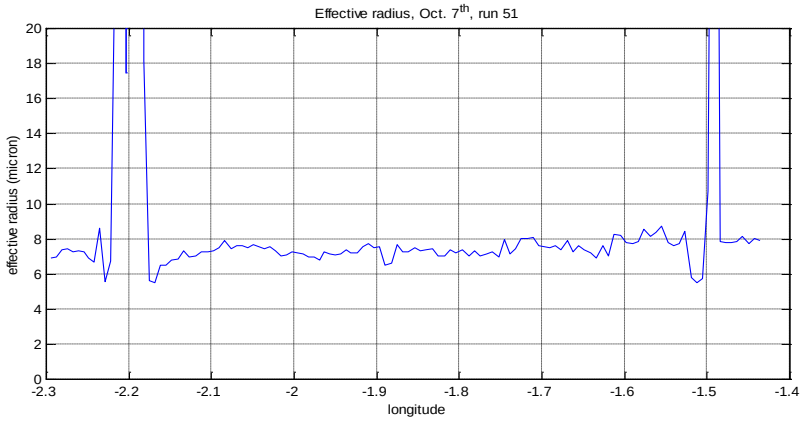

Figure D.2c: The effective radius versus longitude for run 51, Oct. 7th.

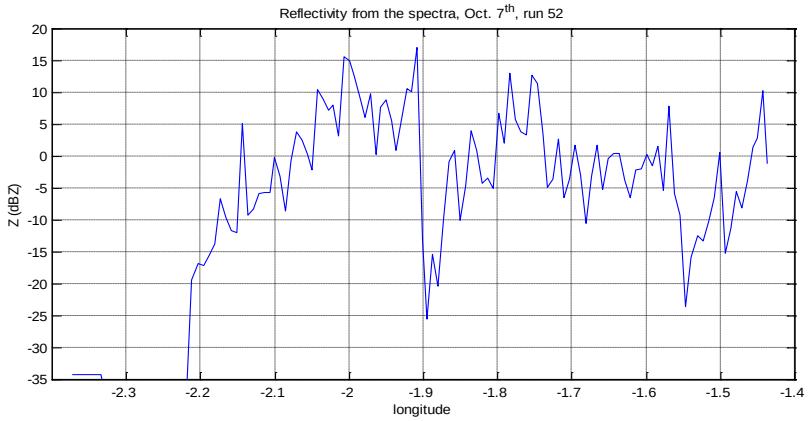

Figure D.3a: The reflectivity versus longitude for run 52, Oct. 7th.

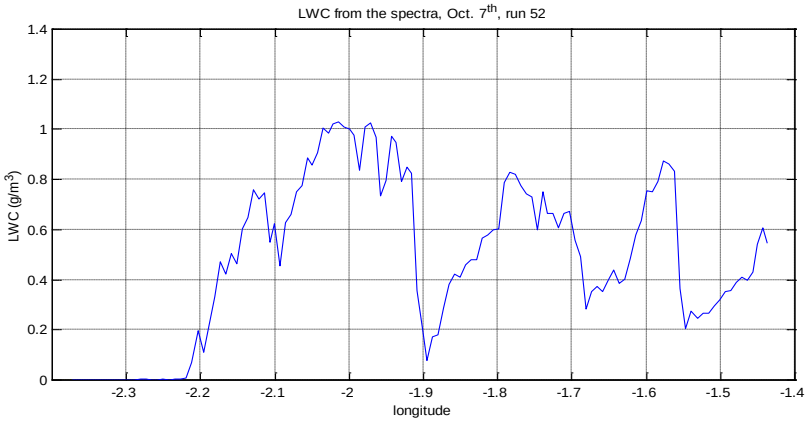

Figure D.3b: The LWC versus longitude for run 52, Oct. 7th.

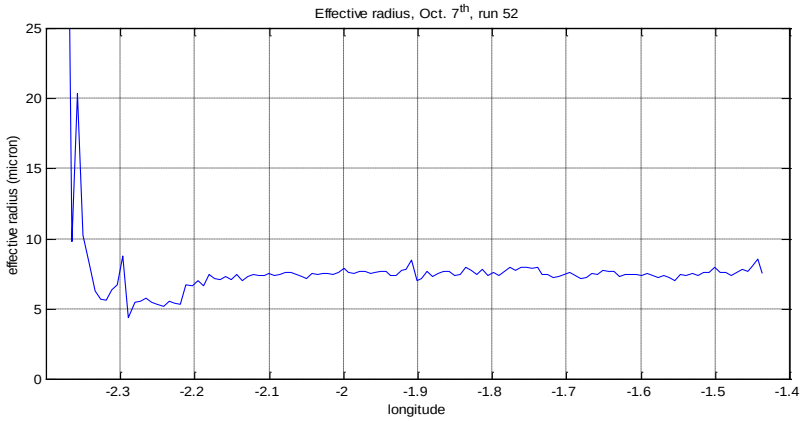

Figure D.3c: The effective radius versus longitude for run 52, Oct. 7th.

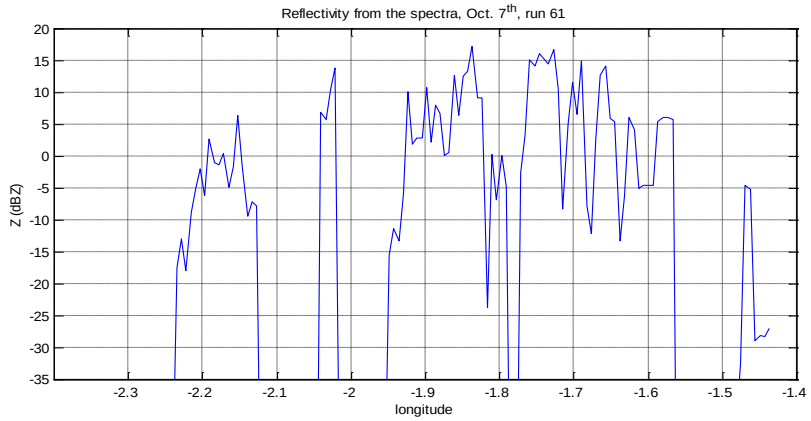

Figure D.4a: The reflectivity versus longitude for run 61, Oct. 7th.

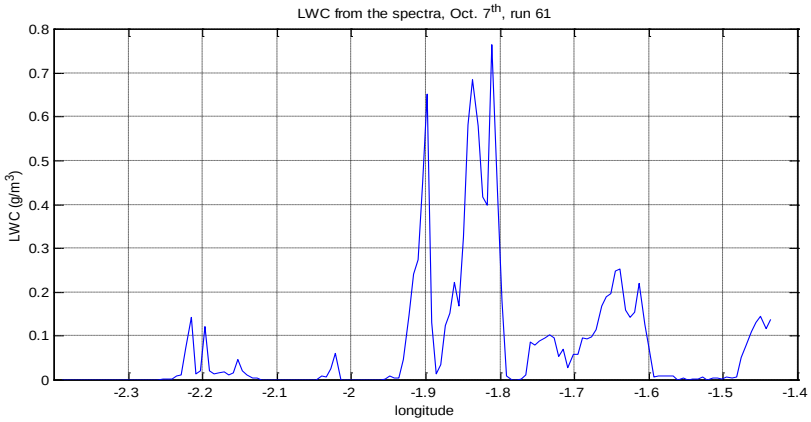

Figure D.4b: The LWC versus longitude for run 61, Oct. 7th.

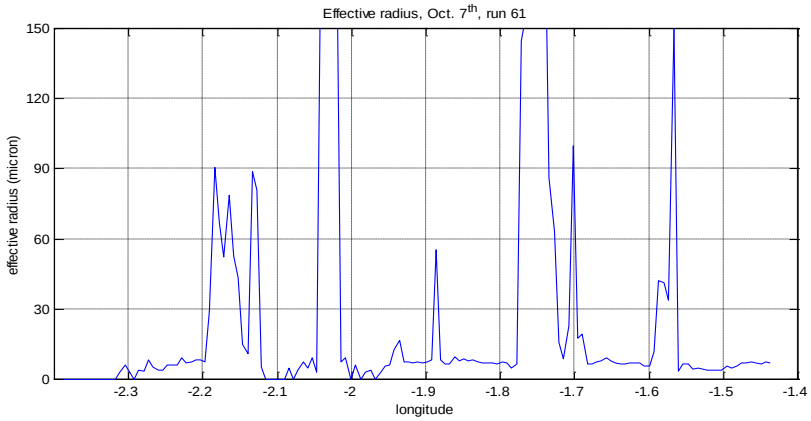

Figure D.4c: The effective radius versus longitude for run 61, Oct. 7th.

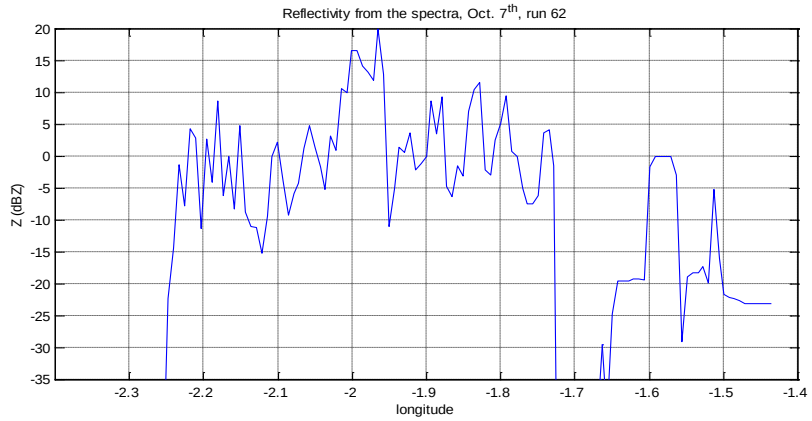

Figure D.5a: The reflectivity versus longitude for run 62, Oct. 7th.

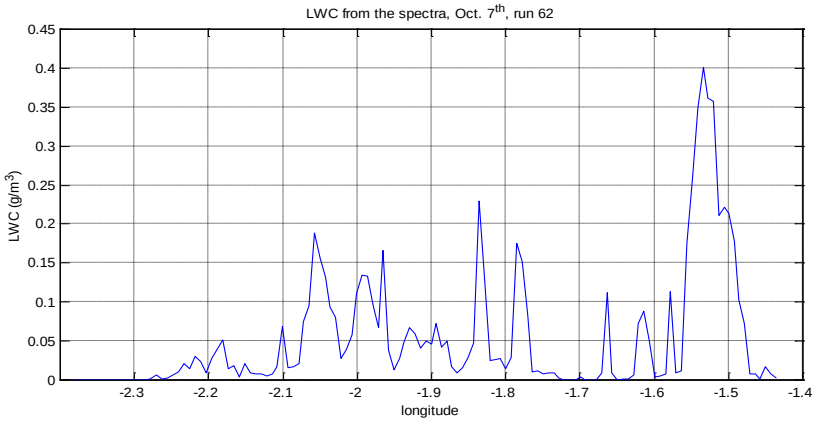

Figure D.5b: The LWC versus longitude for run 62, Oct. 7th.

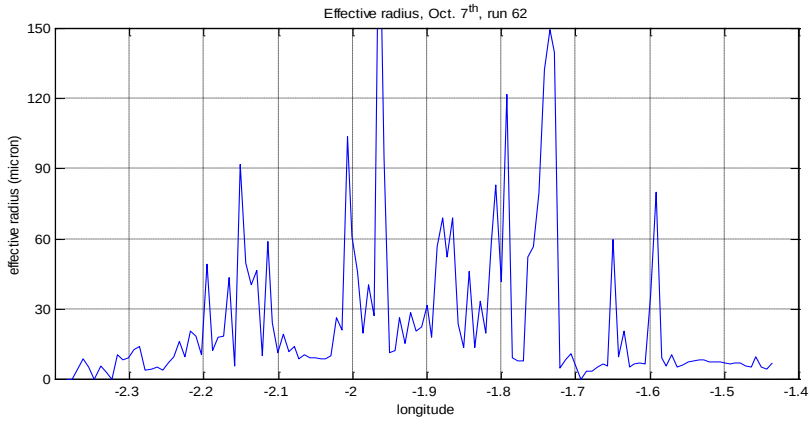

Figure D.5c: The effective radius versus longitude for run 62, Oct. 7th.

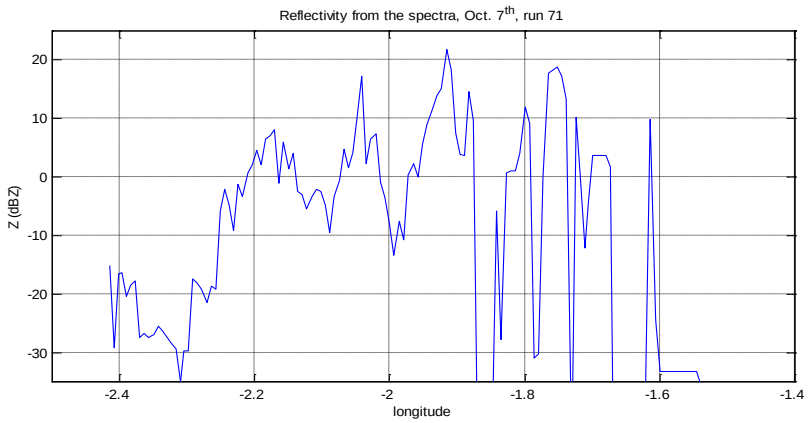

Figure D.6a: The reflectivity versus longitude for run 71, Oct. 7th.

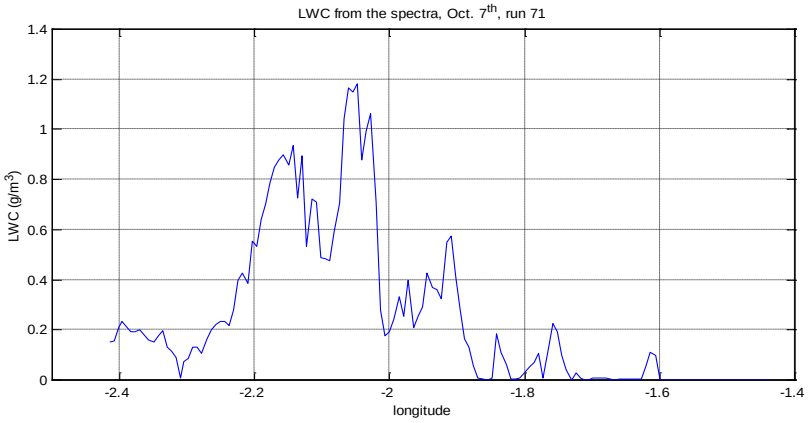

Figure D.6b: The LWC versus longitude for run 71, Oct. 7th.

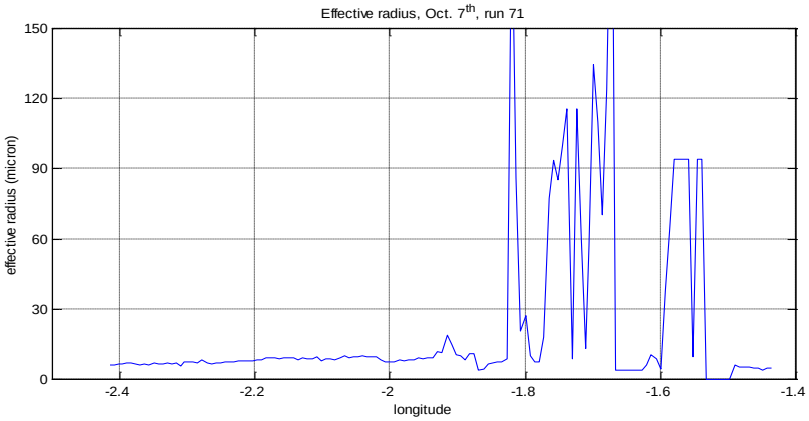

Figure D.6c: The effective radius versus longitude for run 71, Oct. 7th.

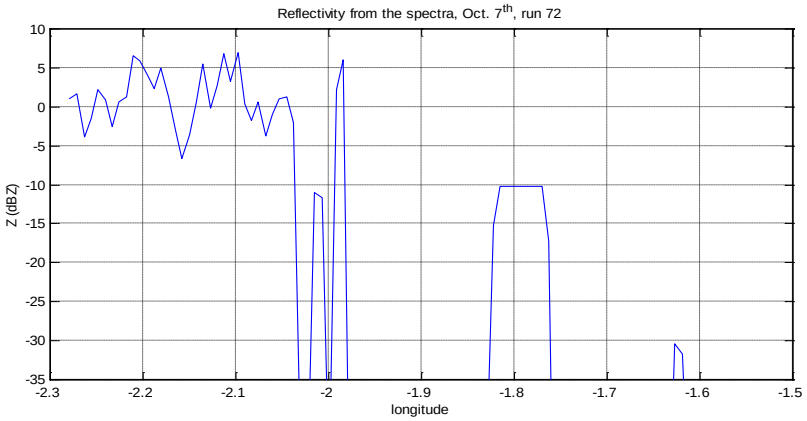

Figure D.7a: The reflectivity versus longitude for run 72, Oct. 7th.

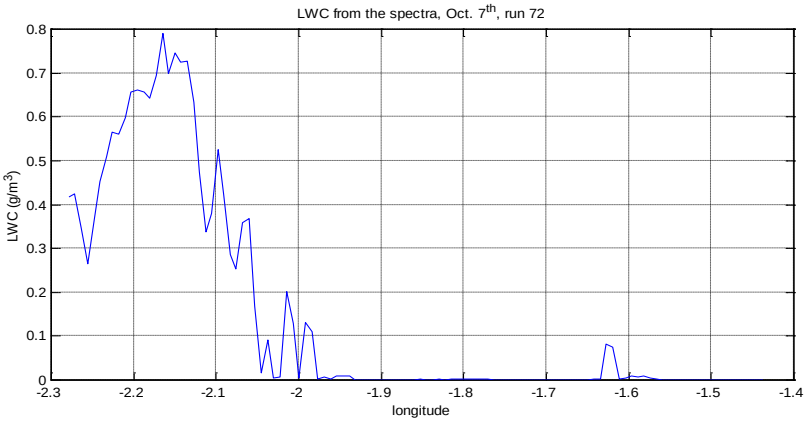

Figure D.7b: The LWC versus longitude for run 72, Oct. 7th.

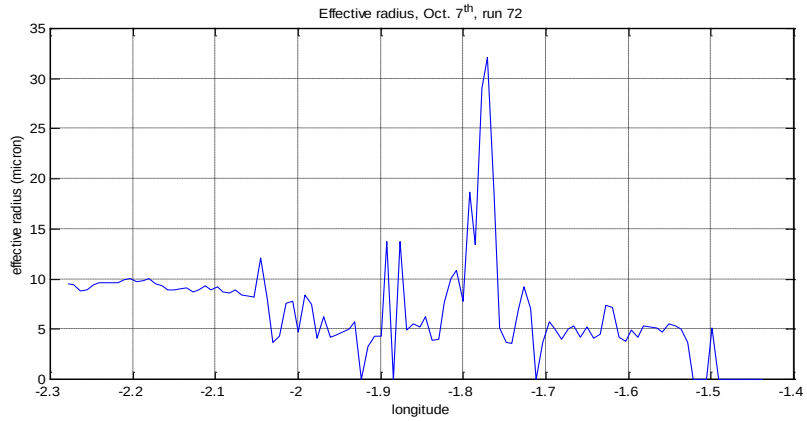

Figure D.7c: The effective radius versus longitude for run 72, Oct. 7th.

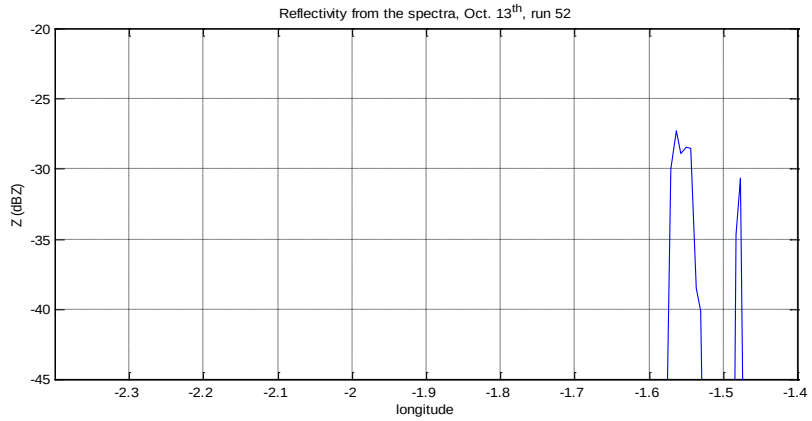

Figure D.8a: The reflectivity versus longitude for run 52, Oct. 13th.

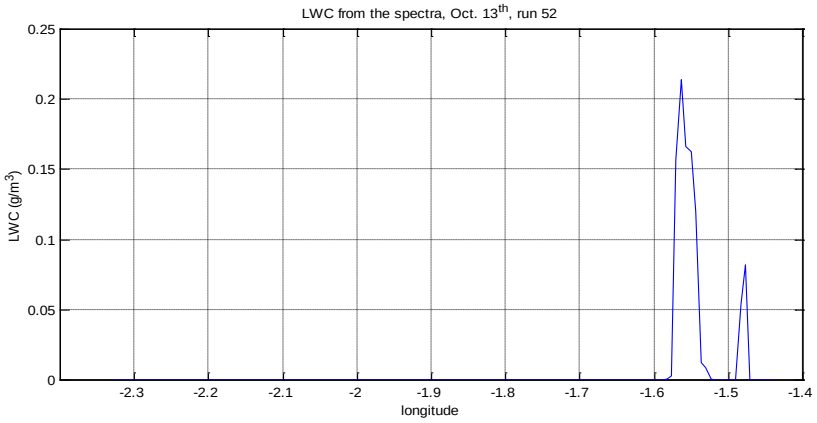

Figure D.8b: The LWC versus longitude for run 52, Oct. 13th.

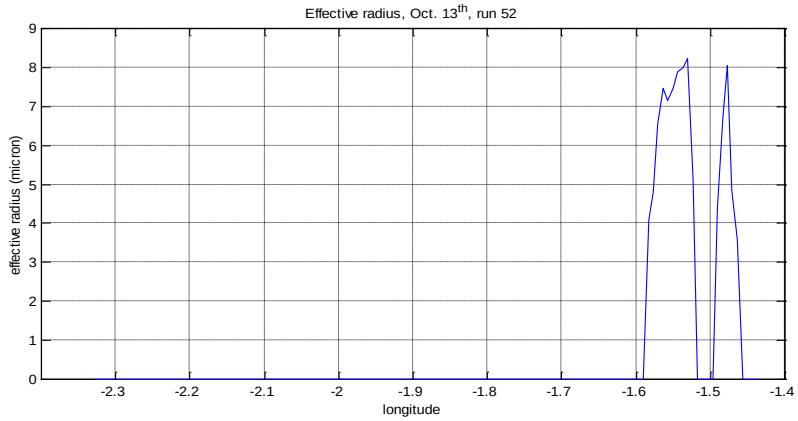

Figure D.8c: The effective radius versus longitude for run 52, Oct. 13th.

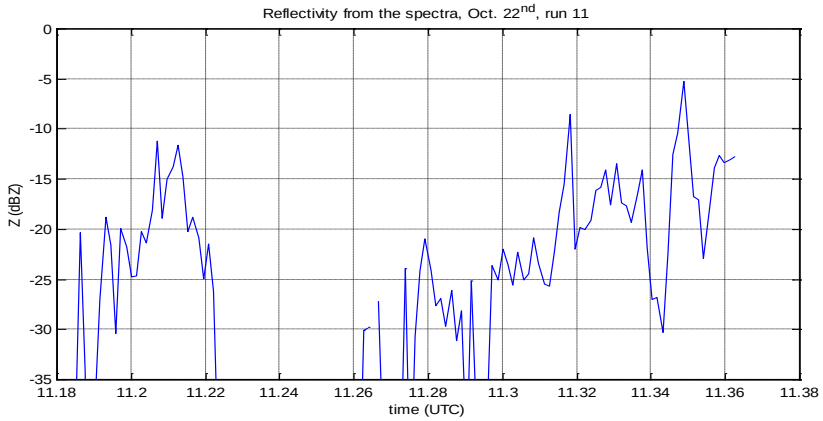

Figure D.9a: The reflectivity versus longitude for run 11, Oct. 22nd.

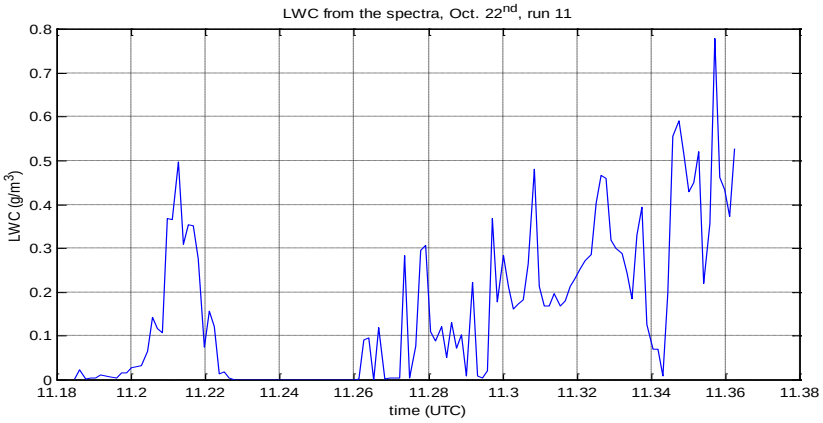

Figure D.9b: The LWC versus longitude for run 11, Oct. 22nd.

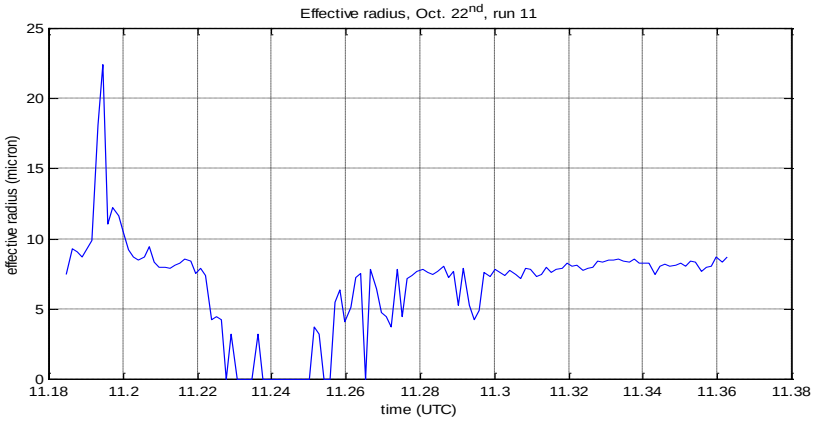

Figure D.9c: The effective radius versus longitude for run 11, Oct. 22nd.

Appendix E. Comparison of radar images and the effective radius

In this appendix radar measurements and the effective radius from the spectra are presented. The 94 GHz Kestrel radar was mounted on the Arat and the particle probes on the Hercules aircraft. The aircraft have comparable but slightly different speeds. Thus they were not at the same longitude simultaneously. However they did arrive overhead Chilbolton (-1.44° longitude) at the same time.
On October 22nd the Arat was not operational so there are no images from the Kestrel for that day. For run 32 of October 7th there is also no image from the Kestrel available. The image shown in this appendix is made about five minutes after run 32. It is included to give a global impression of the conditions during run 32.

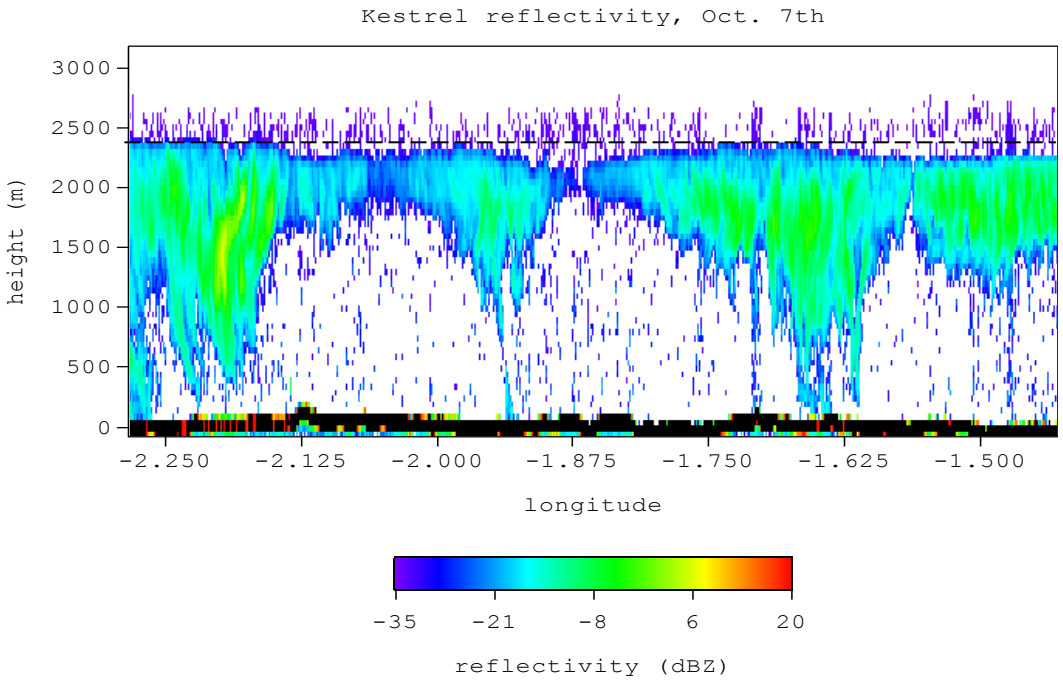

Figure E.1: The reflectivity measured by the Kestrel. The image shows the situation just after run 32, Oct. 7th. The dashed line shows the track of the Hercules aircraft. The image is made five to ten minutes after the passage of the Hercules.

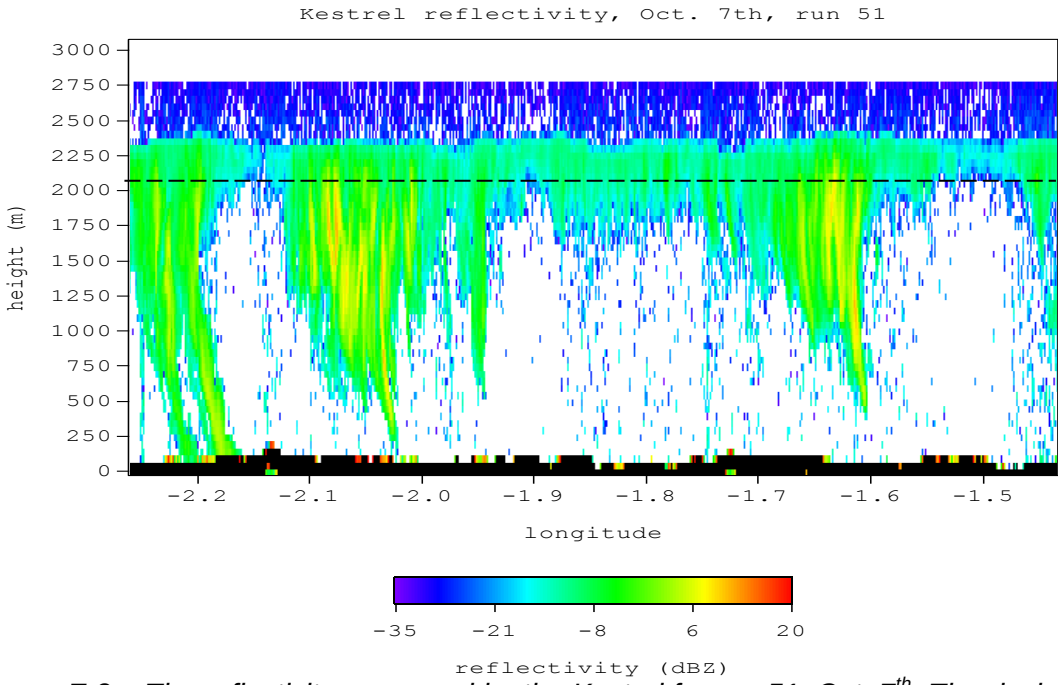

Figure E.2a: The reflectivity measured by the Kestrel for run 51, Oct. 7th. The dashed line shows the track of the Hercules.

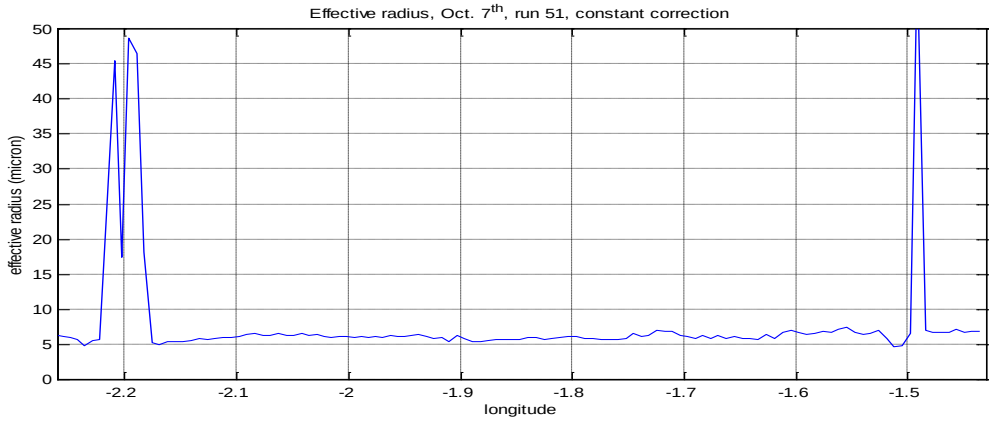

Figure E.2b: The effective radius using the constant correction for run 51, Oct. 7th.

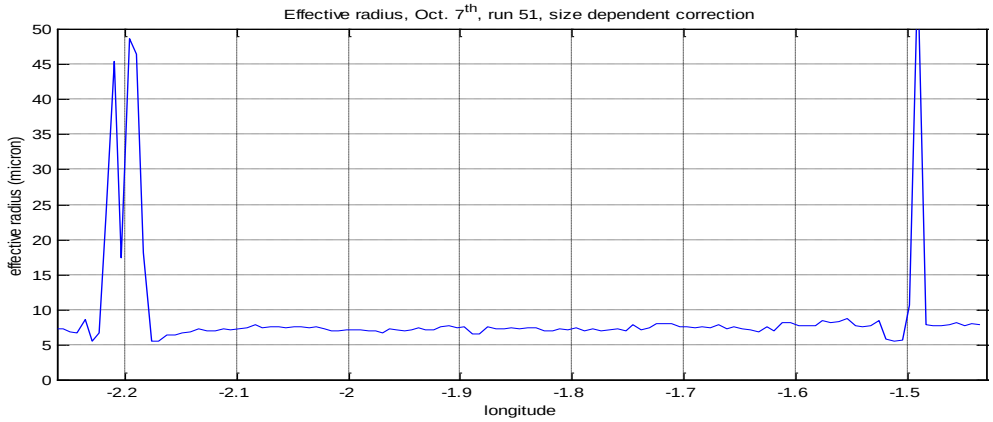

Figure E.2c: The effective radius using the size dependent correction for run 51, Oct. 7th.

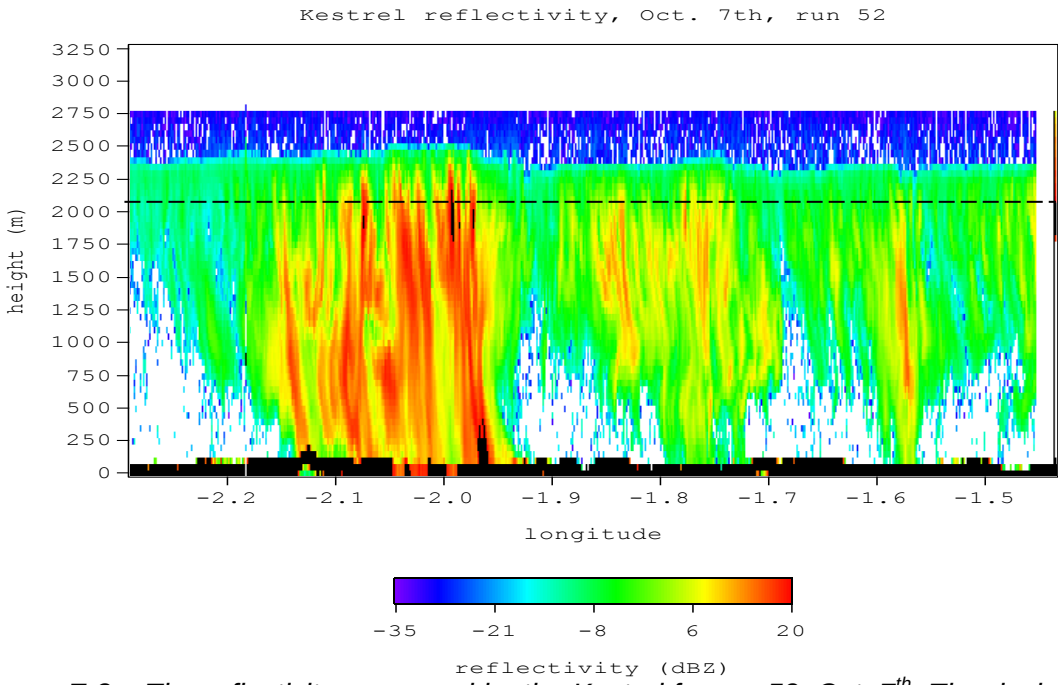

Figure E.3a: The reflectivity measured by the Kestrel for run 52, Oct. 7th. The dashed line shows the track of the Hercules.

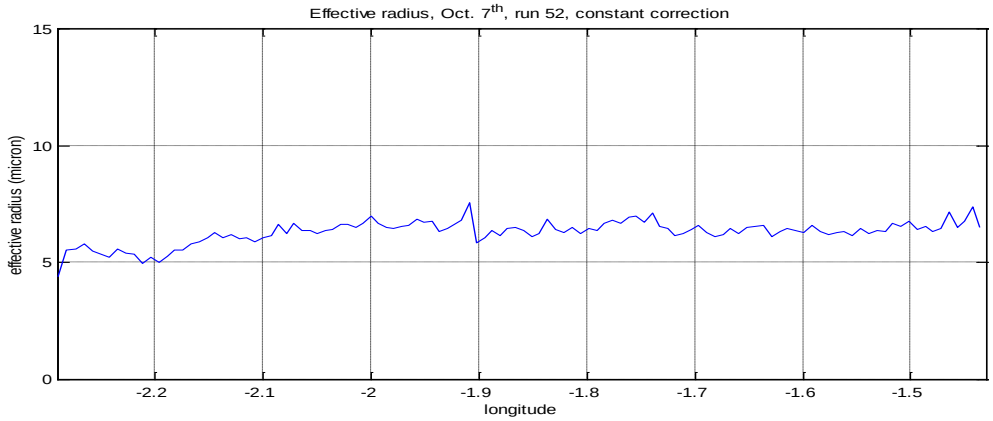

Figure E.3b: The effective radius using the constant correction for run 52, Oct. 7th.

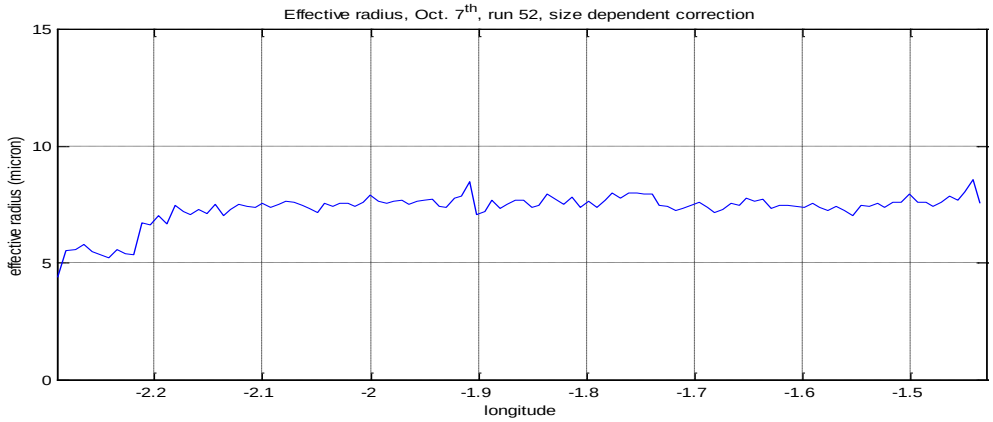

Figure E.3c: The effective radius using the size dependent correction for run 52, Oct. 7th.

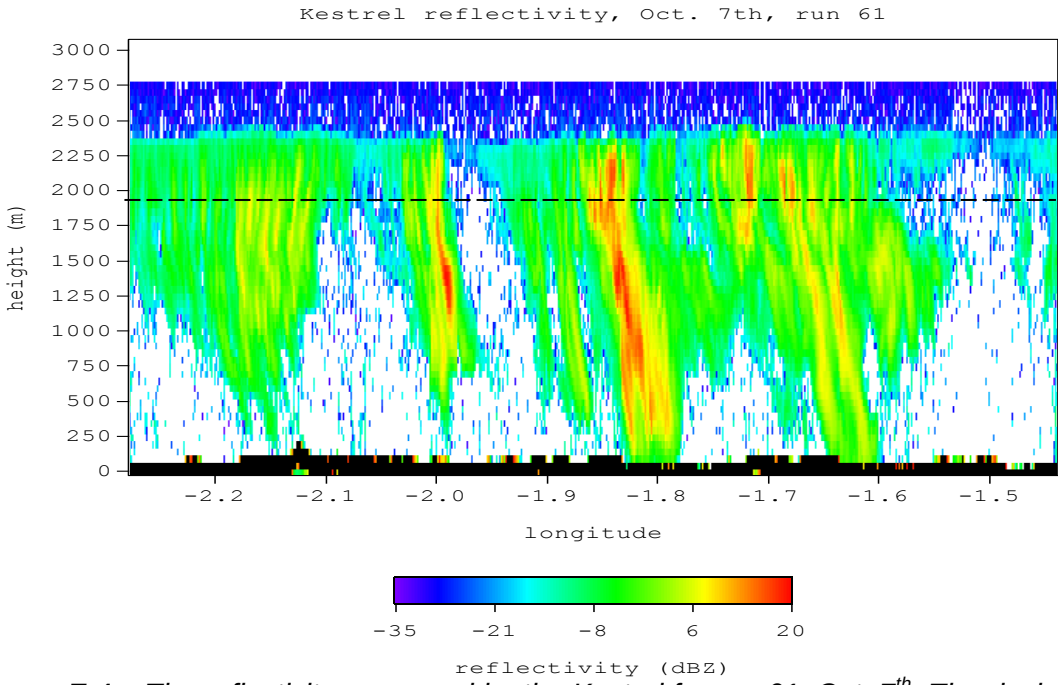

Figure E.4a: The reflectivity measured by the Kestrel for run 61, Oct. 7th. The dashed line shows the track of the Hercules.

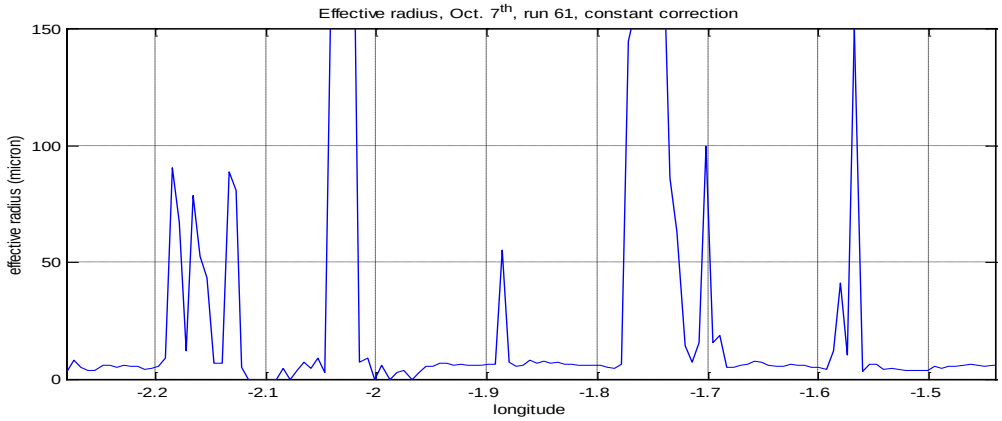

Figure E.4b: The effective radius using the constant correction for run 61, Oct. 7th.

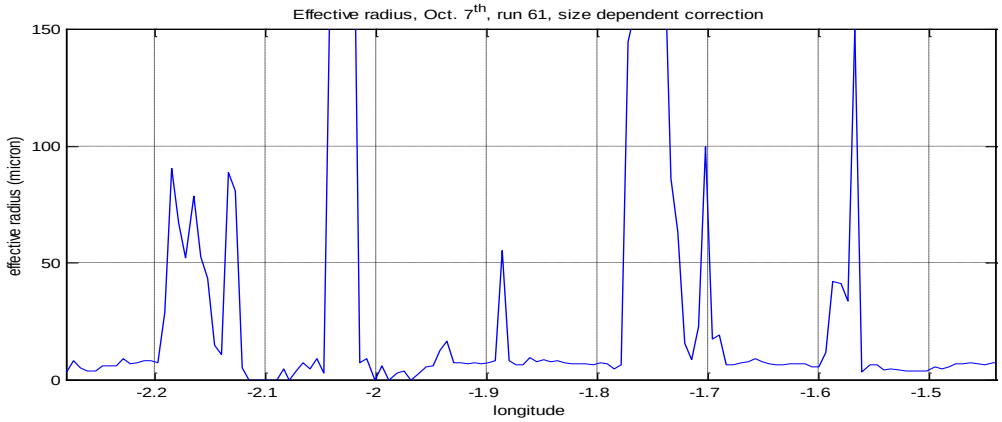

Figure E.4c: The effective radius using the size dependent correction for run 61, Oct. 7th.

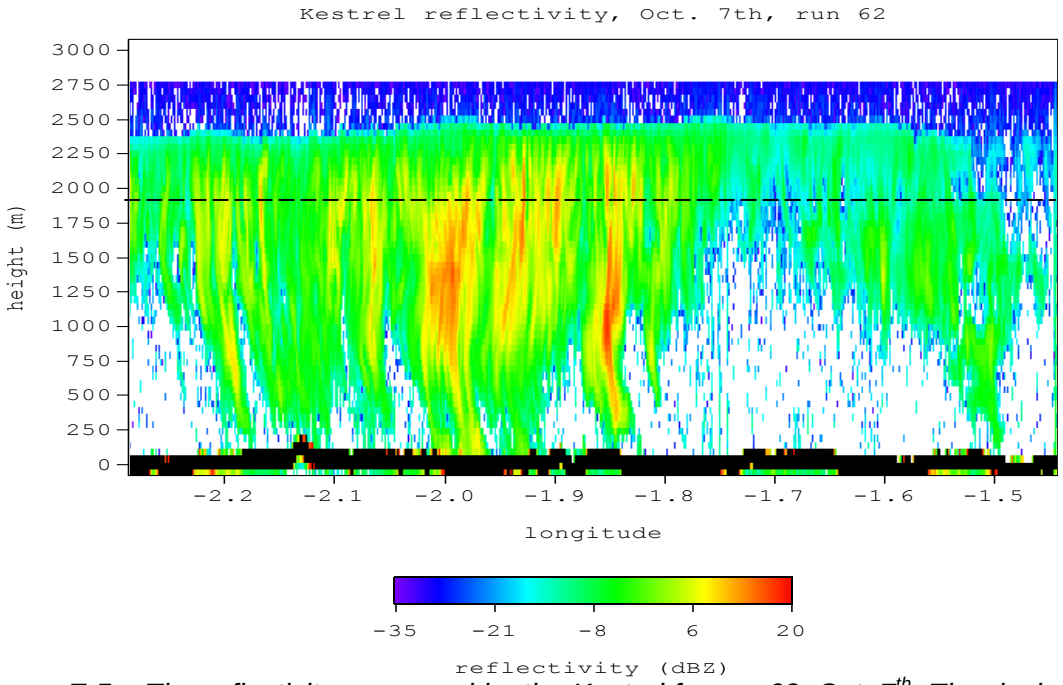

Figure E.5a: The reflectivity measured by the Kestrel for run 62, Oct. 7th. The dashed line shows the track of the Hercules.

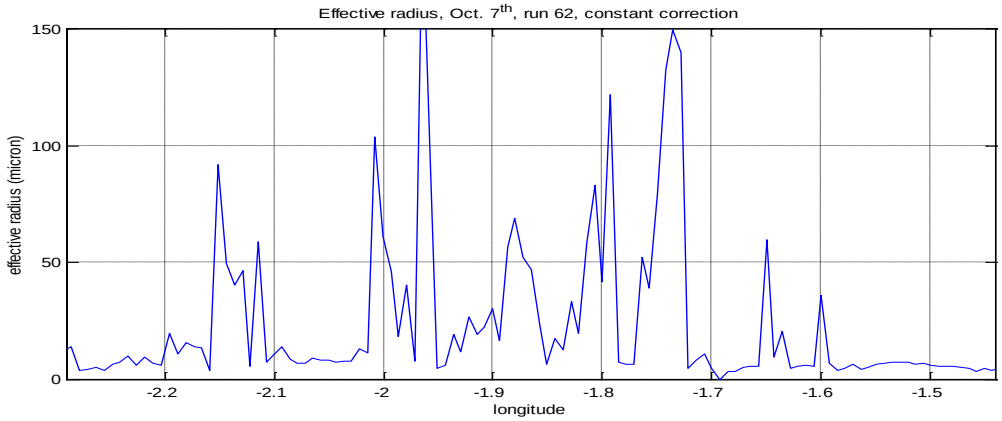

Figure E.5b: The effective radius using the constant correction for run 62, Oct. 7th.

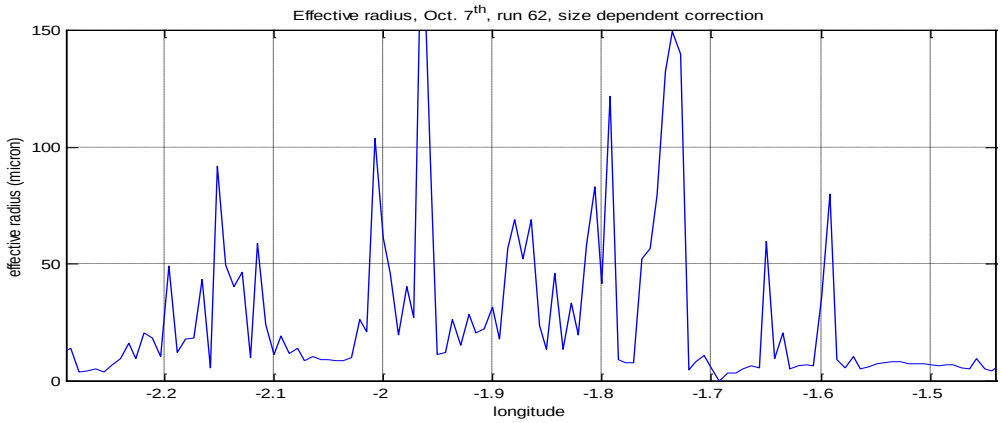

Figure E.5c: The effective radius using the size dependent correction for run 62, Oct. 7th.

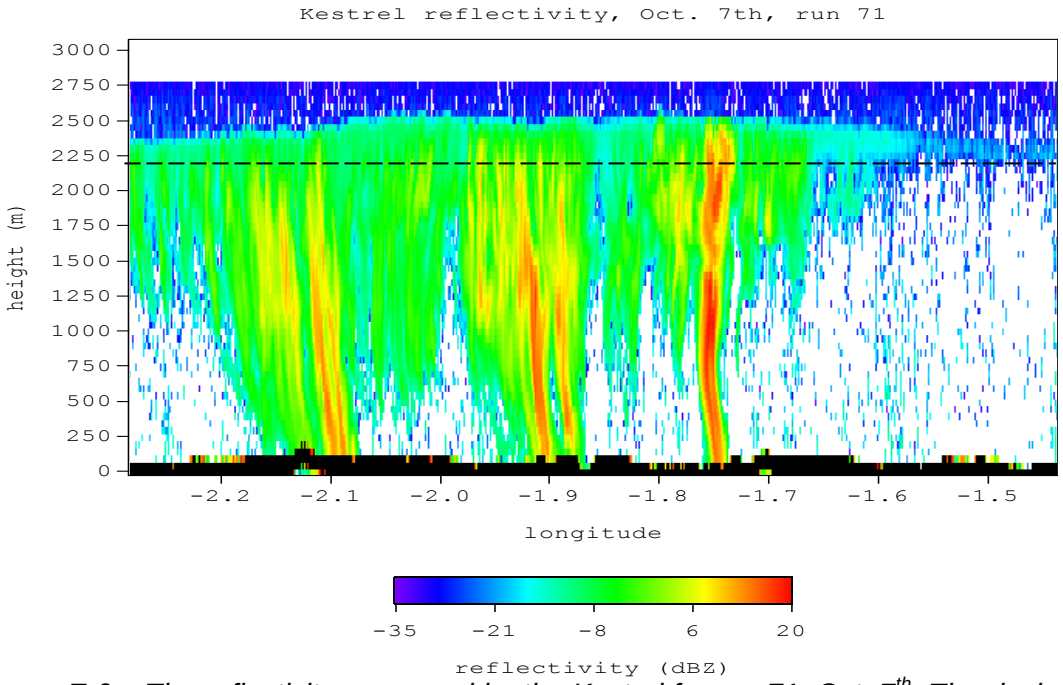

Figure E.6a: The reflectivity measured by the Kestrel for run 71, Oct. 7th. The dashed line shows the track of the Hercules.

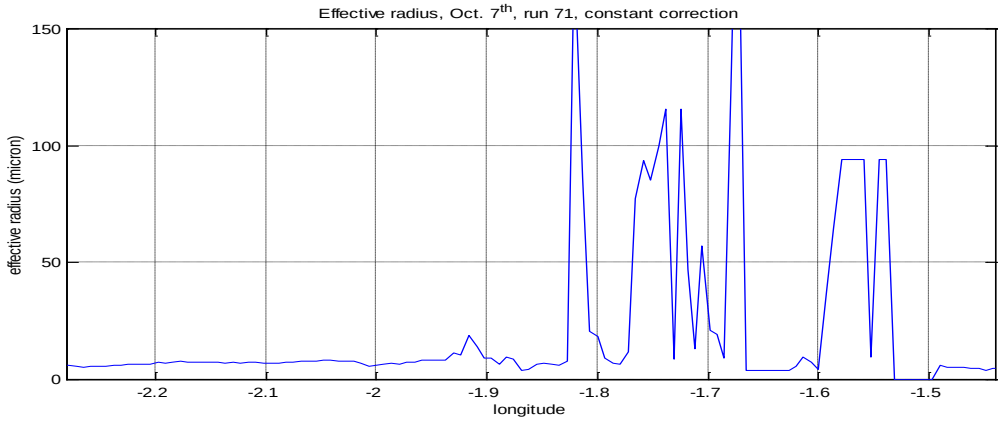

Figure E.6b: The effective radius using the constant correction for run 71, Oct. 7th.

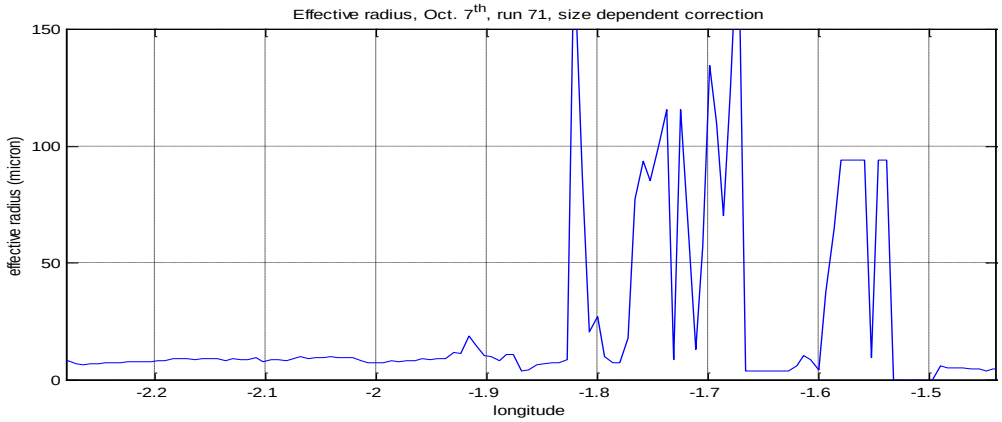

Figure E.6c: The effective radius using the size dependent correction for run 71, Oct. 7th.

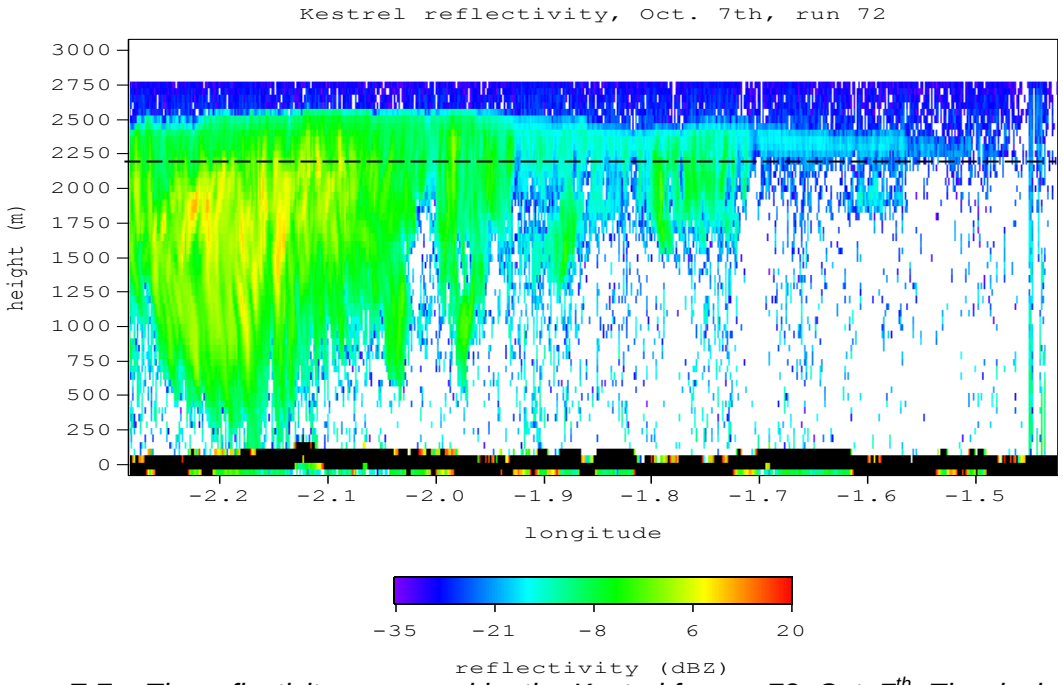

Figure E.7a: The reflectivity measured by the Kestrel for run 72, Oct. 7th. The dashed line shows the track of the Hercules.

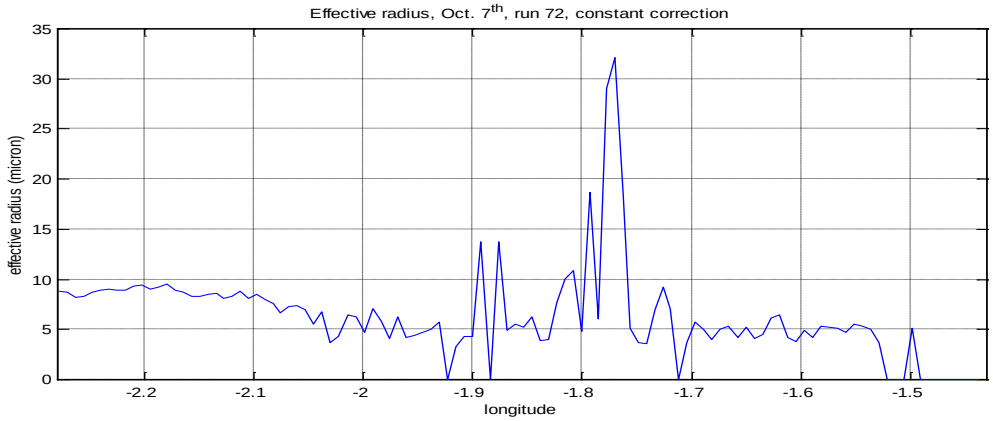

Figure E.7b: The effective radius using the constant correction for run 72, Oct. 7th.

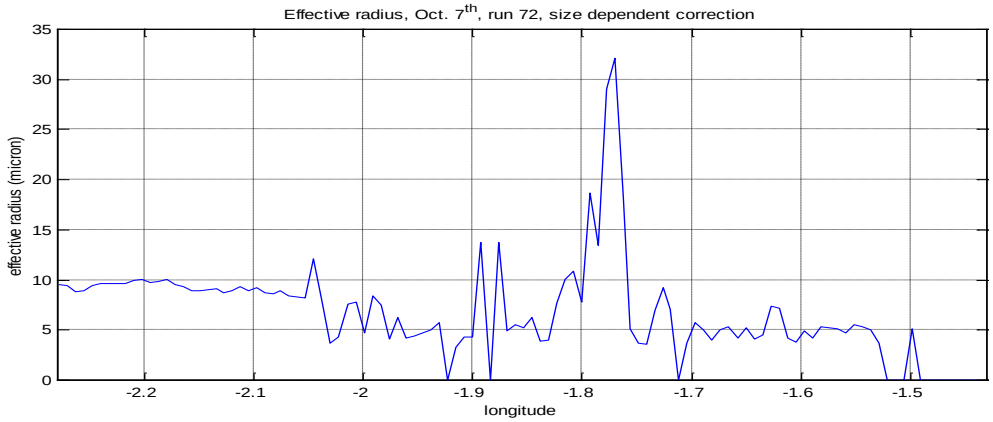

Figure E.7c: The effective radius using the size dependent correction for run 72, Oct. 7th.

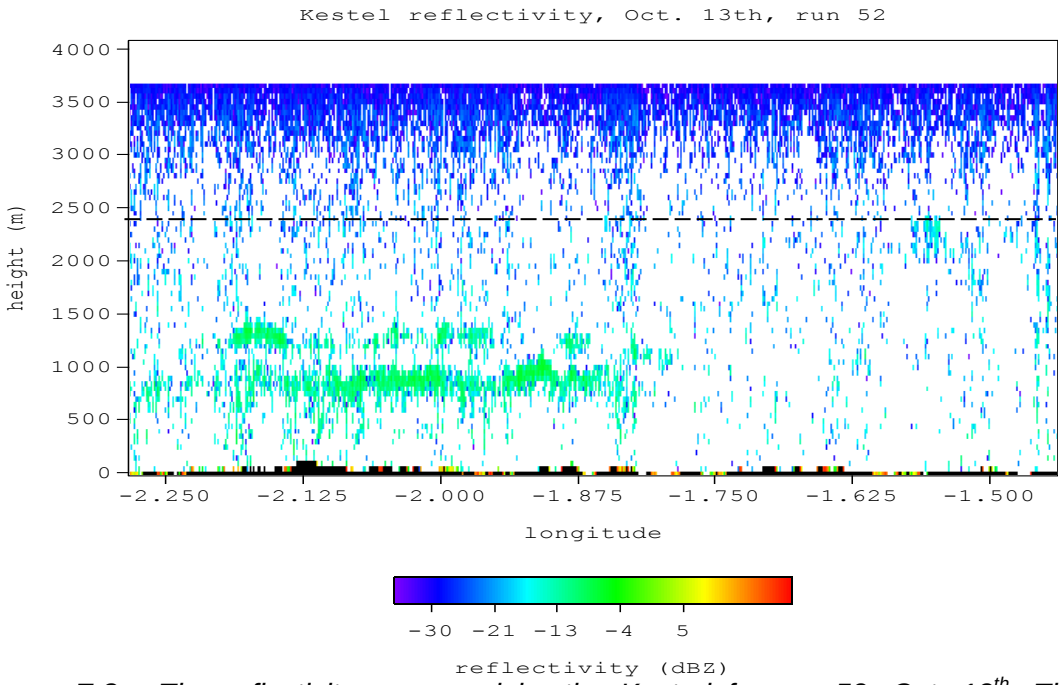

Figure E.8a: The reflectivity measured by the Kestrel for run 52, Oct. 13th. The dashed line shows the track of the Hercules.

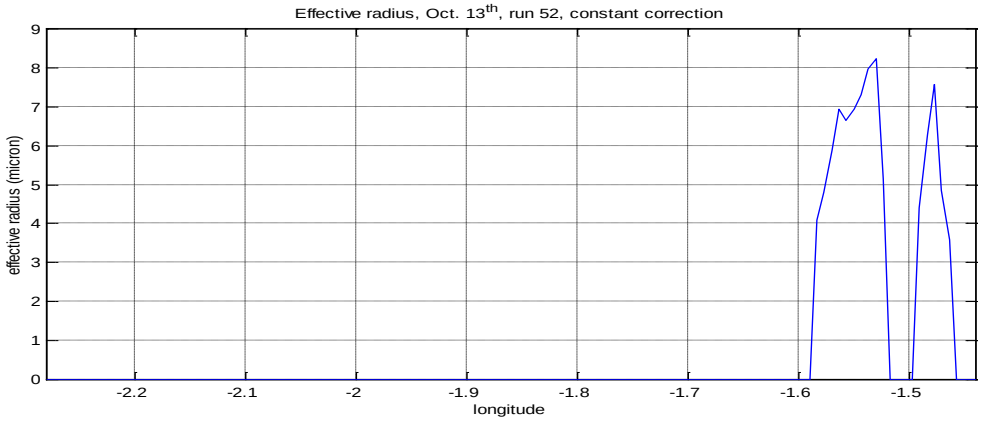

Figure E.8b: The effective radius using the constant correction for run 52, Oct. 13th.

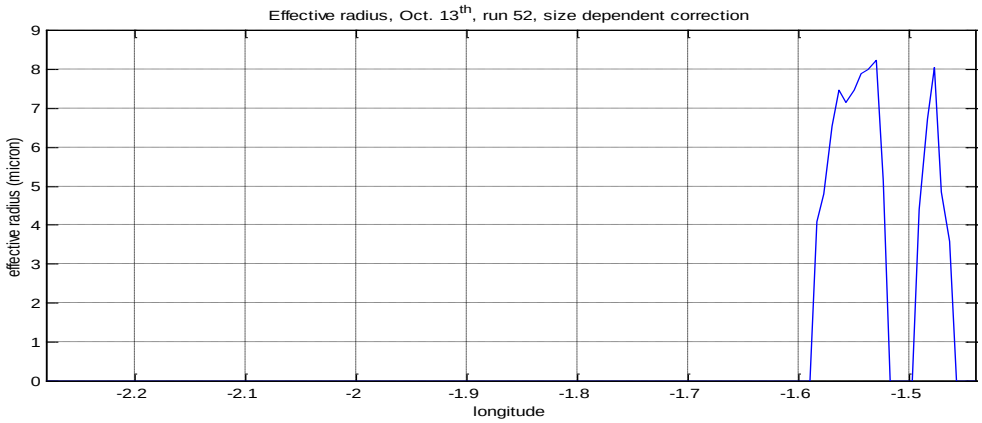

Figure E.8c: The effective radius using the size dependent correction for run 52, Oct. 13th.

Appendix F. Namibian data; Z-LWC relations constant correction

In this appendix the Z-LWC relationships computed from data measured in Namibia are presented. In each figure the least-squares fit is plotted, using this fit the Z-LWC relationship can be written as: $z = a*LWC^b$. The constants *a* and *b* and the root-mean-square (rms) value are given in the title of each plot.
First the $Z_{FSSP+2DC}$ versus $LWC_{FSSP+2DC}$ scatter plots are presented. In this case data with Z < -35 dBZ or LWC < 0.01 g/m^3 are not taken into account.
Then the Z_{FSSP} versus LWC_{FSSP} scatter plots are shown. These data are fitted discarding data with Z < -45 dBZ or LWC < 0.01 g/m^3.

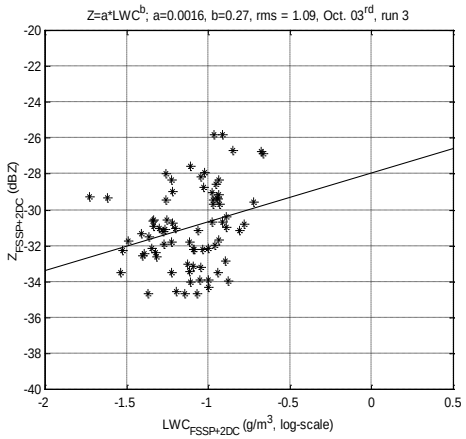

Fig F.1: Run 3, Oct. 3rd, rms- error is 1.09.

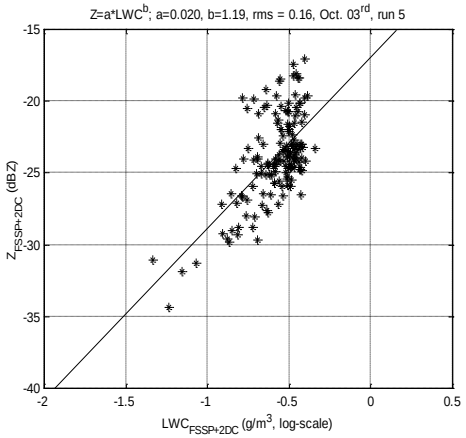

Fig F.2: Run 5, Oct. 3rd, rms- error is 0.16.

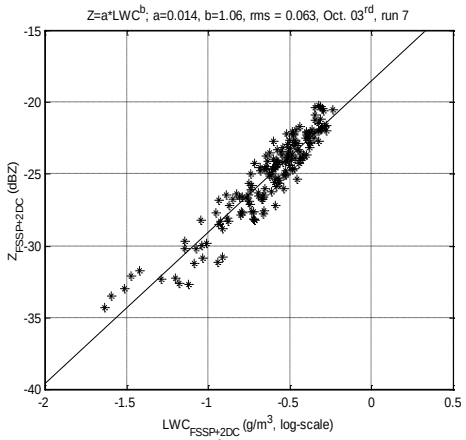

Fig F.3: Run 7, Oct. 3rd, rms- error is 0.063.

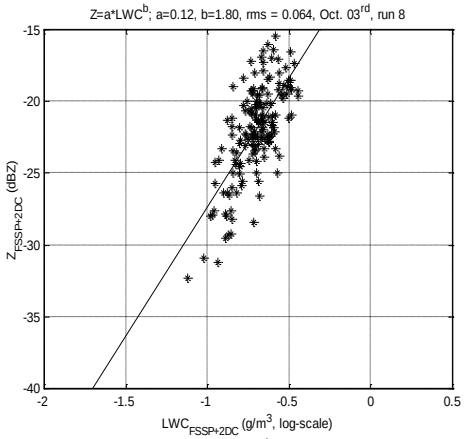

Fig F.4: Run 8, Oct. 3rd, rms- error is 0.064.

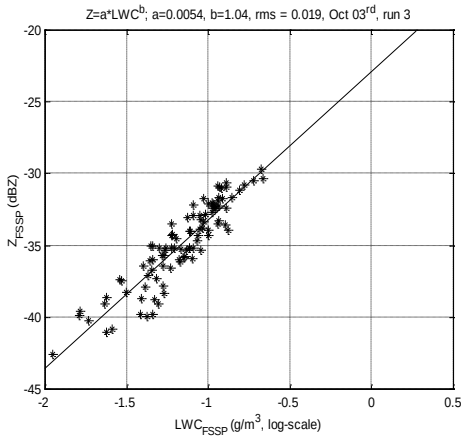

Fig F.5: Run 3, Oct. 3rd, rms- error is 0.019.

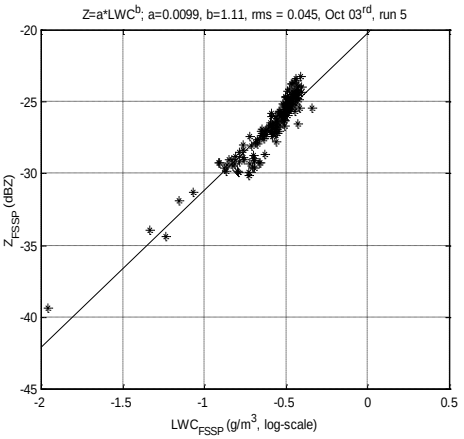

Fig F.6: Run 5, Oct. 3rd, rms- error is 0.045.

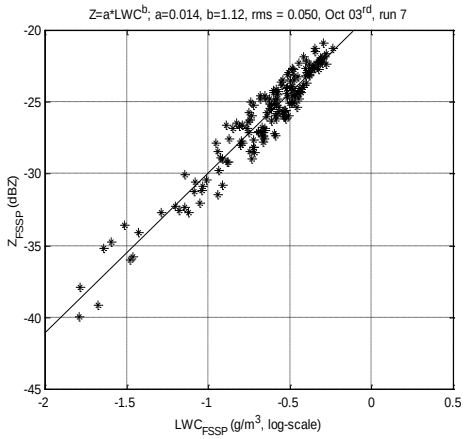

Fig F.7: Run 7, Oct. 3rd, rms- error is 0.050.

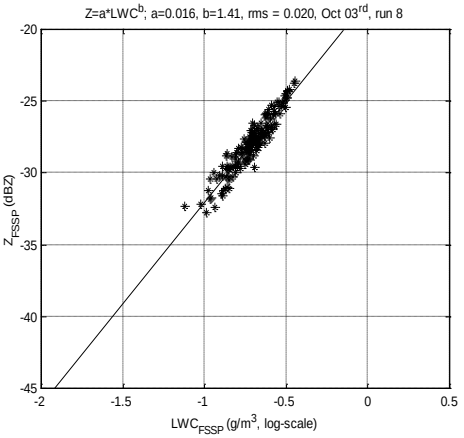

Fig F.8: Run 8, Oct. 3rd, rms- error is 0.020.

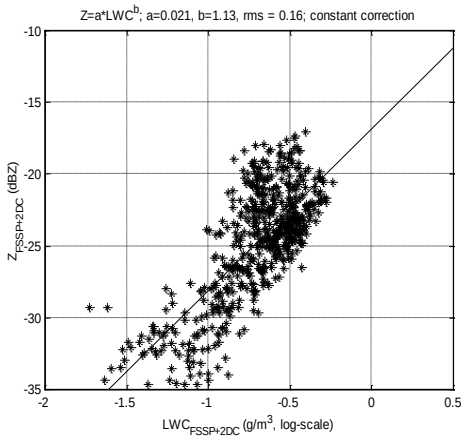

Fig F.9: Fit on all Namibian data taking the 2DC data into account, rms-error is 0.16.

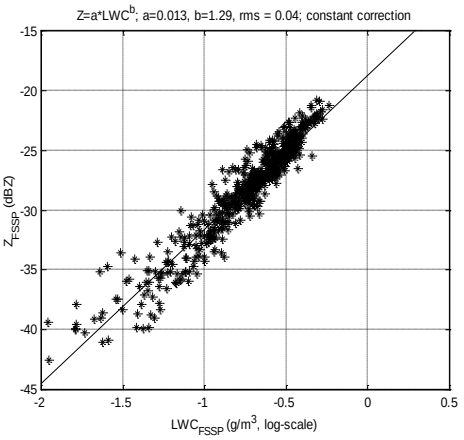

Fig F.10: Fit on all Namibian data taking only the FSSP data into account, rms-error is 0.04.

Appendix G. Namibian data; Z-LWC relations size dependent correction

In this appendix the Z-LWC relationships from the data measured in Namibia are included. In each figure the least-squares fit is plotted, using this fit the Z-LWC relationship can be written as: $z = a*LWC^b$. The constants *a* and *b* and the root-mean-square (rms) value are given in the title of each plot.
First the $Z_{FSSP+2DC}$ versus $LWC_{FSSP+2DC}$ scatter plots are presented. In this case data with Z < -35 dBZ or LWC < 0.01 g/m^3 are not taken into account.
Then the Z_{FSSP} versus LWC_{FSSP} scatter plots are shown. These data are fitted discarding data with Z < -45 dBZ or LWC < 0.01 g/m^3.

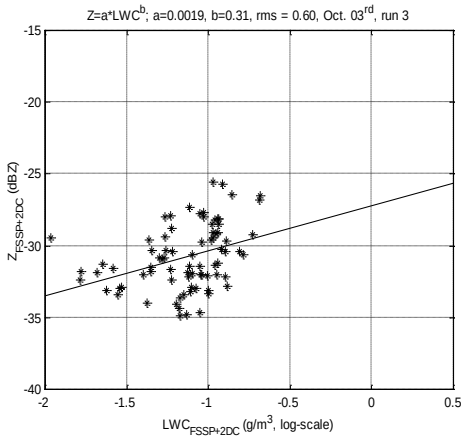

Fig G.1: Run 3, Oct. 3rd, rms- error is 0.60.

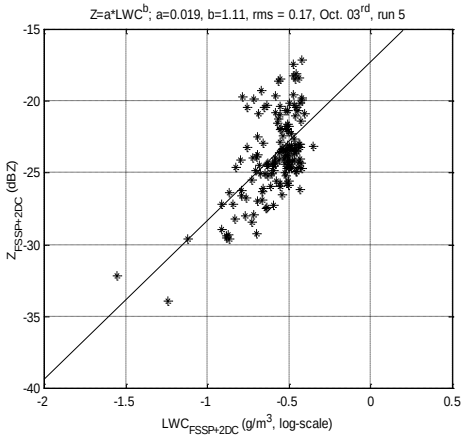

Fig G.2: Run 5, Oct. 3rd, rms- error is 0.17.

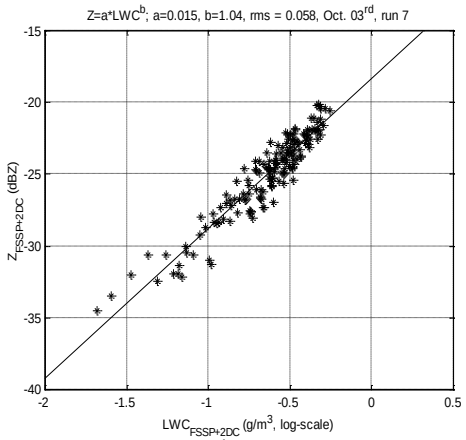

Fig G.3: Run 7, Oct. 3rd, rms- error is 0.058.

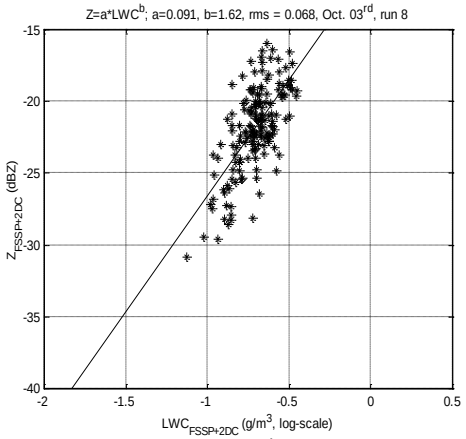

Fig G.4: Run 8, Oct. 3rd, rms- error is 0.068.

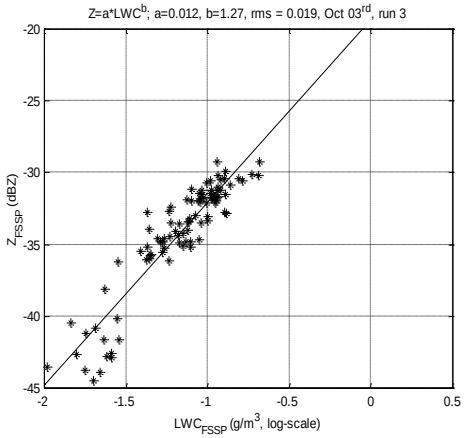

Fig G.5: Run 3, Oct. 3rd, rms- error is 0.019.

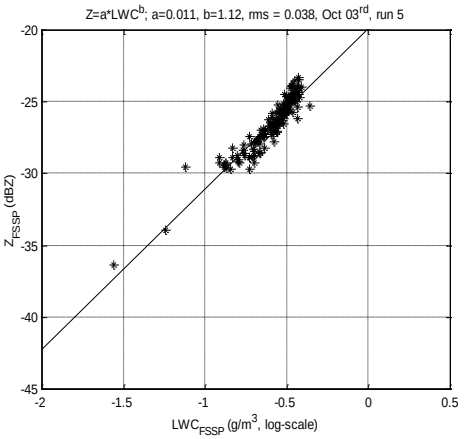

Fig G.6: Run 5, Oct. 3rd, rms- error is 0.038.

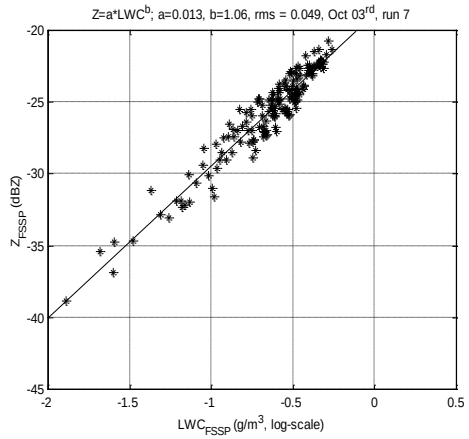

Fig G.7: Run 7, Oct. 3rd, rms- error is 0.049.

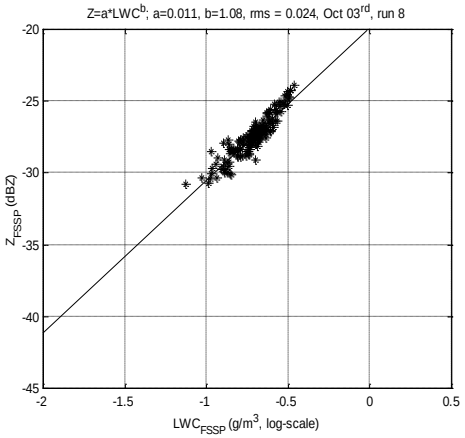

Fig G.8: Run 8, Oct. 3rd, rms- error is 0.024.

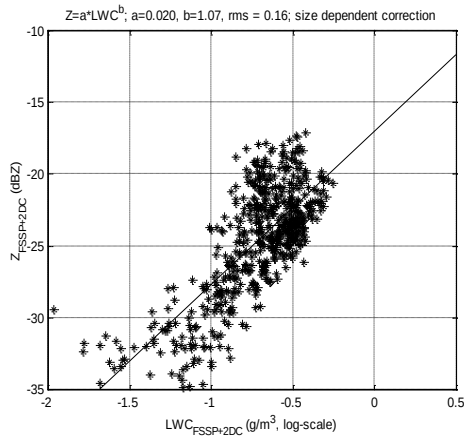

Fig G.9: Fit on all Namibian data taking the 2DC data into account, rms-error is 0.16.

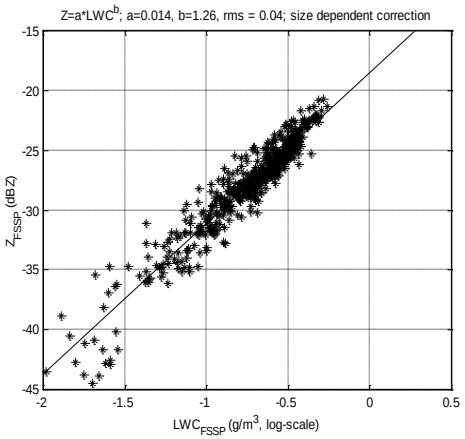

Fig G.10: Fit on all Namibian data taking only the FSSP data into account, rms-error is 0.04.

Appendix H. Namibian data; reflectivity, LWC and effective radius constant correction

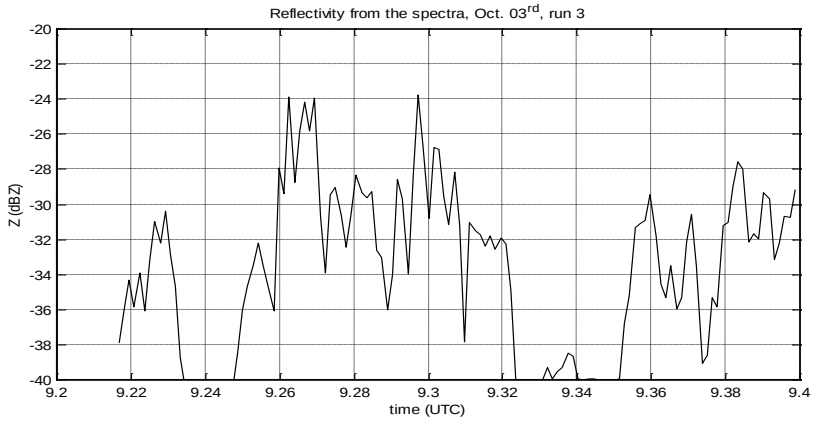

Figure H.1a: The reflectivity versus longitude for run 3, Oct. 3rd.

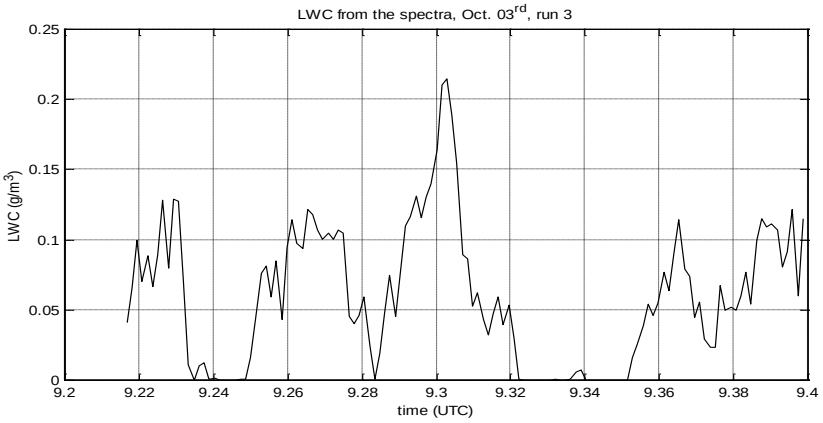

Figure H.1b: The LWC versus longitude for run 3, Oct. 3rd.

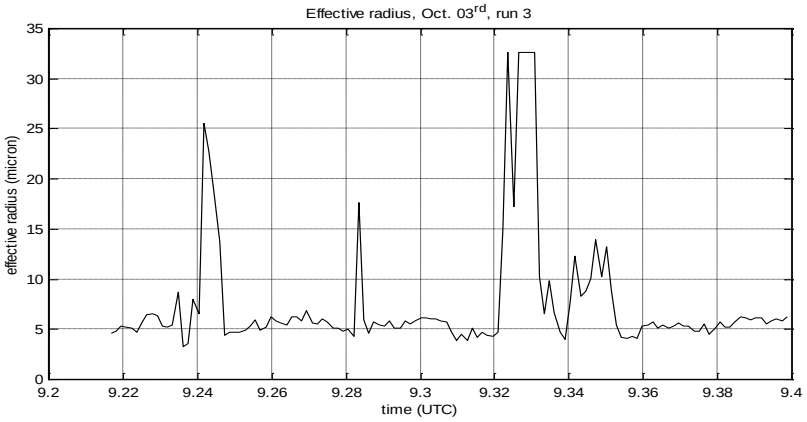

Figure H.1c: The effective radius versus longitude for run 3, Oct. 3rd.

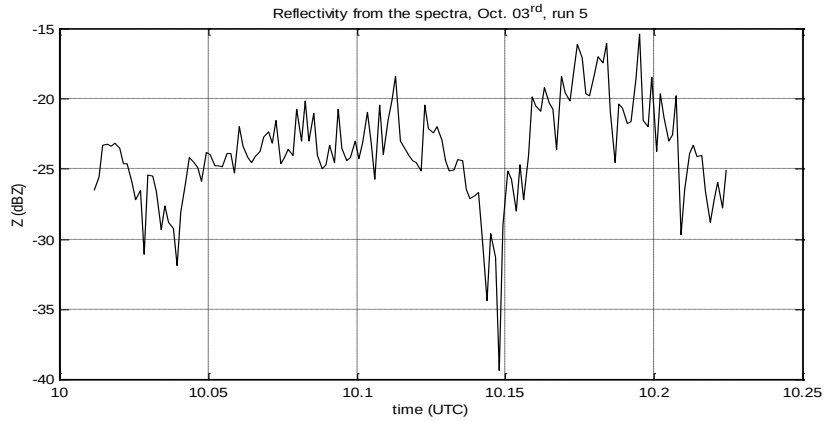

Figure H.2a: The reflectivity versus longitude for run 5, Oct. 3rd.

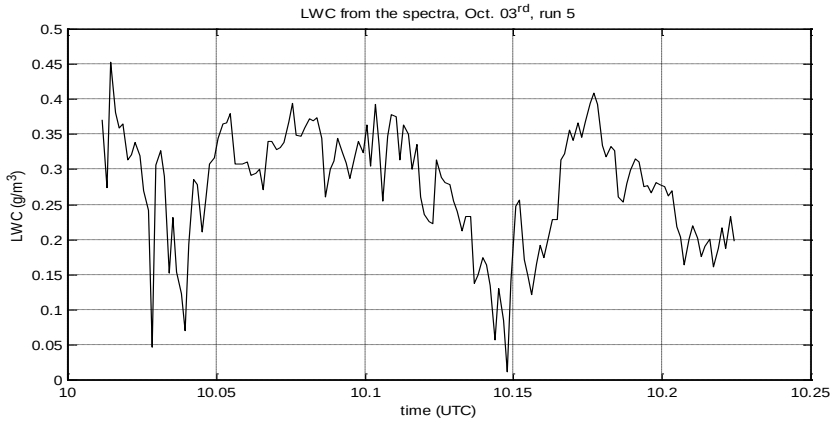

Figure H.2b: The LWC versus longitude for run 5, Oct. 3rd.

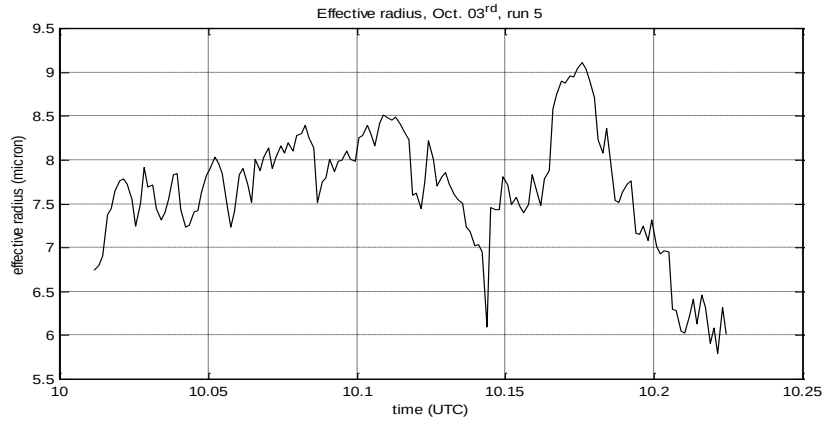

Figure H.2c: The effective radius versus longitude for run 5, Oct. 3rd.

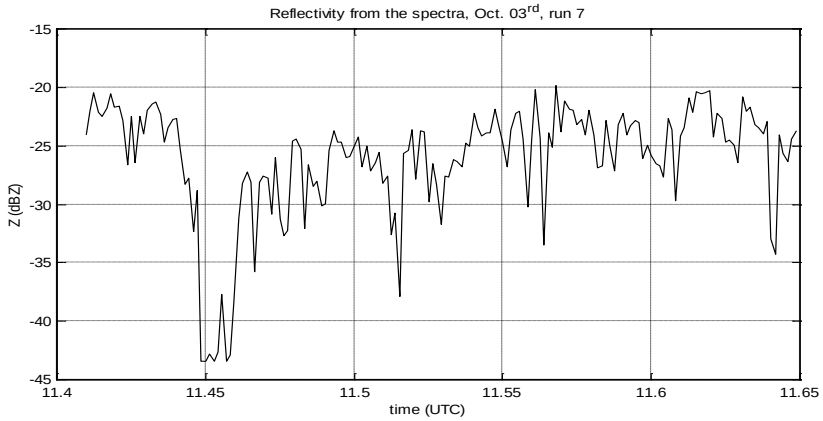

Figure H.3a: The reflectivity versus longitude for run 7, Oct. 3rd.

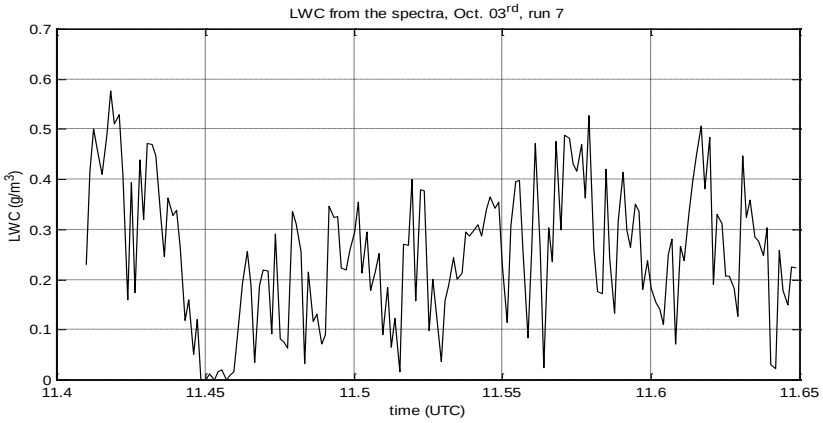

Figure H.3b: The LWC versus longitude for run 7, Oct. 3rd.

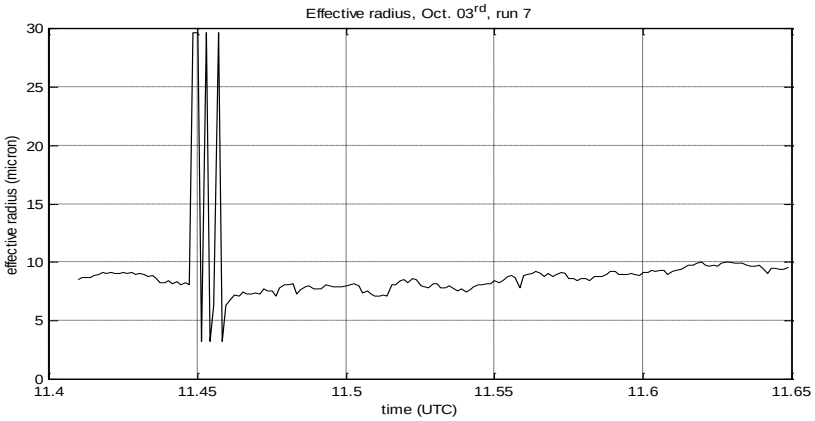

Figure H.3c: The effective radius versus longitude for run 7, Oct. 3rd.

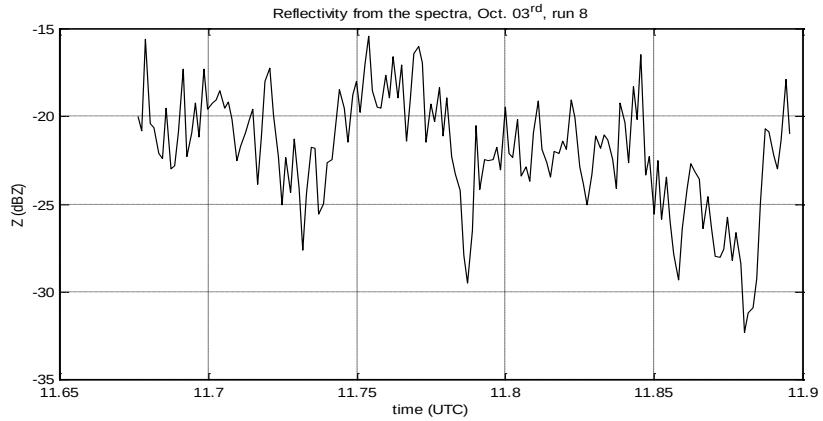

Figure H.4a: The reflectivity versus longitude for run 8, Oct. 3rd.

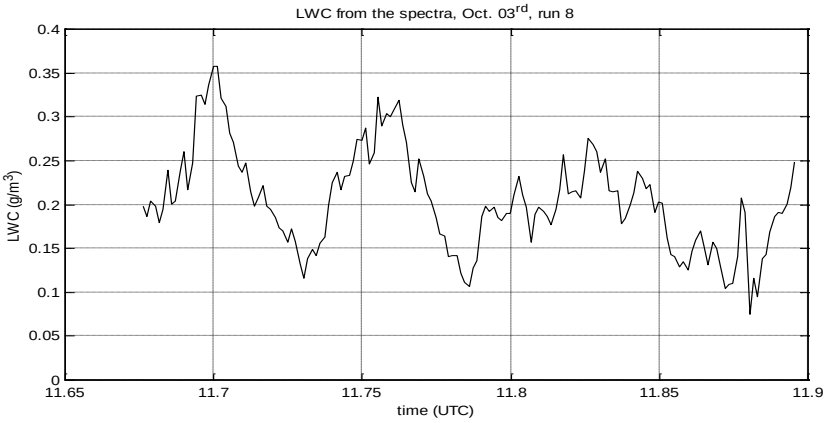

Figure H.4b: The LWC versus longitude for run 8, Oct. 3rd.

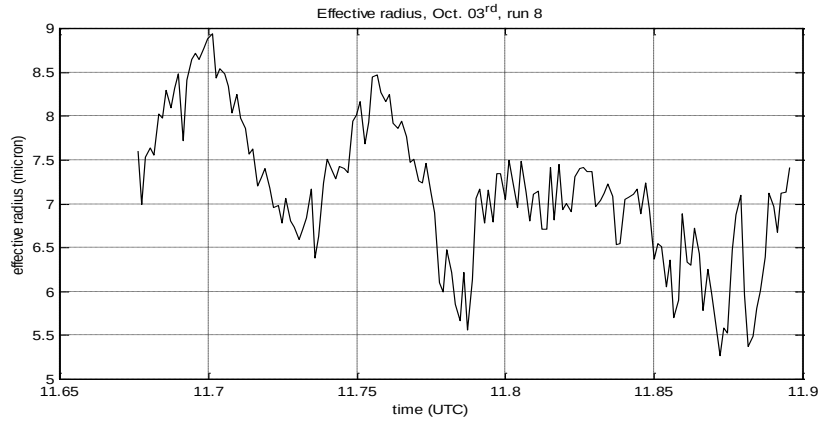

Figure H.4c: The effective radius versus longitude for run 8, Oct. 3rd.

Appendix I. Namibian data; reflectivity, LWC and effective radius size dependent correction

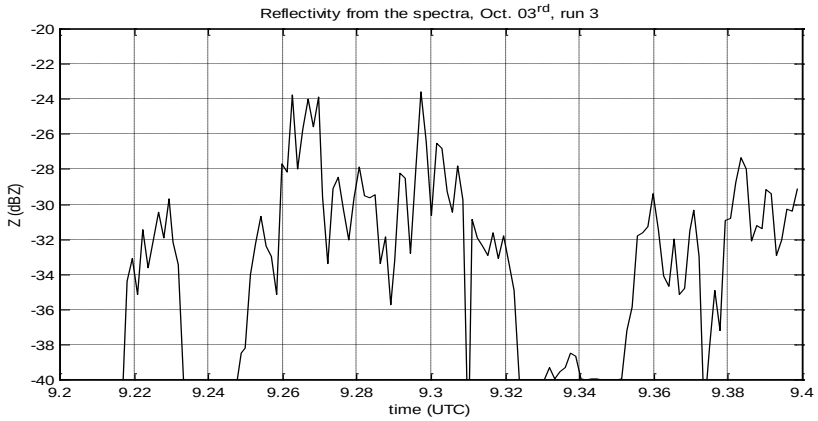

Figure I.1a: The reflectivity versus longitude for run 3, Oct. 3rd.

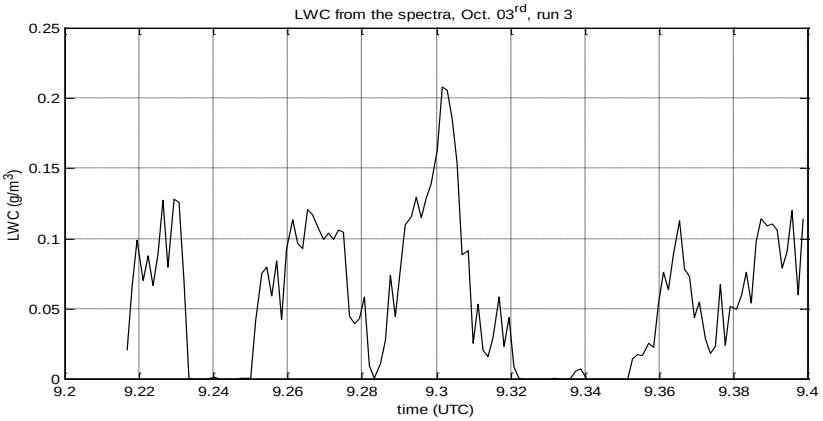

Figure I.1b: The LWC versus longitude for run 3, Oct. 3rd.

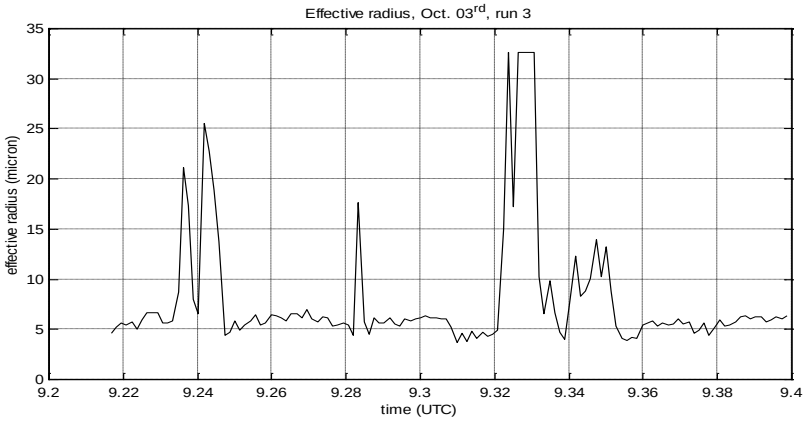

Figure I.1c: The effective radius versus longitude for run 3, Oct. 3rd.

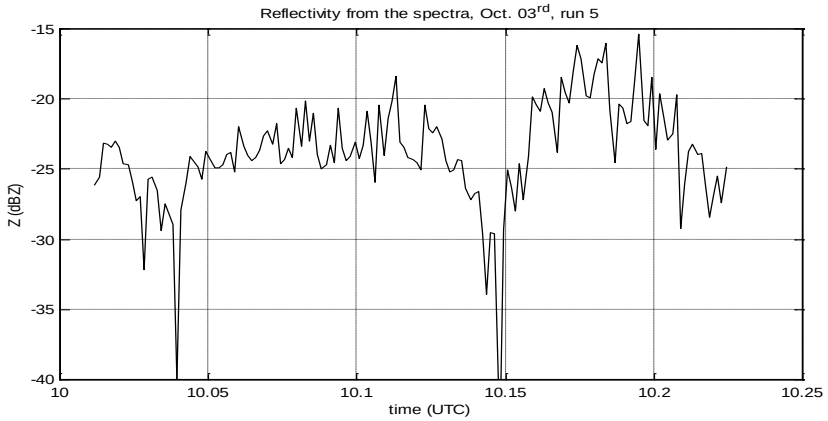

Figure I.2a: The reflectivity versus longitude for run 5, Oct. 3rd.

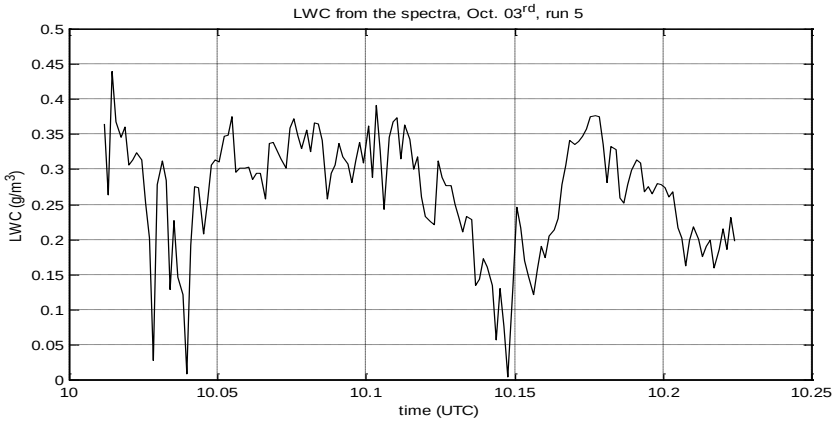

Figure I.2b: The LWC versus longitude for run 5, Oct. 3rd.

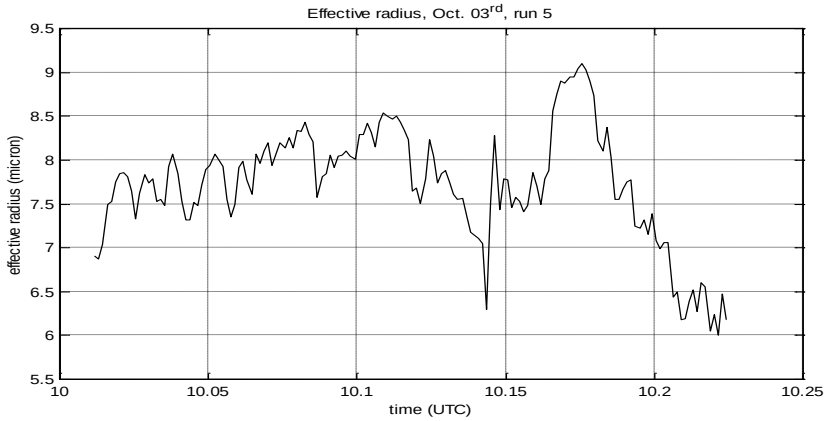

Figure I.2c: The effective radius versus longitude for run 5, Oct. 3rd.

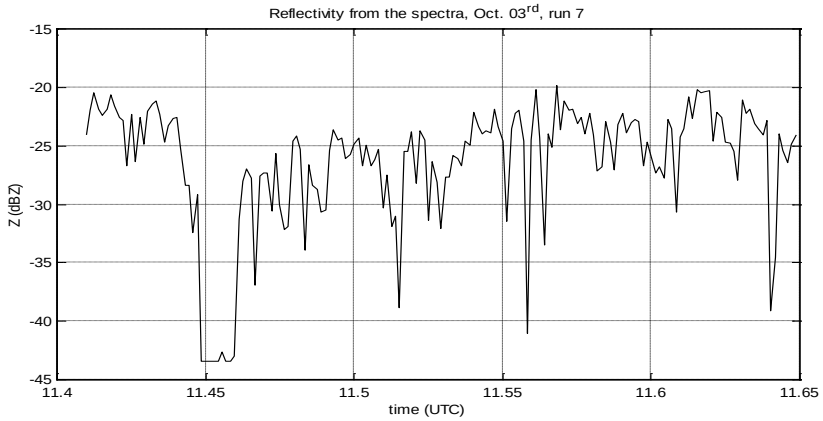

Figure I.3a: The reflectivity versus longitude for run 7, Oct. 3rd.

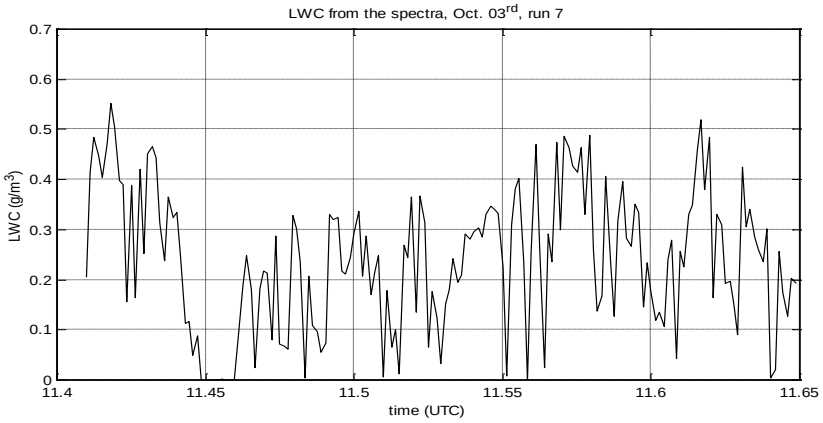

Figure I.3b: The LWC versus longitude for run 7, Oct. 3rd.

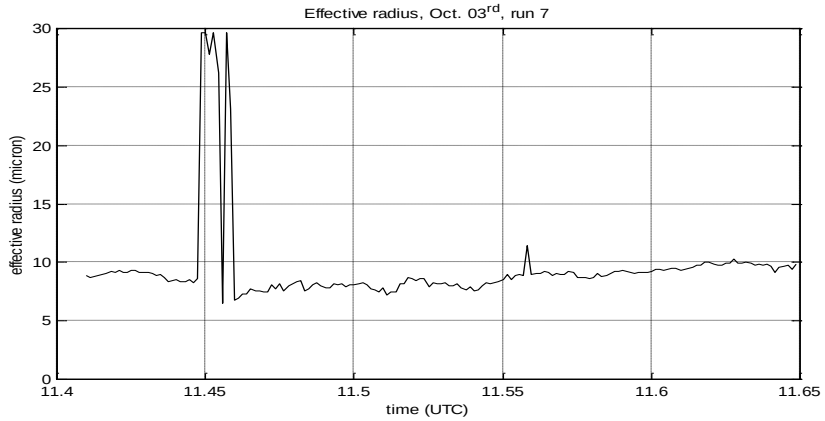

Figure I.3c: The effective radius versus longitude for run 7, Oct. 3rd.

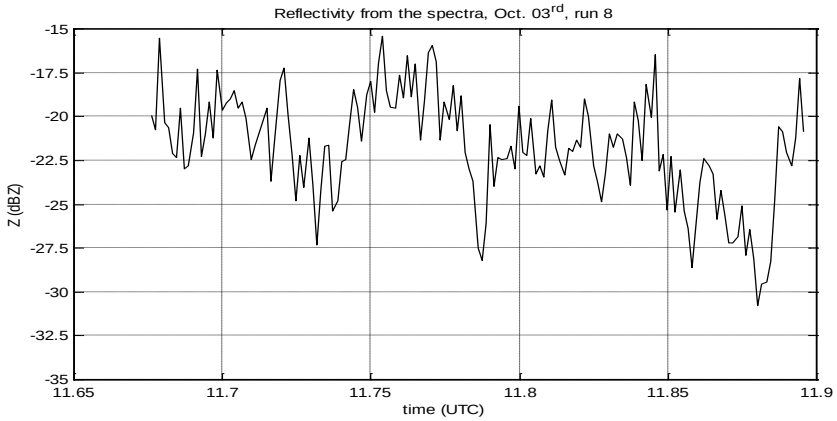

Figure I.4a: The reflectivity versus longitude for run 8, Oct. 3rd.

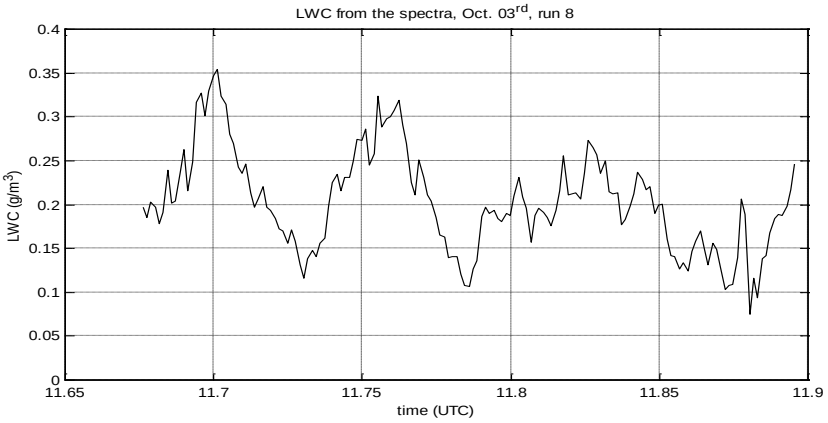

Figure I.4b: The LWC versus longitude for run 8, Oct. 3rd.

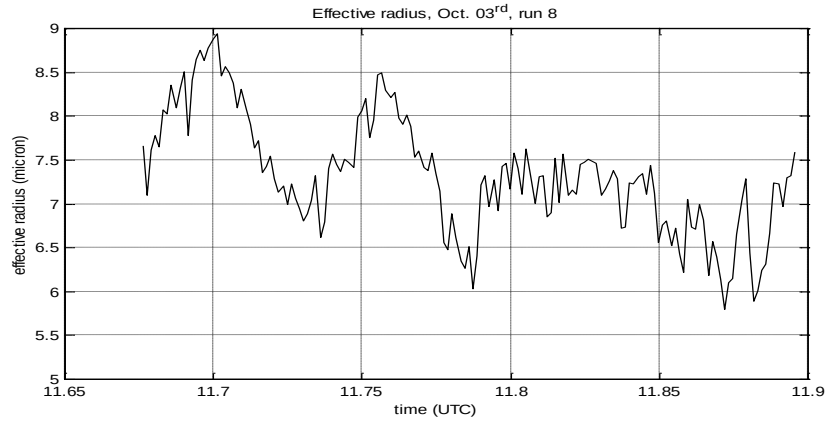

Figure I.4c: The effective radius versus longitude for run 8, Oct. 3rd.

Appendix J. The results obtained with the Kestrel data

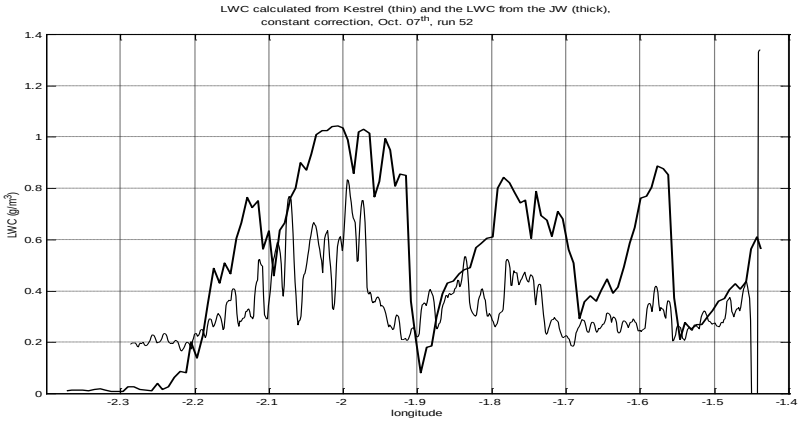

Figure J.1a: The computed and measured LWC for run 52, Oct. 7th.

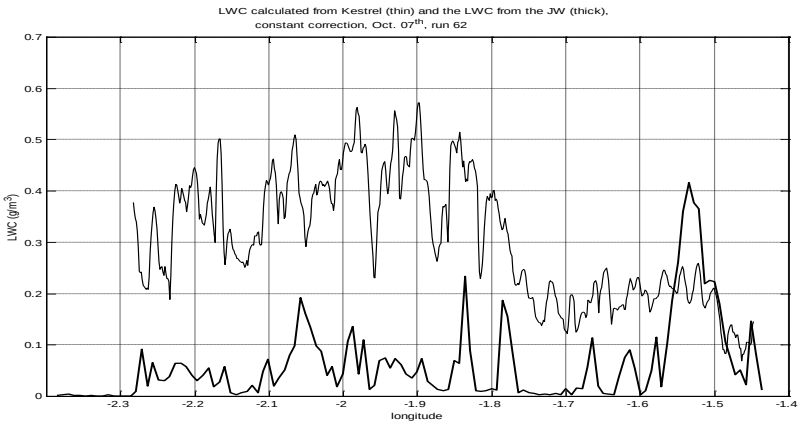

Figure J.1b: The computed and measured LWC for run 62, Oct. 7th.

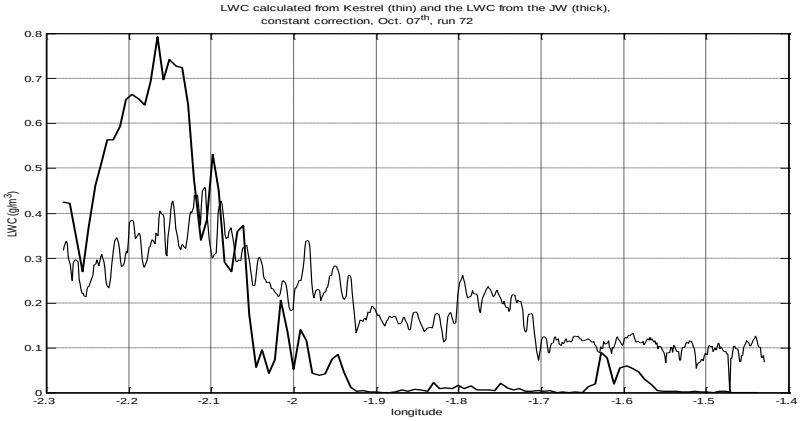

Figure J.1c: The computed and measured LWC for run 72, Oct. 7th.

Figure J.1: The LWC measured by the Johnson-Williams (thick) and the LWC estimated from the 94 GHz Kestrel data (thin). The LWC is computed using relation (4.2) (constant correction).

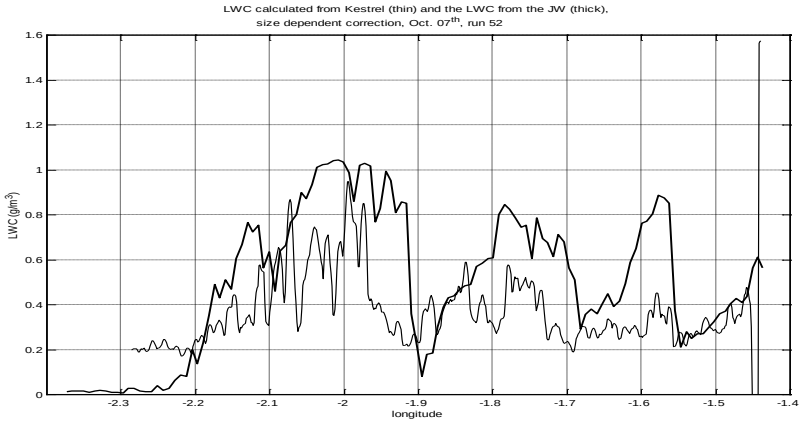

Figure J.2a: The computed and measured LWC for run 52, Oct. 7th.

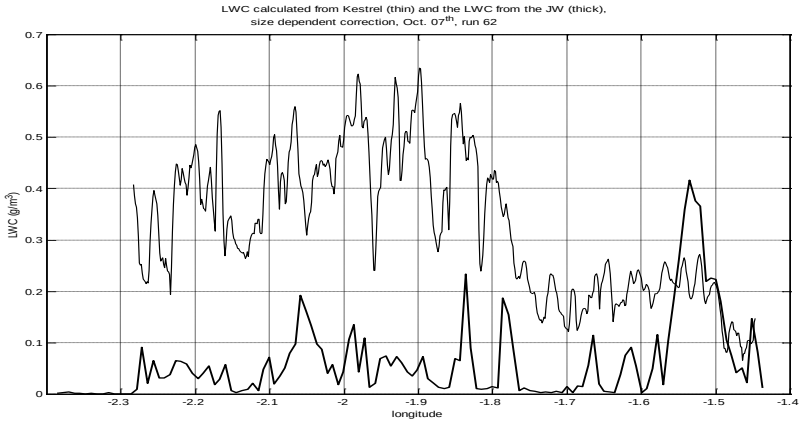

Figure J.2b: The computed and measured LWC for run 62, Oct. 7th.

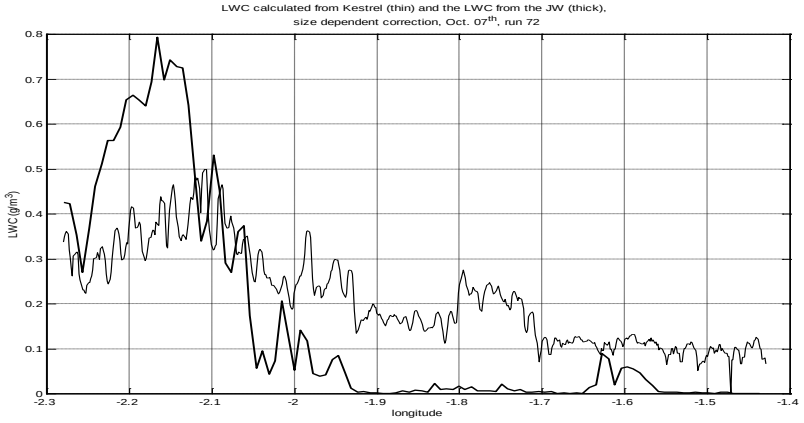

Figure J.2c: The computed and measured LWC for run 72, Oct. 7th.

Figure J.2: The LWC measured by the Johnson-Williams (thick) and the LWC estimated from the 94 GHz Kestrel data (thin). The LWC is computed using relation (4.3) (size dependent correction).

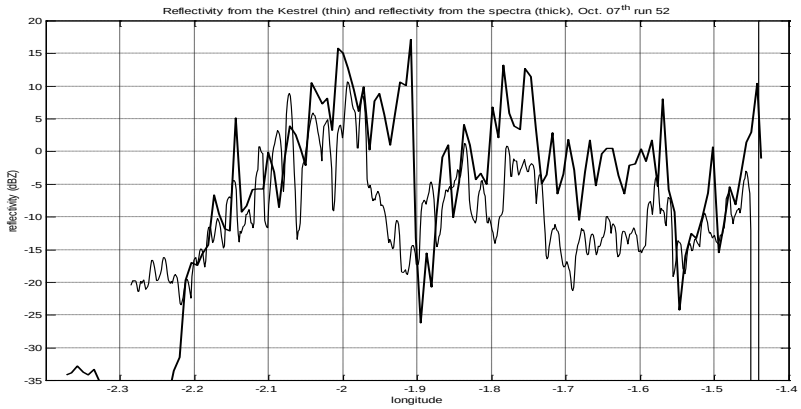

Figure J.3a: The computed and measured reflectivity for run 52, Oct. 7th.

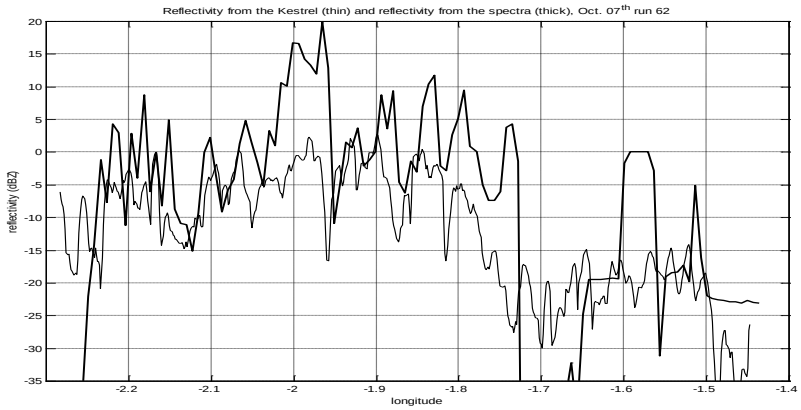

Figure J.3b: The computed and measured reflectivity for run 62, Oct. 7th.

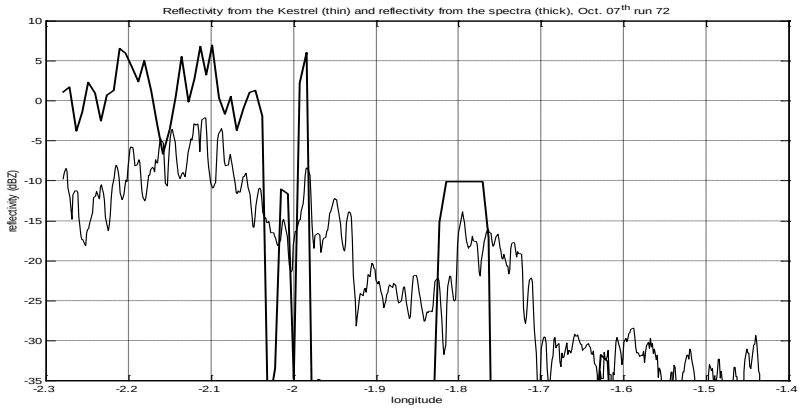

Figure J.3c: The computed and measured reflectivity for run 72, Oct. 7th.

Figure J.3: The reflectivity measured by the 94 GHz Kestrel radar (thin) and the reflectivity calculated from the particle size spectra (thick).

Appendix K. Images of the ground based Miracle radar

In this appendix the images from the ground based 94 GHz Miracle radar are included. The Miracle radar was situated at Chilbolton. Note that the Miracle has a 'blind range' of approximately 900 m; the measurements start at 984 m. The time is in decimals.

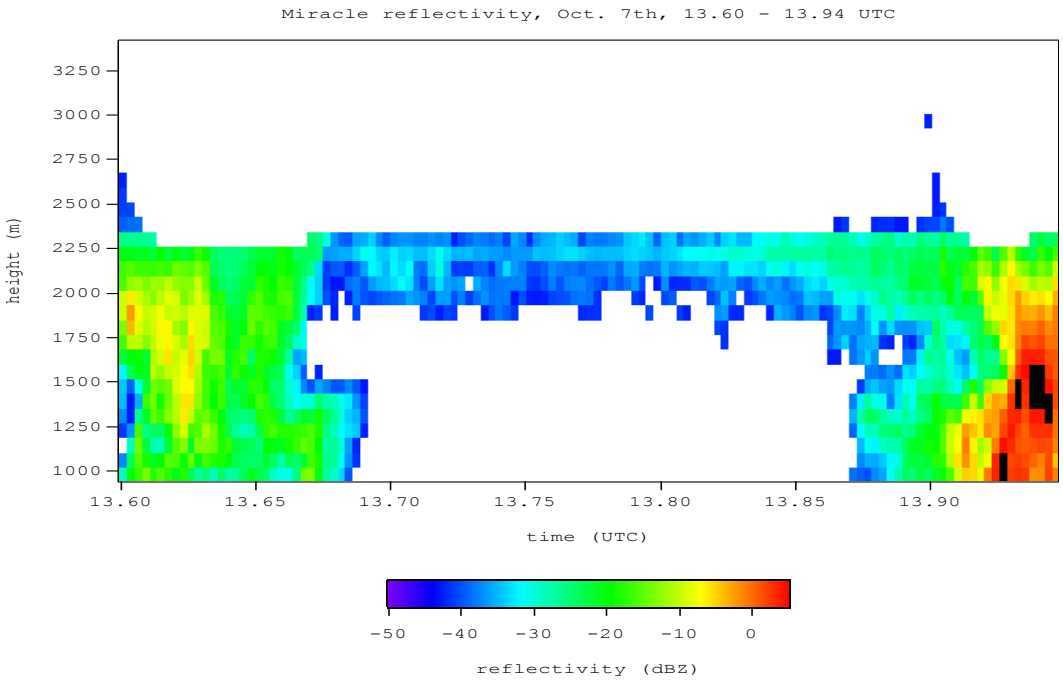

Figure K.1: The reflectivity measured by the Miracle between 13.60 and 13.94 UTC. During this time run 51 was flown.

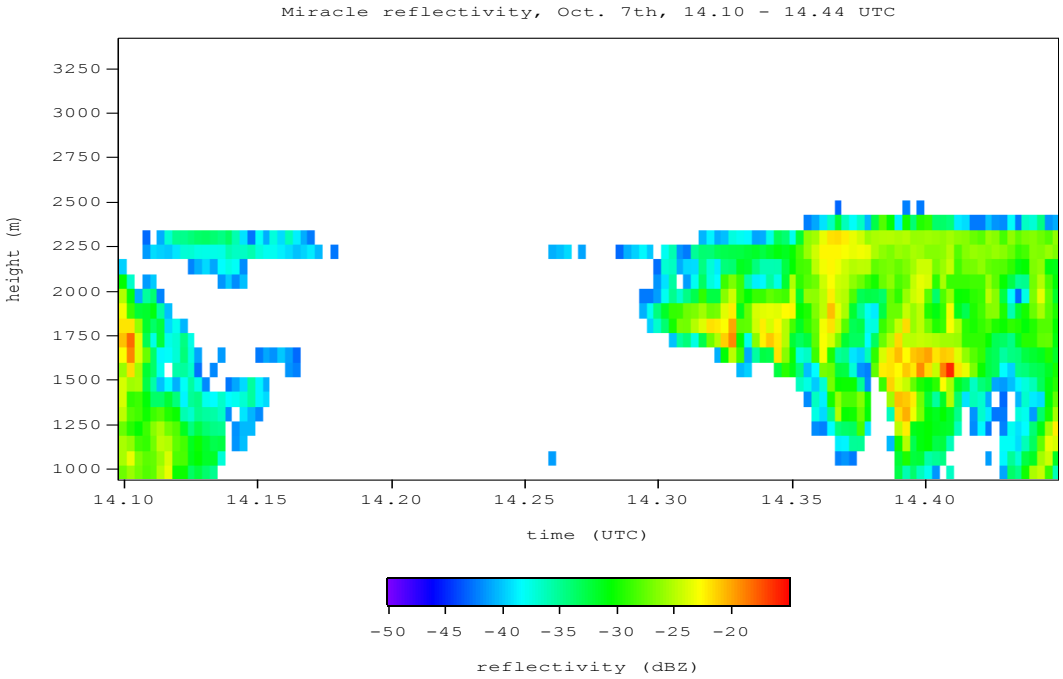

Figure K.2: The reflectivity measured by the Miracle between 14.10 and 14.44 UTC. During this time the last part of run 52 and run 61 were flown.

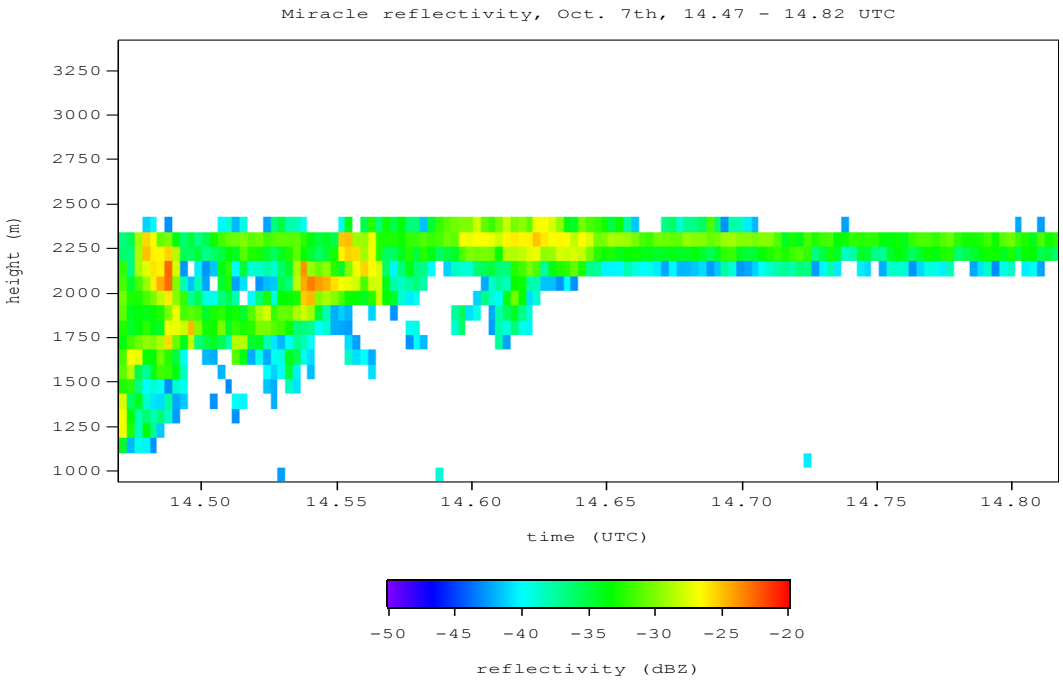

Figure K.3: The reflectivity measured by the Miracle between 14.47 and 14.82 UTC. During this run 62 and the first part of run 71 were flown.

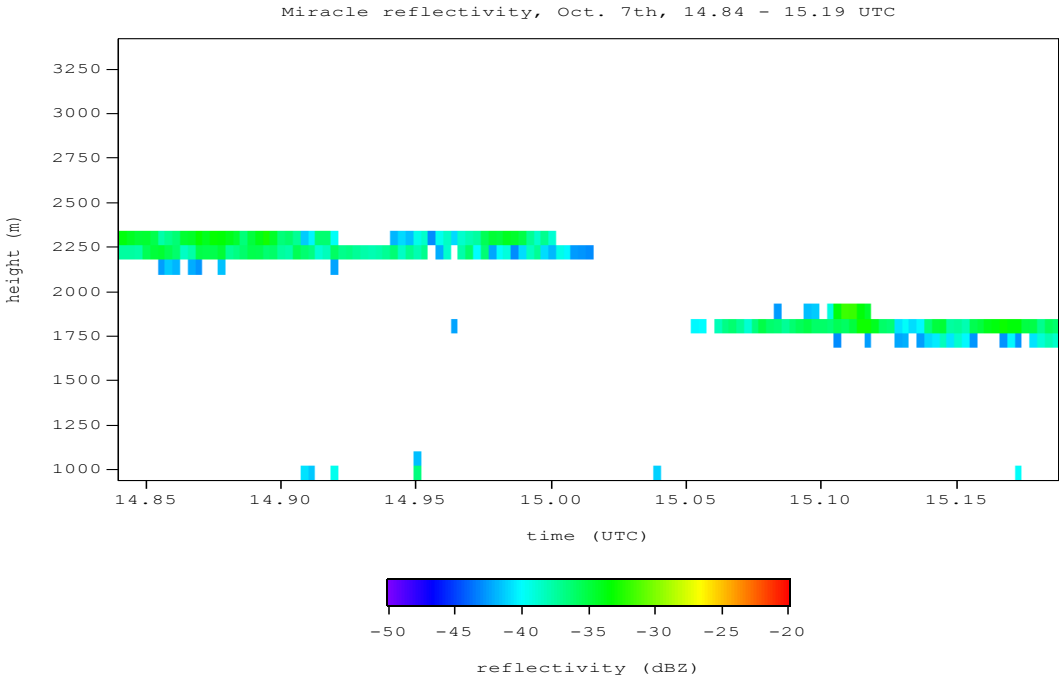

Figure K.4: The reflectivity measured by the Miracle between 14.84 and 15.19 UTC. During this time the last part of run 71 and the first part of run 72 were flown.